9-4-2019

Microfluidic Systems for Cancer Diagnostics

Mohamed Sharafeldin
University of Connecticut - Storrs, mohamed.sharafeldin@uconn.edu

9-4-2019

Microfluidic Systems for Cancer Diagnostics

Mohamed Sharafeldin

Microfluidic Systems for Cancer Diagnostics

Mohamed Sharafeldin, PhD

University of Connecticut, 2019

Cancer is the second leading cause of death among noncommunicable diseases coming right after cardiovascular diseases. Early diagnosis is a key for improving survival expectancy and treatment outcomes as cancer in early stage is more responsive to treatment. Currently, center of diseases control and prevention (CDC) recommend regular screening for cervical, breast and colorectal cancers. Although other screening procedures are available for prostate, pancreatic, thyroid and ovarian cancer, they did not prove to be effective in reducing mortality rates of these cancers. Adaption of prostate specific antigen (PSA) screening test for prostate cancer has not been related to improved survival rates instead it resulted in what has been known as “prostate cancer epidemic” due to overdiagnosis and overtreatment of prostate cancer.

The dilemma of current cancer diagnostic techniques results from the tradeoff between specificity and sensitivity of the cancer screening. Specific cancer screening strategies that depend on either imaging or histopathological examination are not sensitive enough and miss latent or asymptomatic cancers. While sensitive techniques that depend on biomarker screening in biofluids like PSA test are not specific enough for accurate decision. In addition, most of these techniques are time consuming, expensive and require centralized laboratories with highly trained technicians. These criteria limit the availability of cancer screening technique to developed countries with well-established healthcare systems and limit their application in areas with limited resources.

Mohamed Sharafeldin, University of Connecticut, 2019

The goal of this thesis is to develop and test techniques with promising specificity and sensitivity for screening and staging of different types of cancers. Several approaches have been studied to develop point-of-care (POC) sensors for prostate, head and neck cancers that are of low cost, utilizes low sample volumes, automated or semiautomated, and can be utilized in remote areas with limited resources. 3D printing was used to prototype and mass produce microfluidic chips and adaptors with better fluid handling characteristics and much lower cost than traditional microfluidic systems. Panels of selected biomarker proteins were multiplexed on the same microfluidic chip to improve assay specificity while maintaining ultralow sensitivities.

Microfluidic Systems for Cancer Diagnostics

Mohamed Sharafeldin

BS, Zagazig University, 2006

MS, Zagazig University, 2011

A Dissertation Submitted in Partial

Fulfilment of the Requirements for the

Degree of Doctoral of Philosophy at the

University of Connecticut

2019

Copyrights

Mohamed Sharafeldin

2019

Approval Page

Doctor of Philosophy Dissertation

Microfluidic Systems for Cancer Diagnostics

Presented by

Mohamed Sharafeldin, BS, MS

Major Advisor ----------

James F. Rusling

Associate Advisor ----------

Alfredo Angeles-Boza

Associate Advisor ----------

Douglas H. Adamson

University of Connecticut

2019

Dedication

Dedicated to

My Parents

Sanaa and Nabil Sharafeldin

&

My wife

Safaa Soliman

&

My kids

Moaz and Rovan

2019

Acknowledgments

In spite of being international researcher, experiencing for the first time the broad and immense culture of united states and having to deal with all language, cultural and social barriers, I still managed to reach this point and have this dissertation completed without feeling any hurdle. This could not have been achieved without the help, support and encouragement of many people working relentlessly behind the scene.

I would like to express my gratitude and appreciation to Prof. James Rusling, my major advisor, for making this journey possible. With his encouragement, guidance and support throughout different phases of PhD, I did not only learn solid science but also evolved to be more self-confident and had the courage to argue and defend my position. Dr Rusling provided a safe zone for trial and error while working with multidisciplinary research teams across the globe, a privilege that shaped a successful learning experience for me and many others. With the help of my associate advisors, Dr Alfredo Angeles-Boza, Dr Jing Zhao, and Dr Douglas Adamson, I felt that the road was always lighted up with their advises and suggestions. They were always there whenever I needed help or sought advice on future research plans or career. I also would like to thank Dr Dharamainder Choudhary for being such a great teacher and collaborator and accepting to be part of my examination committee. Dr Choudhary's experience in cell culture was of great help to me working on cell cultures for the first time. I would like also to thank my first teaching advisor Dr Fatma Selampinar for the guidance and support she provided that helped me promote my teaching skills and also for accepting to participate in my examination committee.

I appreciate the help and support provided by the all the faculty and staff of chemistry department at University of Connecticut. Faculty were always approachable and available for discussion and

staff always helped with administrative issues and helped place orders for chemicals and materials. I would like to specially thank Dr Steven Suib, Dr Joseph Depasquale, Dr Clyde Cady for their valuable cooperation and guidance. I also would like to thank Emilie Hogrebe, Charlene Fuller, Daniel Daleb, Tyler Cardinal and all undergraduate laboratory staff. I am also grateful to current Rusling group members and alumni, they helped me launch my research and provided a friendly collaborative research environment. I always appreciated the discussion, meeting and help from Dr Amit Joshi, Dr Chandra Dixit, Dr Islam Mosa, Dr Min She, Dr Karteek Kadimisetty, Dr Gregory Bishop, Dr Brunah Oteino, Dr Snehasis Bhakta, Di Jiang, Dr Gayatri Phadke, Dr Jennifer Satterwhite and Dr Collen Krause. I am also grateful to Abby Jones, Tianqi Chen (Kiki) and Kira McCaffrey for being such great lab partners. Dr Boya Song, Dr Abhisek, Nipuni, Israa, Ketki, Ben, Ahmed, Thilini, Randil, Keshani, Lasangi, Gulsum and Tom, you were outstanding lab mates and friends.

I would like to express my heartful gratitude to my family for the unlimited support and help they provided. My father and mother who were always there, although physically across the ocean, when I needed their prayers, emotional and psychological support. I also would like to thank the person who was there whenever I needed, my wife Safaa Soliman, who is an example of a caring mother, wife and close friend. I am also grateful to my kids Moaz and Rovan who had to suffer the manic PhD student father. I am grateful to my brothers Ayman and Sherif and my sister Omnia who always backed my adventures and were supportive and encouraging.

Table of Contents

List of Schemes

List of Figures

List of Tables

Chapter One

Introduction

1.1 Cancer Facts

Cancer is the second cause of death worldwide with approximately 10 million deaths expected in 2018. In US, approximately 1.7 million cases are diagnosed annually with more than 600,000 deaths.[1,2] Cancer screening helped improving survival rate and quality of life for many cancer survivors. Treatment options are more effective when cancerous lesions are small in size and did not metastasize to other parts of the body. FDA approved screening procedures for several types of cancers including colon, rectum, prostate, cervix and breast cancers which helped reduce mortality rate of these cancers.[3,4] Adoption of screening techniques in developed countries resulted in early diagnosis and more cancer incidences as compared to developing world (Fig. 1.1).

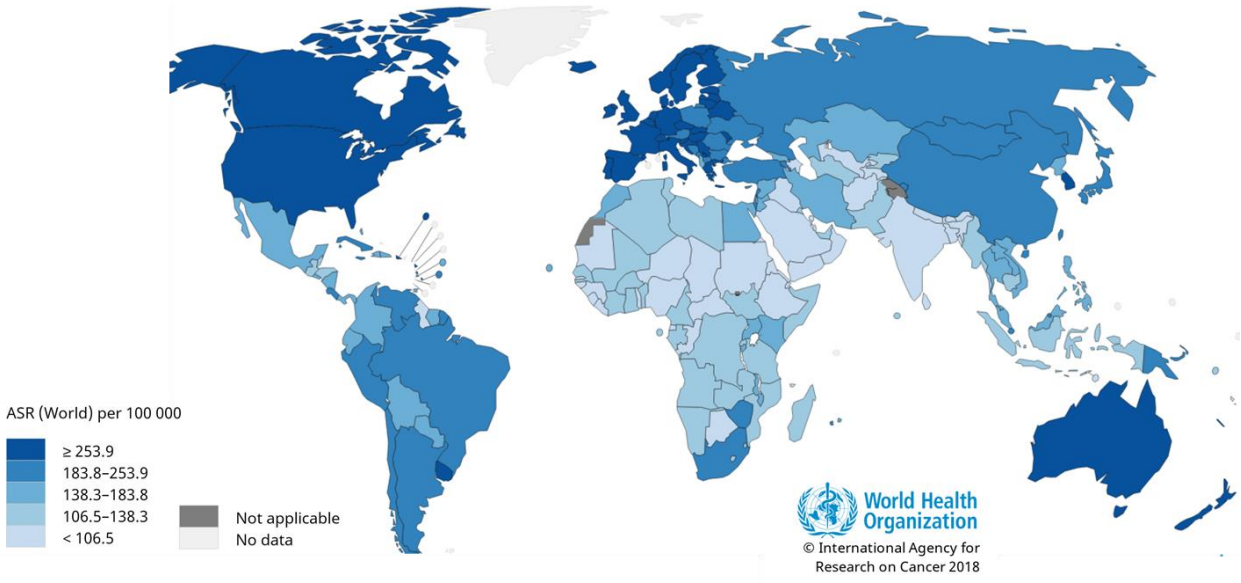

Fig. 1. 1 Estimated cancer Age-Standardized Rate (ASR) in 2018. Reproduced with permission from International Agency for Research on Cancer (IARC) GLOBOCAN 2018

Although proven to be helpful in reducing mortality rates, current diagnosis strategies results in overdiagnosis with patient receiving unnecessary treatment or undergoing life-threatening surgeries.[5] The alternate route for cancer diagnosis rely on physical exams with symptoms presented to healthcare providers or specialists. Specialist will always request further lab works, CT scans and may be biopsies to confirm their findings. Even after diagnosis, staging and assessing treatment depends on insensitive imaging or low specificity blood work.[6,7]

1.2 Cancer Biomarkers

The use of "biomarkers" to screen, diagnose, stage and assess response of cancers to treatment have sparked a massive amount of research in order to develop sensitive and fast caner diagnostics at low cost. Biomarker in general is a molecule expressed in body fluid and can be correlated to a specific condition or disease [8,9] and can be proteins,[10,11] RNA,[12] DNA[13] or small molecules. [14,15] The change in expression level of biomarkers has been correlated to many diseases like different types of cancer, parkinsonism, metabolic disorders and infectious diseases. Due to the non-invasive nature of biomarker testing, they represented excellent candidates for development of rapid, sensitive and cost-effective testing techniques.[16]

1.3 Point-of-care (POC) testing

Point-of-care (POC) testing refers to any testing technique that can be performed at the point of care which can be home, doctor's office or remote area where conventional laboratory testing cannot be integrated.[17] World Health Organization (WHO) Sexually Transmitted Disease Diagnostics Initiative specified "ASSURED" criteria for POC testing in resource-limited settings.[18] ASSURED criteria describe the characteristics for ideal POC as follow:

- Affordable by those at risk
- Sensitive (few false-negatives)

- Specific (few false-positives)
- User-friendly (simple to perform and requiring minimal training)
- Rapid (to enable treatment at first visit) and Robust (does not require refrigerated storage)
- Equipment-free
- Delivered to those who need it

Current cancer diagnostics and screening rely on well-established techniques like magnetic resonance imaging (MRI), computed tomography (CT) scan and pathological examination. Although these techniques can specifically detect cancer, still they lack required sensitivity for early diagnosis and accurate staging of the disease resulting in late diagnosis with high rate of false negatives. In addition, most of these techniques require centralized laboratories with highly trained operators making them cost-prohibitive and inaccessible for many patients.[19,20]

Recently, more sensitive tests have been proposed like prostate specific antigen (PSA) test for prostate cancer screening,[21] Guaiac-based fecal occult blood test (gFOBT) for colorectal cancer,[22] and Pap test and human papilloma virus (HPV) DNA test for cervical cancer.[23] These tests promised high sensitivity for early diagnosis and staging of cancer state but suffered from low specificity issues. For example, PSA test resulted in what has been known as "prostate cancer epidemic" in USA due to overdiagnosis and unnecessary biopsies and treatment of prostate cancer associated with adaption of the test as an annual screening technique.[24] This low specificity is attributed to change in the levels of expression of the selected biomarkers in conditions other than cancer like inflammation or infection.

To overcome limitations associated with low specificities of single biomarker assay, analyzing several biomarkers has been suggested as an alternate approach to enhance assays clinical significance. Multiplexing biomarkers showed potential in improving diagnostic outcomes and screening for prostate cancer,[25] oral cancer,[26,27] breast cancer,[28] lung cancer,[29] ovarian cancer,[30] bladder cancer[31] and colorectal cancer.[32]

Development of sensitive detection techniques for protein biomarkers has been an engine for proposal of new cancer diagnostic strategies. Current gold standard technique for protein detection is enzyme linked immunosorbent assay (ELISA). ELISA has not been a very successful POC test due to need of bulky instruments and relatively high cost. Other techniques for protein biomarker quantification include LC/MS,[33] protein microarrays[34] and gel electrophoresis.[35] Although, these methods promised good sensitivity and multiplexing capabilities the are still expensive and require bulky instruments and highly trained operators.

1.4 Microfluidics as POC diagnostics

Microfluidics by definition is the technique that process and manipulate small volumes of fluids. Microfluidics have been a workhorse for development of multiplexed protein assays offering the ability to achieve high sensitivity with very low amounts of samples. Inherently, microfluidics possesses the characteristics that qualify them for POC testing with low cost of production, integrated detection and ease of miniaturization for complex fluid handling. [36,37,38] In fact, microfluidics fulfils most of the characteristics ascribed by WHO for POC diagnostic techniques. Due to high surface area to volume ratio, microfluidic chambers served as an accelerator for immunoassay due to improved antibody-antigen interaction kinetics. This improved interaction helped reduce assay time from hours to minutes and improved assay sensitivities.[39] Microfluidics also does not require external sophisticated equipment for normal

operation and can be operated by micro pumps. Signals generated in microfluidics can be electrochemical, luminescence, fluorescence or colorimetric signal that can be captured and quantified using simple devices like Charge Coupled Detector (CCD) camera or even smartphone camera.[40]

1.5 Microfluidic device fabrication

Production of microfluidic devices have seen huge advances over years (Fig 1.2). The initial techniques for producing microfluidic systems were clean room micro-fabrication from silicon and glass. In 1970s, soft elastomeric micromolding chemistry was introduced and used in early 1980 for microfluidic production.[41,42] Late 1990s, Polydimethylsiloxane (PDM) leaded soft lithography to be the most popular technique for production of microfluidic systems due to its transparency, elasticity, surface characters and tendency to adsorb to glass and plastic.[43] PDMS-based microfluidics had major limitations mainly due to its hydrophobic surface nature that prompted irreversible adsorption of hydrophobic molecules, incompatibility with organic solvents and deformability under high pressure conditions.[44] PDMS-based microfluidics is still widely used as platform for electrochemical and chemiluminescence biosensors due to its electrochemical inertness and excellent transparency.

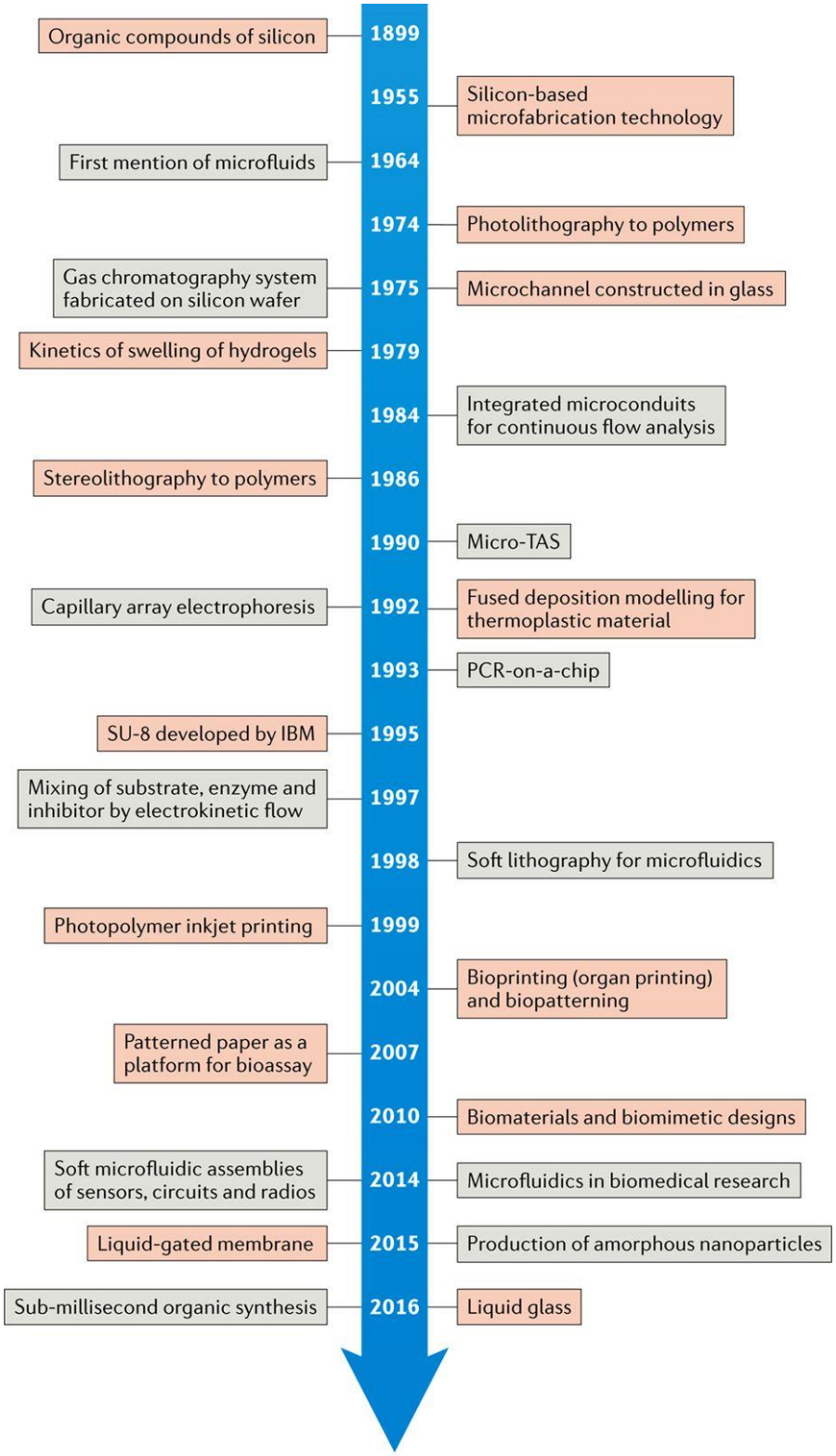

Fig. 1. **2** Overview of the development of microfluidic manufacturing materials (grey) and techniques (red). Reproduced with permission from [44]. Copyright (2017) Springer Nature

1.6 3D printed microfluidics

In recent years, the ability to convert computer assisted design (CAD) files into 3D-printed pieces, also known as additive manufacturing, has sparked significant progress in the field of diagnostics.[45] 3D printing has been utilized in a wide spectrum of applications with excellent design and performance. As an additive manufacturing technique, production costs are lower compared to traditional subtractive manufacturing techniques like milling or ablation due to reduction of the labor and material cost. In addition, the same 3D printer can be used to produce different devices and parts without the need for pre-fabrication changes usually required in subtractive manufacturing techniques. [46,47] These criteria make 3D printing a valuable tool in prototyping, testing and production of tools and equipment for analytical and diagnostic laboratories. In principle, CAD files of previously reported devices can be downloaded and printed in any laboratory, so that advanced diagnostic tools can be directly utilized by researchers without the need for purchase from a commercial vendor. This approach has the potential to bring advanced diagnostic tools more rapidly to the research lab than ever before.

3D printed microfluidic devices have been used to fabricate semi and fully automated diagnostic approaches for diseases like cancer,[48,49] infectious diseases,[50,51,52] and xenobiotic genotoxicity.[53] 3D printing also can make tailored supporting devices that improve performance of existing diagnostics like spectrophotometers[54] and PCR devices[55] and to support smartphone integration for remote sensing.[56,57] The ability to print materials with special properties allows for the creation of new equipment that can dramatically reduce the cost of diagnostic devices like SPR.[58] All these applications used 3D printing for cost-effective multifunctional production to integrate several functions in one device.[59]

Fabrication of diagnostic devices with embedded electronics and circuits have also been completed by 3D printing. The ability to print different materials simultaneously permitted the fabrication of electrodes incorporated into insulator plastic matrices with subsequent electrochemical detection of metals,[60,61,62] organic compounds[63,64] and biologically active molecules.[65] 3D printing avoids disadvantages associated with screen printing like the need for masking and drying steps and allows better resolution and faster fabrication.[66]

1.7 Enzyme-based signal amplification

Construction of sandwich immunoassay structure on electrode surface has been a widely used approach to label captured target analytes with secondary detection antibodies which in turn are bounded to labeling enzyme. This approach provides higher specificity and reduce background noise as it does not only rely on specificity of primary antibody but also on the selectivity of the secondary antibodies.[67] Using enzyme labels improved the sensitivity of such assays due to signal amplification powered by the catalytic activity of the enzyme that magnify the signal corresponding to one target analyte molecules hundreds of times in few seconds.[68] Recently, labels carrying multiple enzymes have been studied to achieve ultra-high sensitivity. Previous reports immobilized multiple horse radish peroxidase (HRP), alkaline phosphatase (ALP) or glucose oxidase (GOx) on carbon nanotubes, nanoparticles, graphene or magnetic beads to amplify electrochemical signals.[69,70,71] Degree of signal amplification is directly dependent on the enzyme turn over number which is “The maximal number of molecules of substrate converted to product per active site per unit time when the enzyme is saturated with substrate”.[72] Turn over numbers for commonly used enzyme labels like HRP, ALP or GOx are hundreds to thousands substrate molecules per second. These enzymes also can be integrated with different substrates that can produce different signals.

1.8 Signal transduction in microfluidic systems

Microfluidics can be integrated with variable types of signal transduction strategies including electrochemical, luminescence and colorimetric techniques. The signal transform biomolecule analytes concentration into a measurable signal as a result of physicochemical change happening at sensing layer. The sensitivity of the assay will depend also on the concentration of substrate and its response to minute changes in the labels. Based on the signal generation strategy, microfluidics can be classified into electrochemical, chemiluminescence, electrochemiluminescence, colorimetric, fluorescence and surface plasmon resonance (SPR) systems.

A. Electrochemical microfluidic systems

Electrochemical microfluidic biosensors utilize a change in current, impedance, potential or conductance as a signal that is correlated to specific analyte concentration. In protein biosensors, a recognition biomolecule usually capture antibodies are immobilized on a conductive electrode that is maintained in contact with reference and counter electrodes through aqueous electrolyte solution. Most common reference electrode is Ag/AgCl electrodes while platinum, gold and carbon are examples of common counter electrodes. Electrochemical sensors hold a promising approach for developing POC sensors due to its high sensitivity, ease of automation, low cost and relatively simple instrumentation.

Ability to immobilize antibodies on electrode with high surface coverage is a critical step in developing electrochemical biosensors. Working electrodes have been fabricated from a spectrum of materials including metals like gold and silver, carbon based materials like pyrolytic graphite and screen printed carbon, or nanoparticles like gold, silver and platinum nanoparticles.[73] depending on the nature of the working electrode, antibodies are covalently immobilized onto gold nanoparticle,[71] carbon nanotubes,[74] polymeric films[75] or

attached to surface through passive adsorption. Antibodies immobilized onto working electrodes serves as capture agents that selectively separate target analyte proteins from different matrices.

Most electrochemical sensors adapt sandwich immunoassay protocol for separation and quantitation of target analytes. Each enzyme label will produce high number of soluble electroactive species in less than a second that result in a large electrochemical signal. But sandwich immunoassay protocol in electrochemical systems usually places the enzyme away from the electrode surface which require the use of mediator to shuttle electrons form electrode surface to enzyme. Mediators are usually an electroactive species that can undergo redox reaction on the electrode surface. Commonly used mediators include quinones, phenolic compounds and ferrocenes ex. Hydroquinone, anthraquinone, dopamine and ferrocene methanol.[76,77] Alternatively, systems modified with carbon based carriers[78,79] or nucleic acid[80] have been introduced to eliminate the need of mediator and shuttle electrons directly to enzyme molecules (Fig. 1.3).

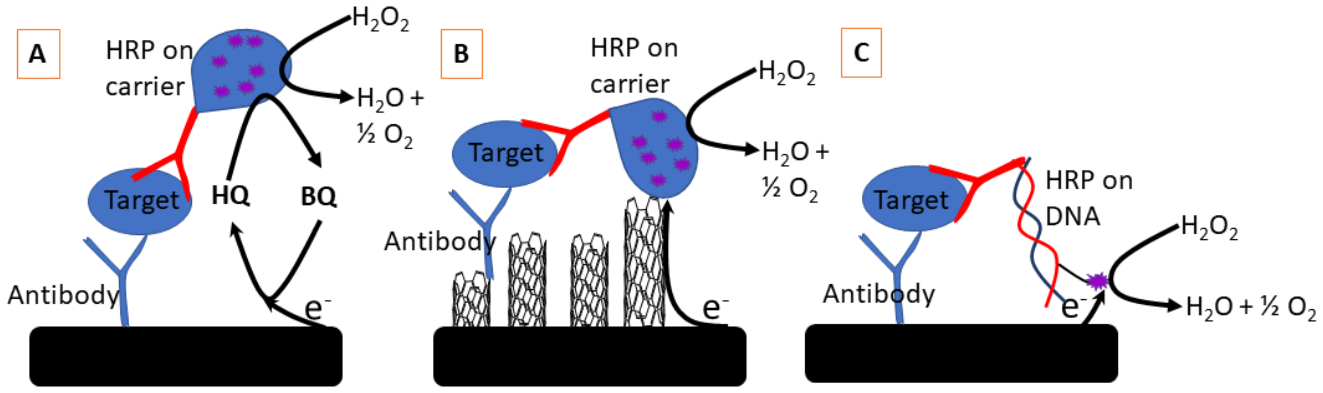

Fig. 1. 3 strategies of electron transfer from electrode surface to labelling enzyme. (A) Use of mediator hydroquinone (HQ) to shuttle electrons from electrode surface to HRP and get oxidized to benzoquinone (BQ). (B) Use of single wall carbon nanotubes as an electron carrier that eliminate the need for mediators. (C) Labelling detection antibodies with DNA carrying HRP which brings the enzyme closer to electrode surface.

Integration of electrochemical sensor in microfluidic devices have been an accessible strategy to develop POC diagnostics that can be used to quantify multiple proteins simultaneously (multiplexing). This is due to the ease of design and integration of multiple electrodes in a single microfluidic channel and availability of instrumentation to measure up to 32 electrochemical signals simultaneously.[81,82]

B. Chemiluminescence microfluidic systems

Similar to electrochemical microfluidic systems, chemiluminescence systems utilized sandwich immunoassay protocol format to label target antigens with enzyme. Signals are generated by a chemical reaction that yields an intermediate excited state that undergo radiative relaxation to ground state. Several approaches to improve the chemiluminescence sensor sensitivity have been studied including the use of photomultiplier tube to capture light, improve the substrate quantum yield, development of quantum dots, and recently use of multi-labeled enzyme systems.[83,84,85] chemiluminescence sensors promise very high sensitivity, ability to capture signals using CCD or smartphone camera and ability to generate signal without the need for sophisticated electronic connections.[86] HRP and ALP are the most common enzymes utilized in chemiluminescence microfluidic sensors. Luminol and its enhanced derivatives are most frequently and most efficient chemiluminescence substrates for the development of light in microfluidic systems. Luminol has been linked to ligands through its amine group with the loss of its quantum yield while its derivatives like iso-luminol did not suffer from such drawback. Luminol reacts with hydrogen peroxide in presence of HRP to form a stable excited intermediate that relax to ground state by emitting light at 425 nm (Fig. 1.4)

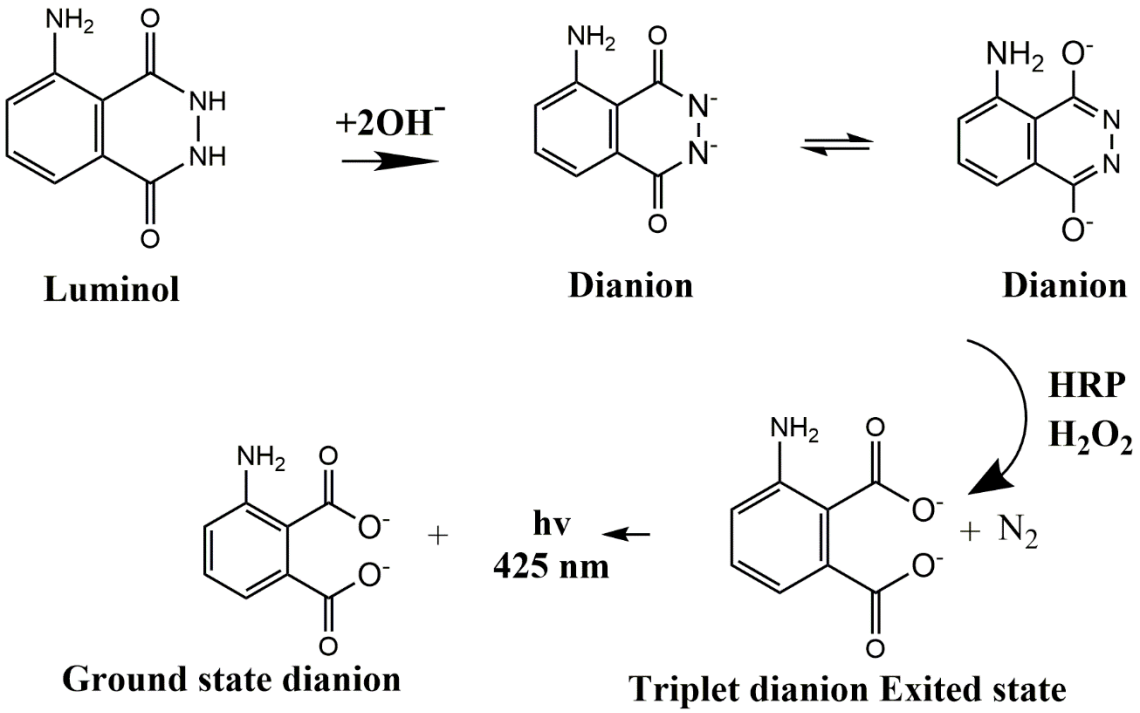

Fig. 1. 4 Mechanism of the light generation from reaction of Luminol with hydrogen peroxide in presence of HRP. Luminol is exited to triplet dianion state in presence of HRP and hydrogen peroxide which undergo radiative relaxation to ground state by emitting light at 425 nm.

Several POC microfluidic chemiluminescence sensors have been developed to quantify proteins,[87] DNA,[88] RNA[89] and even small molecules.[90] Emitted light can be captured in dark on an x-ray film or using CCD camera which reduce the background noise associated with colorimetric and electrochemical techniques. Recently, capturing and quantifying luminescence is becoming more affordable due rapid development in smartphone cameras which makes chemiluminescence sensors a more appealing choice or POC diagnostics.

C. *Electrochemiluminescence microfluidic systems*

Electrochemiluminescent labels generate light when they are stimulated by electricity in appropriate chemical environment. Due to the confined nature of luminescence near the electrode surface, electrochemiluminescence sensors are excellent tool to multiplex analytes. Electrochemiluminescence assay usually provide a wider dynamic range for assay compared to other techniques while maintain excellent sensitivity. [91,92,93]

In electrochemiluminescence systems a lumiphore and its co-reactant are oxidized near the electrode surface, then react to produce luminescence (Fig. 1. 5).[94] Many organic molecules have shown promising electrochemiluminescence characteristics. Tris(2,2′-bipyridine)ruthenium(II) ($Ru(bpy)_3^{2+}$) is one of the most studied electrochemiluminescence molecules due to its low molecular weight and ease to produce multi-labelled antibodies. The major advantage of ECL over fluorescence is the ability to excite the luminophore without the need for excitation light which in turn greatly reduces background noise. Backed with these advantages ECL has been utilized commercially in POC diagnostics like Mesoscale Discovery® and Roche® POC systems. Commercial ECL systems for detection of clinically relevant target analytes like proteins, hormones, steroids, drugs and toxins have been developed with high sensitivity and selectivity.[95]

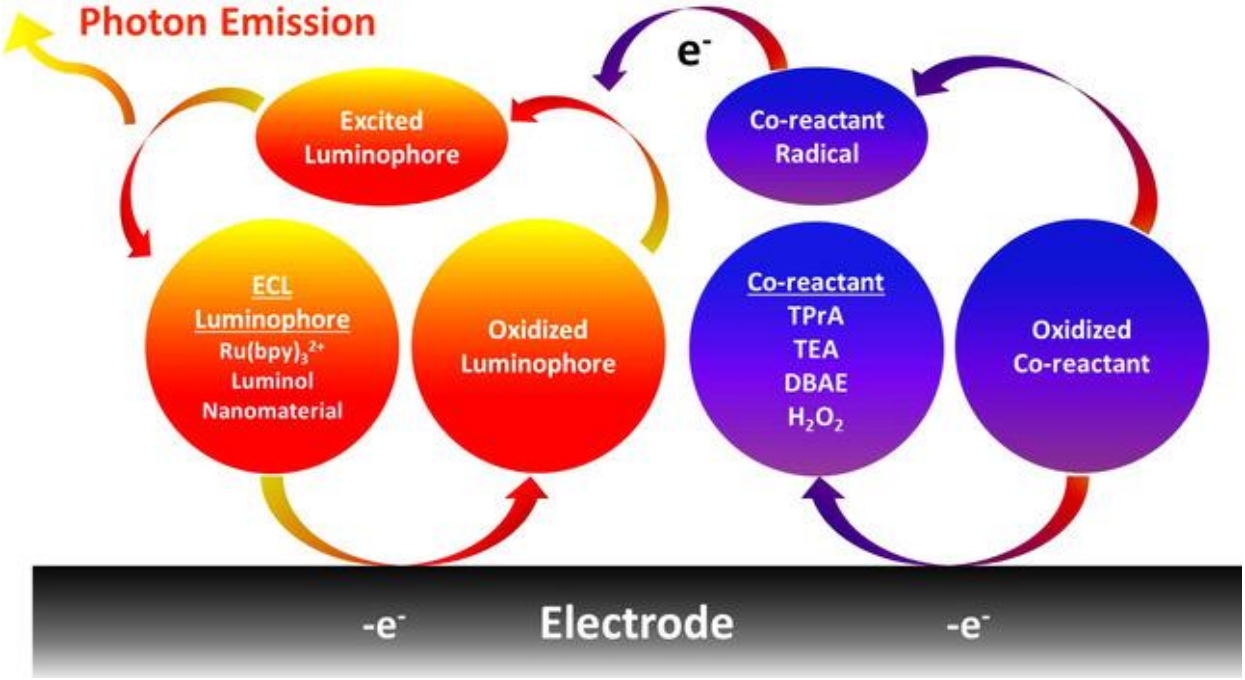

Fig. 1. 5 Mechanism of electrochemiluminescence generation in aqueous solution. Luminophore and its co-reactant are oxidized at the electrode surface. The co-reactant forms a radical that reduce the oxidized luminophore. Excited molecules return to original state by emitting light. Reproduced with permission from [94]. Copyright (2017) Wiley

1.9 Summary and Overview of dissertation

Early detection and staging of cancer is a crucial step in more efficient cancer control and treatment. Despite advances in conventional diagnostic techniques like mammography and computed topography (CT), still early cancer diagnosis is a challenge. Recent developments in proteomics and immunology suggested that using protein biomarkers as a cancer detection tool may offer fast, reliable, non-invasive and cost-effective approach for early diagnosis. In this thesis we would like to investigate several microfluidic approaches for improved cancer diagnostics with better sensitivities and improved stability. In order to achieve a POC testing requirement we also studied the utilization of desktop 3D printers to prototype and fabricate accessible diagnostic tools.

In this chapter, Chapter 1, we provided a description of the status quo of cancer and its current diagnostic tools. The major characteristics of POC diagnostic system have been discussed while highlighting the significance of using microfluidics to develop and improve cancer screening assays. The chapter also provided an insight into enzyme amplification as strategy to increase assay sensitivity and achieve low LOD. Finally, a detailed description of microfluidic fabrication techniques and signal transduction in microfluidic systems have been explained with detailed explanation of advantages provided by each technique.

Chapter 2 describes Fe_3O_4@GO composite as a signal-transducing label in a sandwich immunoassay to detect prostate cancer biomarkers on screen-printed carbon electrode arrays housed in simple microfluidic devices. Antibodies for Prostate Specific Antigen (PSA) and Prostate Specific Membrane antigen (PSMA) were covalently attached to Fe_3O_4@GO, and the resulting bio-composite was used to isolate target antigens from serum and serve as a signal-transducing label for electrochemical detection. The sensor surfaces of the array were coated with electrochemically reduced graphene oxide to improve conductivity and increase surface area, and capture antibodies were attached through either adsorption or covalent binding to residual carboxylic groups on surface. An optimized simple microfluidic system was used to deliver reagents to the electrode arrays and wash/remove unbound species. This sandwich assay based on catalytic reduction of hydrogen peroxide by Fe_3O_4@GO exhibited detection limits of 15 fg/mL for PSA and 4.8 fg /mL for PSMA. Accuracy was validated by measuring PSA and PSMA in patient samples and results showed good correlation to values obtained from standard ELISA.

Chapter 3 introduced a low-cost pipette tip-based ELISA platform “ELISA in a Tip” as a next generation assay tool with better sensitivity, shorter incubation time, low sample and reagent volumes than traditional ELISA. This platform could serve as a simple microfluidic adaptor that

encourages to blend microfluidic advancement, multiplexing and smartphone integration with widely practiced gold standard ELISA without need for major overhaul of current infrastructure in hospitals and testing laboratories. We applied this approach in detection of four cancer protein biomarkers, a prostate cancer panel with detection limits in low picogram range and a wider dynamic range compared to plate-based ELISA. Recoveries from spiked human serum samples were from 80% to 120% with standard deviation less than 15 %. We demonstrated the ability to utilize smartphone-based detection in our colorimetric detection approach that could be an ideal candidate for offering telemedicine to remote areas where quantitation assays for diseases like cancer are challenged. Using these techniques, we showed simultaneous detection of 4 biomarkers PSA, VEGF, IGFBP3 and CD-14 on an 8-channel pipette tip array with detection limits ranging from 1 pg mL^{-1} to 25 pg mL^{-1}. We validated our method by calculating % recoveries from spiked human serum and observed acceptable recoveries ±20%. We were able to utilize colorimetry and chemiluminescence as a detectable signal output that can be measured using smartphone without compromising assay sensitivity.

Chapter 4 explain development of 3D printed multifunctional array capable of onsite differentiation between metastatic and nonmetastatic head and neck squamous cell carcinoma (HNSCC). This chip first lyses cells in a novel microfluidic lysis chamber utilizing combination of mechanical and chemical lysis. Once cells are lysed, desmoglein3 (DSG3), vascular endothelial growth factor-C (VEGF-C) and beta tubulin (β-Tub) will be quantified in an 8 chambers detection compartment. Reagents and samples were delivered automatically to detection compartment using programmable micro pumps controlled by Arduino® microcontroller. Use of streptavidin poly(HRP) as a label with enhanced (West femto®) luminol substrate allowed sub femtogram LOD for the protein biomarkers. Bovine serum albumin (BSA) was used as a negative control to

normalize the chemiluminescence signal. Chemiluminescence signals were captured using CCD camera for 15s and quantified using GeneSnap® software. Assay time was less than 45 min and promised detection of biomarkers at single cell expression level.

Chapter 5 provided a comprehensive study of antibody immobilization strategies on screen printed carbon electrodes. This is a crucial step in developing biosensor arrays as it would affect assay sensitivity, sensor stability and detection limits. The performance of immunosensors prepared using six different antibody immobilization techniques on screen-printed carbon electrodes was compared. anti-HRP was utilized as a model immunoglobulin (IgG) antibody to determine HRP in calf serum by performing amperometry in the presence of H_2O_2 and HQ. Results presented shed insights regarding the influence of the immobilization protocol on the coverage of antibodies and fraction of active ones immobilized, LOD, dynamic range, reproducibility and storage stability. Against previous findings, results demonstrated that while antibody orientation did not have a significant effect on LOD, it did enhance the dynamic range of the immunoassay.

1.9 References

[1] Cancer Facts and Statistics | American Cancer Society https://www.cancer.org/research/cancer-facts-statistics.html (accessed Jul 1, 2019).

[2] Ferlay, J.; Colombet, M.; Soerjomataram, I.; Mathers, C.; Parkin, D. M.; Piñeros, M.; Znaor, A.; Bray, F. Estimating the Global Cancer Incidence and Mortality in 2018: GLOBOCAN Sources and Methods. *Int. J. Cancer* **2019**, *144* (8), 1941–1953.

[3] Tian, J.-Y.; Guo, F.-J.; Zheng, G.-Y.; Ahmad, A. Prostate Cancer: Updates on Current Strategies for Screening, Diagnosis and Clinical Implications of Treatment Modalities. *Carcinogenesis* **2018**, *39* (3), 307–317.

[4] Berry, D. A.; Cronin, K. A.; Plevritis, S. K.; Fryback, D. G.; Clarke, L.; Zelen, M.; Mandelblatt, J. S.; Yakovlev, A. Y.; Habbema, J. D. F.; Feuer, E. J. Effect of Screening and Adjuvant Therapy on Mortality from Breast Cancer. *N. Engl. J. Med.* **2005**, *353* (17), 1784–1792.

[5] Gulati, R.; Gore, J. L.; Etzioni, R. Comparative Effectiveness of Alternative Prostate-Specific Antigen--Based Prostate Cancer Screening Strategies: Model Estimates of Potential Benefits and Harms. *Ann. Intern. Med.* **2013**, *158* (3), 145–153.

[6] Tørring, M. L.; Frydenberg, M.; Hansen, R. P.; Olesen, F.; Vedsted, P. Evidence of Increasing Mortality with Longer Diagnostic Intervals for Five Common Cancers: A Cohort Study in Primary Care. *Eur. J. Cancer* **2013**, *49* (9), 2187–2198.

[7] Hamilton, W. Cancer Diagnosis in Primary Care. *Br. J. Gen. Pract.* **2010**, *60* (571), 121–128.

[8] Manne, U.; Srivastava, R.-G.; Srivastava, S. Keynote Review: Recent Advances in Biomarkers for Cancer Diagnosis and Treatment. *Drug Discov. Today* **2005**, *10* (14), 965–976.

[9] Strimbu, K.; Tavel, J. A. What Are Biomarkers? *Curr. Opin. HIV AIDS* **2010**, *5* (6), 463–466.

[10] Boschetti, E.; D'Amato, A.; Candiano, G.; Righetti, P. G. Protein Biomarkers for Early Detection of Diseases: The Decisive Contribution of Combinatorial Peptide Ligand Libraries. *J. Proteomics* **2018**, *188*, 1–14.

[11] Rifai, N.; Gillette, M. A.; Carr, S. A. Protein Biomarker Discovery and Validation: The Long and Uncertain Path to Clinical Utility. *Nat. Biotechnol.* **2006**, *24* (8), 971.

[12] Xi, X.; Li, T.; Huang, Y.; Sun, J.; Zhu, Y.; Yang, Y.; Lu, Z. J. RNA Biomarkers: Frontier of Precision Medicine for Cancer. *Non-Coding RNA* **2017**, *3* (1).

[13] Ziegler, A.; Koch, A.; Krockenberger, K.; Großhennig, A. Personalized Medicine Using DNA Biomarkers: A Review. *Hum. Genet.* **2012**, *131* (10), 1627–1638.

[14] Havelund, J. F.; Heegaard, N. H. H.; Færgeman, N. J. K.; Gramsbergen, J. B. Biomarker Research in Parkinson's Disease Using Metabolite Profiling. *Metabolites* **2017**, *7* (3).

[15] Tan, W.; He, J.; Deng, J.; Yang, X.; Cui, L.; Ran, R.; Du, G.; Jiang, X. Small Molecule Metabolite Biomarkers for Hepatocellular Carcinoma with Bile Duct Tumor Thrombus Diagnosis. *Sci. Rep.* **2018**, *8* (1), 3309.

[16] Selleck, M. J.; Senthil, M.; Wall, N. R. Making Meaningful Clinical Use of Biomarkers. *Biomark. Insights* **2017**, *12*.

[17] Hayes, B.; Murphy, C.; Crawley, A.; O'Kennedy, R. Developments in Point-of-Care Diagnostic Technology for Cancer Detection. *Diagnostics* **2018**, *8* (2).

[18] Drain, P. K.; Hyle, E. P.; Noubary, F.; Freedberg, K. A.; Wilson, D.; Bishai, W.; Rodriguez, W.; Bassett, I. V. Evaluating Diagnostic Point-of-Care Tests in Resource-Limited Settings. *Lancet Infect. Dis.* **2014**, *14* (3), 239–249.

[19] Smith, R. A.; Andrews, K. S.; Brooks, D.; Fedewa, S. A.; Manassaram-Baptiste, D.; Saslow, D.; Brawley, O. W.; Wender, R. C. Cancer Screening in the United States, 2017: A Review of Current American Cancer Society Guidelines and Current Issues in Cancer Screening. *CA. Cancer J. Clin.* **2017**, *67* (2), 100–121.

[20] Liu, B.; F. Rusling, J. Cancer Diagnostics. *J. Mater. Chem. B* **2018**, *6* (17), 2507–2509.

[21] Houston Keisha A.; King Jessica; Li Jun; Jemal Ahmedin. Trends in Prostate Cancer Incidence Rates and Prevalence of Prostate Specific Antigen Screening by Socioeconomic Status and Regions in the United States, 2004 to 2013. *J. Urol.* **2018**, *199* (3), 676–682.

[22] Wolf, A. M. D.; Fontham, E. T. H.; Church, T. R.; Flowers, C. R.; Guerra, C. E.; LaMonte, S. J.; Etzioni, R.; McKenna, M. T.; Oeffinger, K. C.; Shih, Y.-C. T.; et al. Colorectal Cancer Screening for Average-Risk Adults: 2018 Guideline Update from the American Cancer Society. *CA. Cancer J. Clin.* **2018**, *68* (4), 250–281.

[23] Committee on Practice Bulletins—Gynecology. ACOG Practice Bulletin Number 131: Screening for Cervical Cancer. *Obstet. Gynecol.* **2012**, *120* (5), 1222–1238.

[24] Adami, H.-O. The Prostate Cancer Pseudo-Epidemic. *Acta Oncol.* **2010**, *49* (3), 298–304.

[25] Rusling, J. F. Multiplexed Electrochemical Protein Detection and Translation to Personalized Cancer Diagnostics. *Anal. Chem.* **2013**, *85* (11), 5304–5310.

[26] Malhotra, R.; Patel, V.; Chikkaveeraiah, B. V.; Munge, B. S.; Cheong, S. C.; Zain, R. B.; Abraham, M. T.; Dey, D. K.; Gutkind, J. S.; Rusling, J. F. Ultrasensitive Detection of Cancer Biomarkers in the Clinic by Use of a Nanostructured Microfluidic Array. *Anal. Chem.* **2012**, *84* (14), 6249–6255.

[27] Arellano-Garcia, M. E.; Hu, S.; Wang, J.; Henson, B.; Zhou, H.; Chia, D.; Wong, D. T. Multiplexed Immunobead-Based Assay for Detection of Oral Cancer Protein Biomarkers in Saliva. *Oral Dis.* **2008**, *14* (8), 705–712.

[28] Chen, I.-H.; Aguilar, H. A.; Paez Paez, J. S.; Wu, X.; Pan, L.; Wendt, M. K.; Iliuk, A. B.; Zhang, Y.; Tao, W. A. Analytical Pipeline for Discovery and Verification of Glycoproteins from Plasma-Derived Extracellular Vesicles as Breast Cancer Biomarkers. *Anal. Chem.* **2018**, *90* (10), 6307–6313.

[29] Jia, J.; Wang, W.; Meng, W.; Ding, M.; Ma, S.; Wang, X. Development of a Multiplex Autoantibody Test for Detection of Lung Cancer. *PLOS ONE* **2014**, *9* (4), e95444.

[30] Shadfan, B. H.; Simmons, A. R.; Simmons, G. W.; Ho, A.; Wong, J.; Lu, K. H.; Bast, R. C.; McDevitt, J. T. A Multiplexable, Microfluidic Platform for the Rapid Quantitation of a Biomarker Panel for Early Ovarian Cancer Detection at the Point-of-Care. *Cancer Prev. Res. (Phila. Pa.)* **2015**, *8* (1), 37–48.

[31] Rosser, C. J.; Dai, Y.; Miyake, M.; Zhang, G.; Goodison, S. Simultaneous Multi-Analyte Urinary Protein Assay for Bladder Cancer Detection. *BMC Biotechnol.* **2014**, *14* (1), 24.

[32] Ostendorff, H. P.; Awad, A.; Braunschweiger, K. I.; Liu, Z.; Wan, Z.; Rothschild, K. J.; Lim, M. J. Multiplexed VeraCode Bead-Based Serological Immunoassay for Colorectal Cancer. *J. Immunol. Methods* **2013**, *400–401*, 58–69.

[33] Sandin, M.; Chawade, A.; Levander, F. Is Label-Free LC-MS/MS Ready for Biomarker Discovery? *PROTEOMICS – Clin. Appl.* **2015**, *9* (3–4), 289–294.

[34] Borrebaeck, C. A. K. Precision Diagnostics: Moving towards Protein Biomarker Signatures of Clinical Utility in Cancer. *Nat. Rev. Cancer* **2017**, *17* (3), 199–204.

[35] Kitamura, Y.; Usami, R.; Ichihara, S.; Kida, H.; Satoh, M.; Tomimoto, H.; Murata, M.; Oikawa, S. Plasma Protein Profiling for Potential Biomarkers in the Early Diagnosis of Alzheimer's Disease. *Neurol. Res.* **2017**, *39* (3), 231–238.

[36] Whitesides, G. M. The Origins and the Future of Microfluidics. *Nature* **2006**, *442* (7101), 368.

[37] Sackmann, E. K.; Fulton, A. L.; Beebe, D. J. The Present and Future Role of Microfluidics in Biomedical Research. *Nature* **2014**, *507* (7491), 181–189.

[38] K. Sia, S.; J. Kricka, L. Microfluidics and Point-of-Care Testing. *Lab. Chip* **2008**, *8* (12), 1982–1983.

[39] Henares, T. G.; Mizutani, F.; Hisamoto, H. Current Development in Microfluidic Immunosensing Chip. *Anal. Chim. Acta* **2008**, *611* (1), 17–30.

[40] G. Rackus, D.; H. Shamsi, M.; R. Wheeler, A. Electrochemistry, Biosensors and Microfluidics: A Convergence of Fields. *Chem. Soc. Rev.* **2015**, *44* (15), 5320–5340.

[41] Aumiller, G. D.; Chandross, E. A.; Tomlinson, W. J.; Weber, H. P. Submicrometer Resolution Replication of Relief Patterns for Integrated Optics. *J. Appl. Phys.* **1974**, *45* (10), 4557–4562.

[42] Masuda, S.; Washizu, M.; Nanba, T. Novel Method of Cell Fusion in Field Constriction Area in Fluid Integration Circuit. *IEEE Trans. Ind. Appl.* **1989**, *25* (4), 732–737.

[43] Duffy, D. C.; McDonald, J. C.; Schueller, O. J. A.; Whitesides, G. M. Rapid Prototyping of Microfluidic Systems in Poly(Dimethylsiloxane). *Anal. Chem.* **1998**, *70* (23), 4974–4984.

[44] Hou, X.; Zhang, Y. S.; Santiago, G. T.; Alvarez, M. M.; Ribas, J.; Jonas, S. J.; Weiss, P. S.; Andrews, A. M.; Aizenberg, J.; Khademhosseini, A. Interplay between Materials and Microfluidics. *Nat. Rev. Mater.* **2017**, *2* (5), 17016.

[45] Waheed, S.; M. Cabot, J.; P. Macdonald, N.; Lewis, T.; M. Guijt, R.; Paull, B.; C. Breadmore, M. 3D printed microfluidic devices: enablers and barriers. *Lab. Chip* **2016**, *16*, 1993–2013, doi:10.1039/C6LC00284F.

[46] Why 3D Printing Could Be A Manufacturing And Logistics Game Changer Available online: https://www.manufacturing.net/blog/2013/10/why-3d-printing-could-be-manufacturing-and-logistics-game-changer (accessed on Apr 30, 2018).

[47] Au, A. K.; Lee, W.; Folch, A. Mail-order microfluidics: evaluation of stereolithography for the production of microfluidic devices. *Lab. Chip* **2014**, *14*, 1294–1301, doi:10.1039/C3LC51360B.

[48] Kadimisetty, K.; Mosa, I. M.; Malla, S.; Satterwhite-Warden, J. E.; Kuhns, T. M.; Faria, R. C.; Lee, N. H.; Rusling, J. F. 3D-printed supercapacitor-powered electrochemiluminescent protein immunoarray. *Biosens. Bioelectron.* **2016**, *77*, 188–193, doi:10.1016/j.bios.2015.09.017.

[49] Damiati, S.; Peacock, M.; Leonhardt, S.; Damiati, L.; Baghdadi, M. A.; Becker, H.; Kodzius, R.; Schuster, B. Embedded Disposable Functionalized Electrochemical Biosensor with a 3D-Printed Flow Cell for Detection of Hepatic Oval Cells (HOCs). *Genes* **2018**, *9*, 89, doi:10.3390/genes9020089.

[50] Mulberry, G.; White, K. A.; Vaidya, M.; Sugaya, K.; Kim, B. N. 3D printing and milling a real-time PCR device for infectious disease diagnostics. *PLOS ONE* **2017**, *12*, e0179133, doi:10.1371/journal.pone.0179133.

[51] Singh, H.; Shimojima, M.; Shiratori, T.; An, L. V.; Sugamata, M.; Yang, M. Application of 3D Printing Technology in Increasing the Diagnostic Performance of Enzyme-Linked Immunosorbent Assay (ELISA) for Infectious Diseases. *Sensors* **2015**, *15*, 16503–16515, doi:10.3390/s150716503.

[52] Chudobova, D.; Cihalova, K.; Skalickova, S.; Zitka, J.; Rodrigo, M. A. M.; Milosavljevic, V.; Hynek, D.; Kopel, P.; Vesely, R.; Adam, V.; Kizek, R. 3D-printed chip for detection of methicillin-resistant Staphylococcus aureus labeled with gold nanoparticles. *ELECTROPHORESIS* **2015**, *36*, 457–466, doi:10.1002/elps.201400321.

[53] Kadimisetty, K.; Malla, S.; Rusling, J. F. Automated 3-D Printed Arrays to Evaluate Genotoxic Chemistry: E-Cigarettes and Water Samples. *ACS Sens.* **2017**, *2*, 670–678, doi:10.1021/acssensors.7b00118.

[54] Schäfer, M.; Bräuler, V.; Ulber, R. Bio-sensing of metal ions by a novel 3D-printable smartphone spectrometer. *Sens. Actuators B Chem.* **2018**, *255*, 1902–1910, doi:10.1016/j.snb.2017.08.207.

[55] Mendoza-Gallegos, R. A.; Rios, A.; Garcia-Cordero, J. L. An Affordable and Portable Thermocycler for Real-Time PCR Made of 3D-Printed Parts and Off-the-Shelf Electronics. *Anal. Chem.* **2018**, *90*, 5563–5568, doi:10.1021/acs.analchem.7b04843.

[56] Wang, L.-J.; Sun, R.; Vasile, T.; Chang, Y.-C.; Li, L. High-Throughput Optical Sensing Immunoassays on Smartphone. *Anal. Chem.* **2016**, *88*, 8302–8308, doi:10.1021/acs.analchem.6b02211.

[57] Chen, Y.; Fu, Q.; Li, D.; Xie, J.; Ke, D.; Song, Q.; Tang, Y.; Wang, H. A smartphone colorimetric reader integrated with an ambient light sensor and a 3D printed attachment for on-site detection of zearalenone. *Anal. Bioanal. Chem.* **2017**, *409*, 6567–6574, doi:10.1007/s00216-017-0605-2.

[58] Hinman, S. S.; McKeating, K. S.; Cheng, Q. Plasmonic Sensing with 3D Printed Optics. *Anal. Chem.* **2017**, *89*, 12626–12630, doi:10.1021/acs.analchem.7b03967.

[59] Rusling, J. F. Developing Microfluidic Sensing Devices Using 3D Printing. *ACS Sens.* **2018**, *3*, 522–526, doi:10.1021/acssensors.8b00079.

[60] Lee, K. Y.; Ambrosi, A.; Pumera, M. 3D-printed Metal Electrodes for Heavy Metals Detection by Anodic Stripping Voltammetry. *Electroanalysis* **2017**, *29*, 2444–2453, doi:10.1002/elan.201700388.

[61] Rymansaib, Z.; Iravani, P.; Emslie, E.; Medvidović-Kosanović, M.; Sak-Bosnar, M.; Verdejo, R.; Marken, F. All-Polystyrene 3D-Printed Electrochemical Device with Embedded Carbon Nanofiber-Graphite-Polystyrene Composite Conductor. *Electroanalysis* **2016**, *28*, 1517–1523, doi:10.1002/elan.201600017.

[62] Honeychurch, K. C.; Rymansaib, Z.; Iravani, P. Anodic stripping voltammetric determination of zinc at a 3-D printed carbon nanofiber–graphite–polystyrene electrode using a carbon pseudo-reference electrode. *Sens. Actuators B Chem.* **2018**, *267*, 476–482, doi:10.1016/j.snb.2018.04.054.

[63] Cheng, T. S.; Nasir, M. Z. M.; Ambrosi, A.; Pumera, M. 3D-printed metal electrodes for electrochemical detection of phenols. *Appl. Mater. Today* **2017**, *9*, 212–219, doi:10.1016/j.apmt.2017.07.005.

[64] Tan, C.; Nasir, M. Z. M.; Ambrosi, A.; Pumera, M. 3D Printed Electrodes for Detection of Nitroaromatic Explosives and Nerve Agents. *Anal. Chem.* **2017**, *89*, 8995–9001, doi:10.1021/acs.analchem.7b01614.

[65] Liyarita, B. R.; Ambrosi, A.; Pumera, M. 3D-printed Electrodes for Sensing of Biologically Active Molecules. *Electroanalysis 0*, doi:10.1002/elan.201700828.

[66] Lewis, J. A.; Ahn, B. Y. Device fabrication: Three-dimensional printed electronics. *Nature* **2015**, *518*, 42–43, doi:10.1038/518042a.

[67] Hosseini, S.; Vázquez-Villegas, P.; Rito-Palomares, M.; Martinez-Chapa, S. O. Advantages, Disadvantages and Modifications of Conventional ELISA. In *Enzyme-linked Immunosorbent Assay (ELISA): From A to Z*; Hosseini, S., Vázquez-Villegas, P., Rito-Palomares, M., Martinez-Chapa, S. O., Eds.; SpringerBriefs in Applied Sciences and Technology; Springer Singapore: Singapore, 2018; pp 67–115.

[68] Yang, H. Enzyme-Based Ultrasensitive Electrochemical Biosensors. *Curr. Opin. Chem. Biol.* **2012**, *16* (3), 422–428.

[69] Wu, Y.; Chen, C.; Liu, S. Enzyme-Functionalized Silica Nanoparticles as Sensitive Labels in Biosensing. *Anal. Chem.* **2009**, *81* (4), 1600–1607.

[70] Munge, B. S.; Coffey, A. L.; Doucette, J. M.; Somba, B. K.; Malhotra, R.; Patel, V.; Gutkind, J. S.; Rusling, J. F. Nanostructured Immunosensor for Attomolar Detection of Cancer Biomarker Interleukin-8 Using Massively Labeled Superparamagnetic Particles. *Angew. Chem. Int. Ed.* **2011**, *50* (34), 7915–7918.

[71] Mani, V.; Chikkaveeraiah, B. V.; Patel, V.; Gutkind, J. S.; Rusling, J. F. Ultrasensitive Immunosensor for Cancer Biomarker Proteins Using Gold Nanoparticle Film Electrodes and Multienzyme-Particle Amplification. *ACS Nano* **2009**, *3* (3), 585–594.

[72] Roskoski, R. Michaelis-Menten Kinetics. In *xPharm: The Comprehensive Pharmacology Reference*; Enna, S. J., Bylund, D. B., Eds.; Elsevier: New York, 2007; pp 1–10.

[73] Wang, G.; Zhang, L.; Zhang, J. A Review of Electrode Materials for Electrochemical Supercapacitors. *Chem. Soc. Rev.* **2012**, *41* (2), 797–828.

[74] Munge, B. S.; Fisher, J.; Millord, L. N.; Krause, C. E.; Dowd, R. S.; Rusling, J. F. Sensitive Electrochemical Immunosensor for Matrix Metalloproteinase-3 Based on Single-Wall Carbon Nanotubes. *Analyst* **2010**, *135* (6), 1345–1350.

[75] Presnova, G. V.; Rubtsova, M. Yu.; Shumyantseva, V. V.; Bulko, T. V.; Egorov, A. M. Comparative Immobilization of Antibodies on Modified Screen-Printed Graphite Electrodes. *Mosc. Univ. Chem. Bull.* **2008**, *63* (2), 71.

[76] da Silva, L. V.; de Almeida, A. K. A.; Xavier, J. A.; Lopes, C. B.; Silva, F. de A. dos S.; Lima, P. R.; dos Santos, N. D.; Kubota, L. T.; Goulart, M. O. F. Phenol Based Redox Mediators in Electroanalysis. *J. Electroanal. Chem.* **2018**, *827*, 230–252.

[77] Du, D.; Wang, J.; Lu, D.; Dohnalkova, A.; Lin, Y. Multiplexed Electrochemical Immunoassay of Phosphorylated Proteins Based on Enzyme-Functionalized Gold Nanorod Labels and Electric Field-Driven Acceleration. *Anal. Chem.* **2011**, *83* (17), 6580–6585.

[78] Yu, X.; Kim, S. N.; Papadimitrakopoulos, F.; Rusling, J. F. Protein Immunosensor Using Single-Wall Carbon Nanotube Forests with Electrochemical Detection of Enzyme Labels. *Mol. Biosyst.* **2005**, *1* (1), 70–78.

[79] Zhong, Z.; Wu, W.; Wang, D.; Wang, D.; Shan, J.; Qing, Y.; Zhang, Z. Nanogold-Enwrapped Graphene Nanocomposites as Trace Labels for Sensitivity Enhancement of Electrochemical Immunosensors in Clinical Immunoassays: Carcinoembryonic Antigen as a Model. *Biosens. Bioelectron.* **2010**, *25* (10), 2379–2383.

[80] Xia, F.; White, R. J.; Zuo, X.; Patterson, A.; Xiao, Y.; Kang, D.; Gong, X.; Plaxco, K. W.; Heeger, A. J. An Electrochemical Supersandwich Assay for Sensitive and Selective DNA Detection in Complex Matrices. *J. Am. Chem. Soc.* **2010**, *132* (41), 14346–14348.

[81] Wei, F.; Patel, P.; Liao, W.; Chaudhry, K.; Zhang, L.; Arellano-Garcia, M.; Hu, S.; Elashoff, D.; Zhou, H.; Shukla, S.; et al. Electrochemical Sensor for Multiplex Biomarkers Detection. *Clin. Cancer Res.* **2009**, *15* (13), 4446–4452.

[82][82] Munge, B. S.; Stracensky, T.; Gamez, K.; DiBiase, D.; Rusling, J. F. Multiplex Immunosensor Arrays for Electrochemical Detection of Cancer Biomarker Proteins. *Electroanalysis* **2016**, *28* (11), 2644–2658.

[83] Poznyak, S. K.; Talapin, D. V.; Shevchenko, E. V.; Weller, H. Quantum Dot Chemiluminescence. *Nano Lett.* **2004**, *4* (4), 693–698.

[84] Zhao, L.; Sun, L.; Chu, X. Chemiluminescence Immunoassay. *TrAC Trends Anal. Chem.* **2009**, *28* (4), 404–415.

[85] Roda, A.; Michelini, E.; Cevenini, L.; Calabria, D.; Calabretta, M. M.; Simoni, P. Integrating Biochemiluminescence Detection on Smartphones: Mobile Chemistry Platform for Point-of-Need Analysis. *Anal. Chem.* **2014**, *86* (15), 7299–7304.

[86] Roda, A.; Mirasoli, M.; Michelini, E.; Di Fusco, M.; Zangheri, M.; Cevenini, L.; Roda, B.; Simoni, P. Progress in Chemical Luminescence-Based Biosensors: A Critical Review. *Biosens. Bioelectron.* **2016**, *76*, 164–179.

[87] Lee, J. S.; Joung, H.-A.; Kim, M.-G.; Park, C. B. Graphene-Based Chemiluminescence Resonance Energy Transfer for Homogeneous Immunoassay. *ACS Nano* **2012**, *6* (4), 2978–2983.

[88] He, Y.; Liu, D.; He, X.; Cui, H. One-Pot Synthesis of Luminol Functionalized Silver Nanoparticles with Chemiluminescence Activity for Ultrasensitive DNA Sensing. *Chem. Commun.* **2011**, *47* (38), 10692–10694.

[89] Zhao, J.; Jin, X.; Vdovenko, M.; Zhang, L.; Yu. Sakharov, I.; Zhao, S. A WS 2 Nanosheet Based Chemiluminescence Resonance Energy Transfer Platform for Sensing Biomolecules. *Chem. Commun.* **2015**, *51* (55), 11092–11095.

[90] Hong, L.; Liu, A.-L.; Li, G.-W.; Chen, W.; Lin, X.-H. Chemiluminescent Cholesterol Sensor Based on Peroxidase-like Activity of Cupric Oxide Nanoparticles. *Biosens. Bioelectron.* **2013**, *43*, 1–5.

[91] Richter, M. M. Electrochemiluminescence (ECL). *Chem. Rev.* **2004**, *104* (6), 3003–3036.

[92] Li, L.; Chen, Y.; Zhu, J.-J. Recent Advances in Electrochemiluminescence Analysis. *Anal. Chem.* **2017**, *89* (1), 358–371.

[93] Hu, L.; Xu, G. Applications and Trends in Electrochemiluminescence. *Chem. Soc. Rev.* **2010**, *39* (8), 3275–3304.

[94] Gross, E. M.; Durant, H. E.; Hipp, K. N.; Lai, R. Y. Electrochemiluminescence Detection in Paper-Based and Other Inexpensive Microfluidic Devices. *ChemElectroChem* **2017**, *4* (7), 1594–1603.

[95] Cohen, L.; Walt, D. R. Highly Sensitive and Multiplexed Protein Measurements. *Chem. Rev.* **2019**, *119* (1), 293–321.

Chapter Two

Fe_3O_4 Nanoparticles on Graphene Oxide Sheets for Isolation and Ultrasensitive Amperometric Detection of Cancer Biomarker Proteins

2.1 Abstract

Ultrasensitive mediator-free electrochemical detection for biomarker proteins was achieved at low cost using a novel composite of Fe_3O_4 nanoparticles loaded onto graphene oxide (GO) nano-sheets (Fe_3O_4@GO). This paramagnetic Fe_3O_4@GO composite (1 µm size range) was decorated with antibodies against prostate specific antigen (PSA) and prostate specific membrane antigen (PSMA), and then used to first capture these biomarkers and then deliver them to an 8-sensor detection chamber of a microfluidic immunoarray. Screen-printed carbon sensors coated with electrochemically reduced graphene oxide (ERGO) and a second set of antibodies selectively capture the biomarker-laden Fe_3O_4@GO particles, which subsequently catalyze hydrogen peroxide reduction to detect PSA and PSMA. Accuracy was confirmed by good correlation between patient serum assays and enzyme-linked immuno-sorbent assays (ELISA). Excellent detection limits (LOD) of 15 fg/mL for PSA and 4.8 fg/mL for PSMA were achieved in serum. The LOD for PSA was 1000-fold better than the only previous report of PSA detection using Fe_3O_4. Dynamic ranges were easily tunable for concentration ranges encountered in serum samples by adjusting the Fe_3O_4@GO Concentration. Reagent cost was only $0.85 for a single 2-protein assay.

2.2 Introduction

Accurate, sensitive, cost-effective measurements of multiple proteins in patient samples are critical for progress in clinical detection and monitoring of cancer.[1,2] Recent advances in nanomaterials-assisted assays by ourselves [3] and others [4,5,6,7,8] have improved multiplexed protein sensitivity up to 1000-fold compared to earlier established commercial assays. However, cost and assay complexity still raise barriers to translation of effective protein-based cancer diagnostics into widespread clinical and point-of-care (POC) use.[9]

Enzyme-linked immunosorbent assays [ELISA] have long been the gold standard for clinical protein determinations, and typically achieve detection limits of 1-10 pg/mL for serum proteins.[10] ELISA employs enzyme labels attached to detection antibodies that have been pre-captured on an antibody-decorated well plate to measure proteins using optical detection of a colored enzyme reaction product. Many variations on this "sandwich assay" format, often utilizing magnetic beads, have been used in more modern, multiplexed commercial protein detection kits.[3,11,12] In our recent work, magnetic beads loaded with massive numbers of horseradish peroxidase (HRP) labels and detection antibodies were used to achieve ultrasensitive multiplexed protein detection at levels as low as 5 fg/mL.[13,14]

Iron oxide (Fe_3O_4) nanoparticles have peroxidase-like activity for catalysis of hydrogen peroxide (H_2O_2) reduction, which can be optically monitored by following the H_2O_2–assisted oxidation of 3,3',5,5'-tetramethylbenzidine (TMB) or o-phenylendiamine (OPD).[15,16,17,18] Peroxidase-like activity of Fe_3O_4 nanoparticles for electrochemical detection of hydrogen peroxide has been enhanced by incorporation with other materials like platinum,[19] graphene derivatives,[20,21,22] platinum/palladium,[23] and gold.[24] Chitosan coated Fe_3O_4 nanoparticles were used in colorimetric ELISA to detect of carcinoembryonic antigen with 1 ng/mL LOD[25] and

thrombin with LOD of 1 nM.[26] Dumbbell-like gold-Fe_3O_4 was used for electrochemical detection of prostate specific antigen (PSA) with 5 pg/mL LOD and dynamic range of 0.01-10 ng/mL.[27]

Loading Fe_3O_4 nanoparticles onto graphene oxide (GO) nanosheets improved wettability and dispersion of the composite material.[28],[29] Fe_3O_4 loaded on GO was previously synthesized and utilized for removal of cobalt,[30] hydrocarbons[31] and organic dyes[32] from environmental samples. Electrostatic interactions between negatively charged graphene oxide sheets and Fe_3O_4 nanoparticles coated with positively charged poly(diallydimethylammonium chloride) (PDDA) were used to assemble core-shell Fe3O4@GO particles.[33]

In this paper, we describe the first preparation and use of multiple-Fe_3O_4 nanoparticles assembled onto graphene oxide nanosheets and decorated with antibodies (Ab_2) to first isolate biomarker proteins from the sample under magnetic control, and then electrochemically detect them at ultra-high sensitivity using the intrinsic peroxidase activity. Electrostatic interactions between intact GO sheets and PDDA-coated Fe_3O_4 nanoparticles (NP) provide precise control over the number of Fe_3O_4 NPs per GO sheet, and can be used to optimize the dynamic range of the assay. Here, Ab_2-Fe_3O_4@GO particles were evaluated as substitutes for HRP-Ab_2-magnetic beads (MB) (1 μm diam.) in an 8-sensor microfluidic system featuring off-line capture of PSA and prostate specific membrane antigen (PSMA) on magnetic particles, followed by delivery of these analyte protein-laden particles to an amperometric detection chamber featuring 8-sensors decorated with capture antibodies (Ab_1). Using this approach, we achieved ultrasensitive detection of PSA and SMA simultaneously with tunable dynamic range at low cost compared to HRP-magnetic beads assay.

2.3 Materials and Methods

2.3.1 Synthesis of Fe_3O_4@GO

Fe_3O_4 nanoparticles were synthesized by a solvo-thermal method,[34] Graphene Oxide (GO) was prepared using a modified Hummer's method.[35,36] Briefly, 50 mg of Fe_3O_4 nanoparticles were sonicated 5 min with 10 mL 0.1 mg/mL poly(diallydimethylammonium chloride) (PDDA) in water, magnetically separated, washed 3x with water, and re-suspended in 25 mL water. GO (50 mg) was sonicated in 25 mL water for 30 min after which the dispersion of PDDA-coated Fe_3O_4 nanoparticles was added dropwise with stirring 1 hr.[33] Fe_3O_4@GO composites were then magnetically separated, washed 3x with water, and dried overnight at 55℃ under vacuum. The Fe_3O_4@GO composite was suspended in water at the concentration required for each assay. ELISA kits used were Sigma Aldrich RAB0331 for PS and Lifeome Biolabs/Cusabio EL008782HU-96 for PSMA.

2.3.2. Electrode preparation

Electrochemically reduced graphene oxide (ERGO) was electrophoretically-deposited on the surface of 8-sensor screen-printed carbon arrays (Kanichi Research) from a dispersion of GO (4 mg/mL) in 0.1 M $LiClO_4$ at -1.2 V for 60 s, then further reduced in 0.5 M $LiClO_4$ for 60 s to increase conductivity and surface area. The ERGO-coated sensors were then washed 5X with water and dried under nitrogen.[37] Antibodies were attached to these sensors through both adsorption and amidization after treating with 1-(3-(Dimethylamino)propyl)-3-ethylcarbodiimide hydrochloride (EDC)/N-hydroxysulfosuccinimide (NHSS) to activate ERGO carboxylate groups, then washing with water and incubating overnight with capture antibodies (Ab_1) at 4℃. Arrays were then washed with phosphate buffer (PBS) (pH 7.4) with 0.05% Tween 20 (PBS-T20) and incubated 1 hr with 2% bovine serum albumin (BSA) in phosphate buffer (pH 7.4) to minimize nonspecific binding.

They were then washed again with PBS-T20 and inserted into the detection chamber of a microfluidic immunoarray that was previously described[38] (Fig. 2.1) for protein detection. The detection chamber consists of a PDMS channel between two PMMA plates equipped with symmetrically placed reference Ag/AgCl electrode and counter Pt electrode. The chamber has an outlet and inlet connected to an injector and a syringe pump (Fig. 2.1).

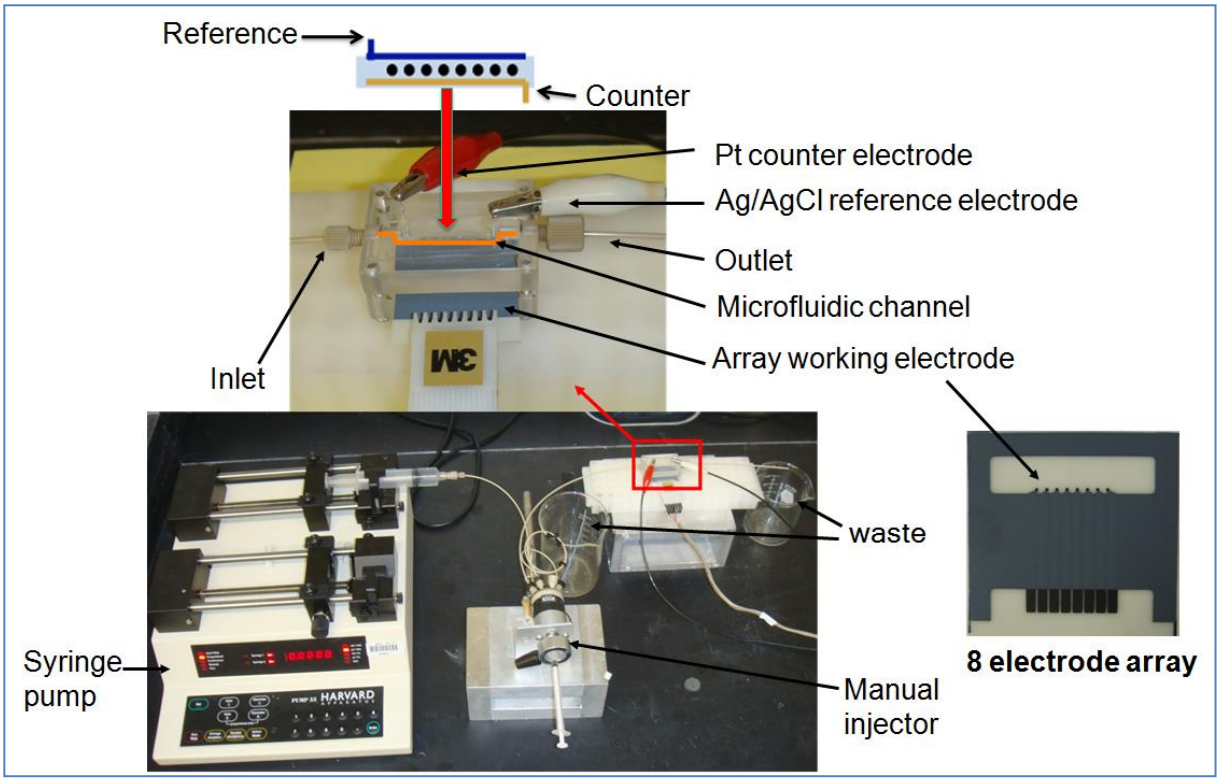

Fig. 2.1 Illustration of microfluidic immunoarray with an injector used to deliver captured protein on Ab_2@Fe_3O_4@GO into a detection chamber equipped with Ag/AgCl reference electrode, Pt counter electrode and housing an 8 electrode ERGO-coated sensor array (Kanichi®) connected to 8 an channel multi-potentiostat (see Malhotra, R. et al., 2012.)

2.3.3. Off-line analyte protein capture

The Fe_3O_4@GO composite was reacted with EDC/NHSS by stirring for 10 min to activate carboxylic groups on the GO, then reacted with antibodies (Ab_2) by incubation overnight at 4℃ to form Ab_2@Fe_3O_4@GO conjugates. Ab_2@Fe_3O_4@GO conjugates were magnetically separated,

washed 2x with 0.1% BSA, then incubated for 1 hr with 0.1 % BSA to minimize nonspecific binding. Protein biomarkers (antigen, Ag) were captured from samples by mixing with $Ab_2@Fe_3O_4@GO$ conjugates while stirring for 30 min.[38] $Ab_2@Fe_3O_4@GO$ with captured analyte proteins were then magnetically separated, washed with 0.1% BSA and dispersed in 120 µL 0.1% BSA. These $Ab_2@Fe_3O_4@GO$-protein conjugates were delivered to the detection chamber through an injector equipped with a 100 µL sample loop. Once the particles filled the reaction chamber as monitored by the black color of the conjugates, the flow was stopped and the array was incubated for 30 min. to enable $Ab_2@Fe_3O_4@GO$-protein capture on the Ab_1-decorated sensors. Then, sensors were washed with PBS-T20 for 4 min at 100 µL/min to remove unbound species (Scheme 2.1).

2.3.4. Protein Measurements

Amperometric signals were generated by injecting 100 µL of 5 mM H_2O_2 in PBS at a flow rate of 100 µL/min and applying -0.3 V vs. Ag/AgCl (0.14 M NaCl). Amounts of $Fe_3O_4@GO$ on the sensors depend on concentrations of captured biomarker proteins. To mimic human serum, undiluted calf serum was used to prepare protein standards.

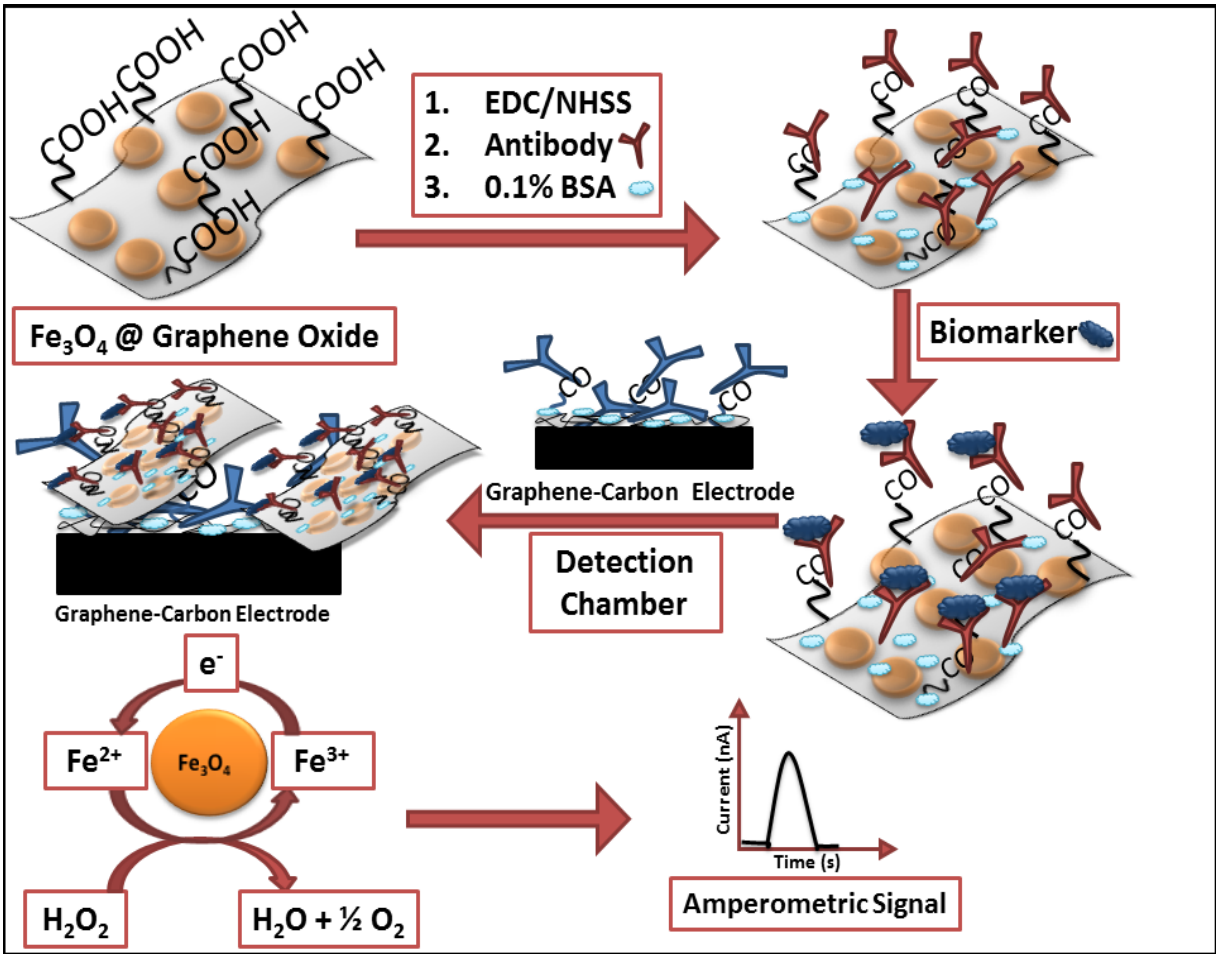

Scheme 2.1 Protein capture and detection mediated by Fe_3O_4@GO sheets. Proteins captured by Fe_3O_4@GO decorated with detection antibodies. Composite with biomarker was then captured on the sensor surfaces coated with graphene and capture antibodies. Amperometric signal was generated by injecting 100 µL 5 mM H_2O_2

2.4. Results and Discussion

2.4.1. Characterization of Fe_3O_4@GO

Dynamic light scattering (DLS) and scanning electron microscopy (SEM) images of Fe_3O_4 nanoparticles revealed average diameters of 300 (±15) nm (Fig. 2.2 A,B). Zeta potential measurements showed that Fe_3O_4 nanoparticles had surface charge -11 (±4) mV. The surface

charge changed to +65 (±6) mV after coating Fe_3O_4 nanoparticles with polycationic PDDA. GO sheets exhibited an average size of 900 (±40) nm and surface charge of -79 ±7 mV. The negative surface charge of GO is due to oxygen-containing surface groups, e.g. carboxylate, epoxy, and hydroxyl.[39]

When positively charged PDDA-coated Fe_3O_4 nanoparticles were mixed with negatively charged GO sheets, a composite of Fe_3O_4 nanoparticles bound to the surface of GO sheets (Fe_3O_4@GO) formed through electrostatic interactions with a final surface charge of -42 (±3). The Fe_3O_4@GO composite was readily dispersed in aqueous solution and then separated in 30 s using a magnet to isolate the particles (Fig. 2.2 E). The Fe_3O_4@GO composites had irregular shapes with an average size dimension of ~1.0 μm as seen in SEM images (Fig. 2.2 C,D,F).

Peroxidase-like activity of Fe_3O_4@GO for hydrogen peroxide reduction was demonstrated by measuring the rate of oxidation of 2,2′-Azino-bis(3-ethylbenzothiazoline-6-sulfonic acid) diammonium salt (ABTS).[40] In this standard assay the change in absorbance at 592 nm corresponds to the catalytic oxidation of ABTS in the presence of H_2O_2 to a colored product. Measured catalytic activity was 260 units per mg Fe_3O_4@GO, equivalent to catalytic activity of 0.312 mg of pure HRP enzyme.

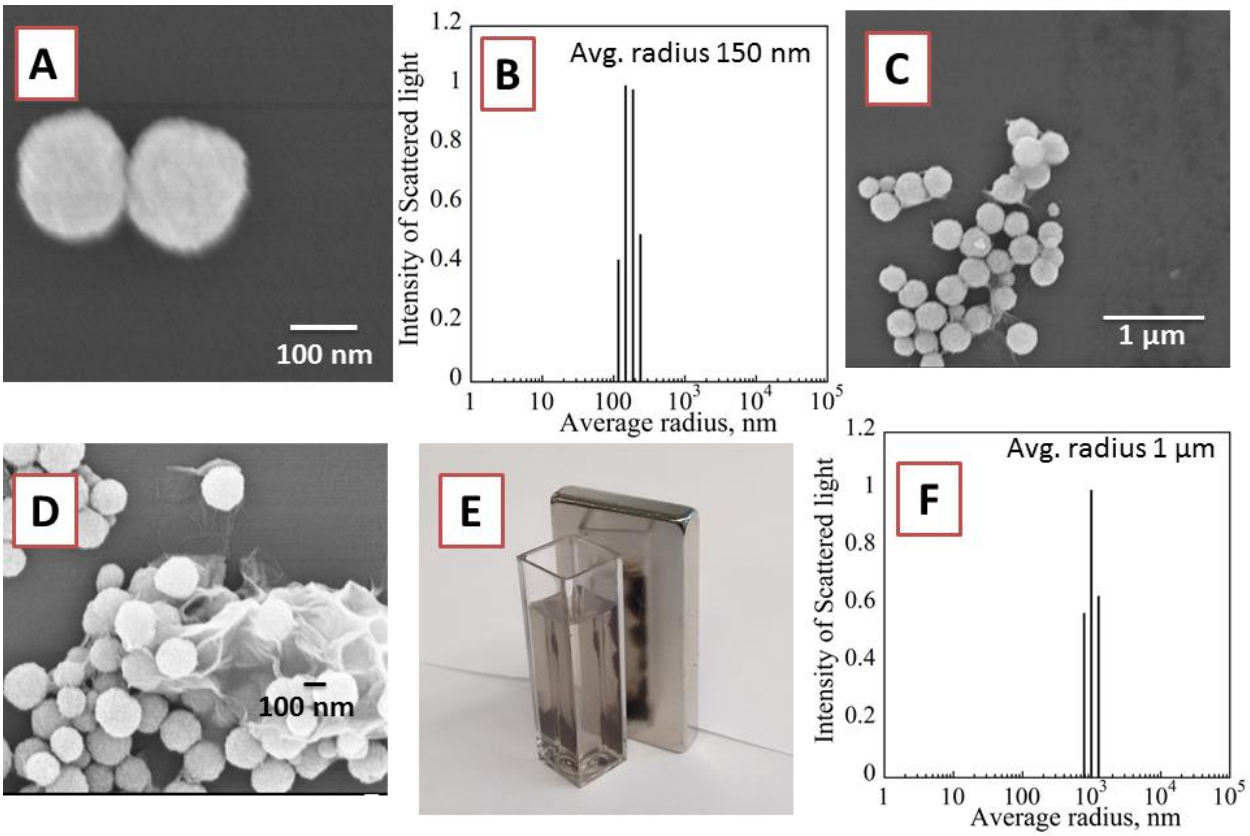

Fig. 2.2 Morphology of Fe_3O_4 nanoparticles: (A) SEM image showing two Fe_3O_4 nanoparticles and (B) DLS of Fe_3O_4 nanoparticles with average diameter 300 nm. (C & D) SEM Images of Fe_3O_4 on surface of GO sheets showing morphology of Fe_3O_4@GO, (E) Magnetic attraction of Fe_3O_4@GO nanoparticles in the cuvette to the magnet on the right (F) DLS of Fe_3O_4@GO composite

For voltammetry, the negatively charged Fe_3O_4@GO composites, (0.1 mg/mL) were attached to screen-printed carbon electrodes in the array through alternating electrostatic layer-by-layer (LBL) assembly using aqueous 2 mg/mL PDDA solution as the alternate-layer polycation. After washing, cyclic and square wave voltammograms (CV, SWV) of PDDA/Fe_3O_4@GO electrodes in 0.1 M PBS buffer showed a large increase in peak current when the concentration of H_2O_2 was increased compared to a bare electrode (Fig. 2.3). Catalytic peak current of the Fe_3O_4@GO electrode gave a good linear correlation with increasing H_2O_2 concentration for CV and SWV peak

currents (Fig. 2.3). These results confirmed the high catalytic activity of Fe_3O_4@GO for the reduction of H_2O_2, and the ability of this material to serve as a label in electrochemical detection.

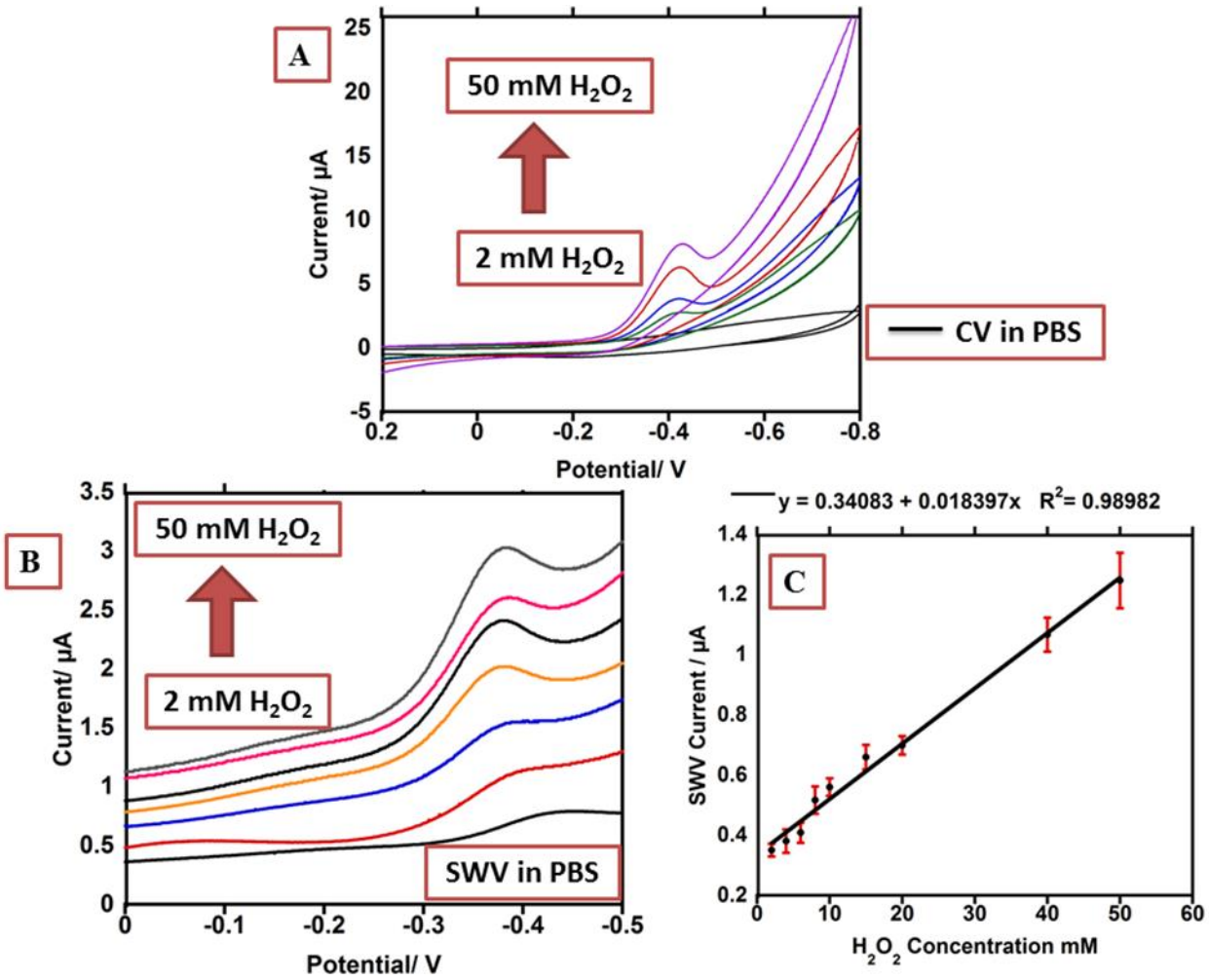

Fig.2.3 Catalytic reduction of H_2O_2 by Fe_3O_4@GO on Kanichi® screen printed carbon array electrodes: (A) CV of Fe_3O_4@GO coated electrode in absence and presence of increasing concentrations (2-50 mM) of H_2O_2 in 0.1 M phosphate buffer (pH 7.4) against Ag/AgCl (0.14M NaCl) at 100 mV/s, (B) square wave voltammograms (SWV) at 5 Hz of Fe_3O_4@GO coated electrode in absence and presence of increasing concentrations (2-50 mM) of H_2O_2 in 0.1 M phosphate buffer (pH 7.4), and (C) plots of peak current of SWV against increasing concentration of H_2O_2 in 0.1 M phosphate buffer (pH 7.4), n=8 (control subtracted)

A bicinchoninic acid (BCA) total protein assay was used estimate the amount of antibodies loaded on Fe_3O_4@GO (Noble and Bailey, 2009).[41] Loading capacity was found to be 1.52 µg of proteins per 1 mg Fe_3O_4@GO which represents around $2.25x10^{12}$ antibodies /mg Fe_3O_4@GO (Fig 2.4).

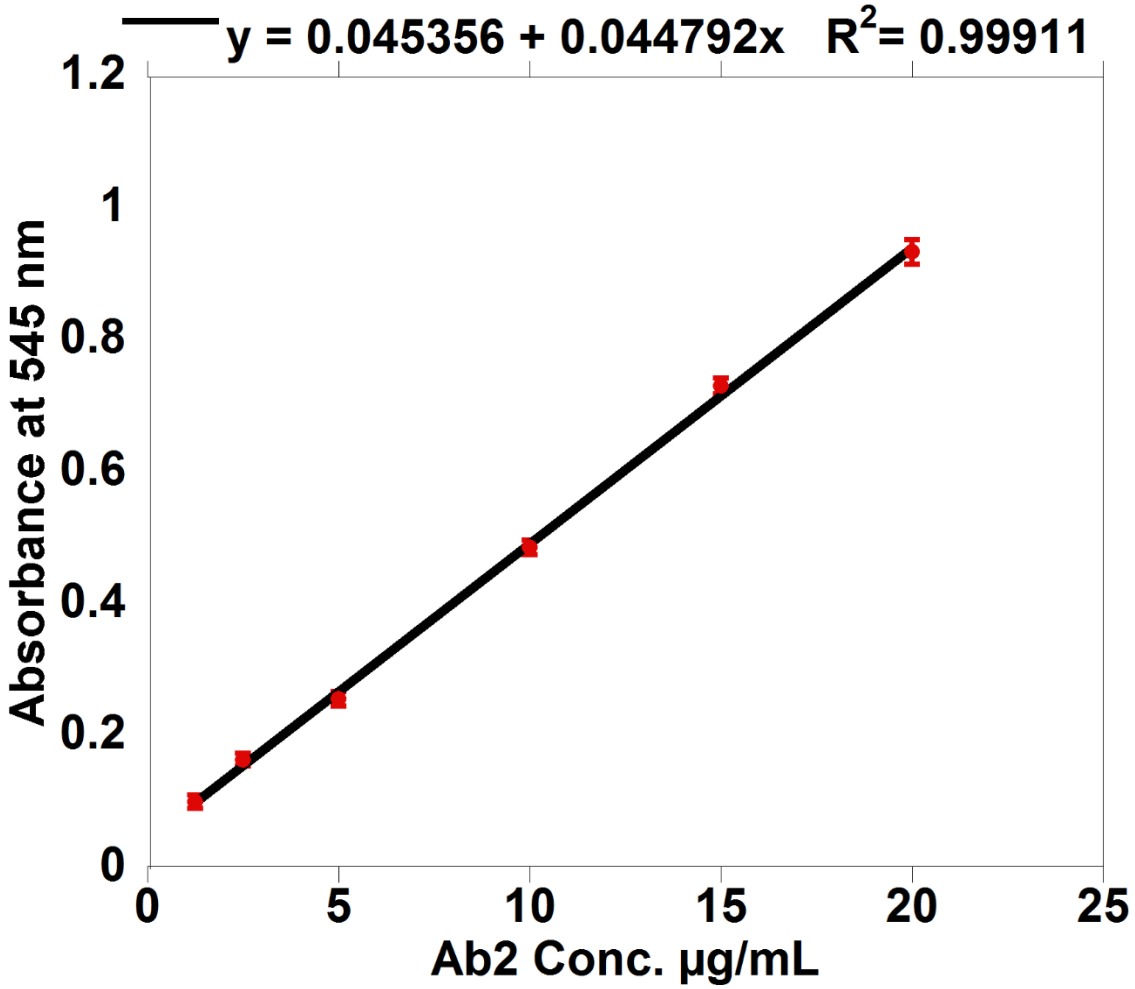

Fig. 2.4 Standard Calibration curve for measurement of series of concentrations of standard PSA detection antibody (Ab_2) using BCA protein detection kit at 545 nm.

Electrical conductivity of the Fe_3O_4@GO as well as GO and Fe_3O_4 films were measured using the standard four-probe method.[42] Conductivities were 52 (±11) S/cm for GO, $4.0X10^{-3}$ ($\pm 7.0X10^{-4}$) S/cm for Fe_3O_4 films, and 17 (±2) S/cm for Fe_3O_4@GO.

2.4.2. Sensor Characterization

Array sensor surface areas before and after coating with ERGO were estimated by CV using the Randles-Sevcik equation[43] with 1 mM ruthenium hexamine chloride as a redox probe in 0.1 M KCl. Surface area of the screen-printed carbon electrode was 9.7±0.1 x10^{-4} cm^2 and increased to 2.0±0.1 x10^{-3} cm^2 after depositing ERGO (Fig. 2.5).

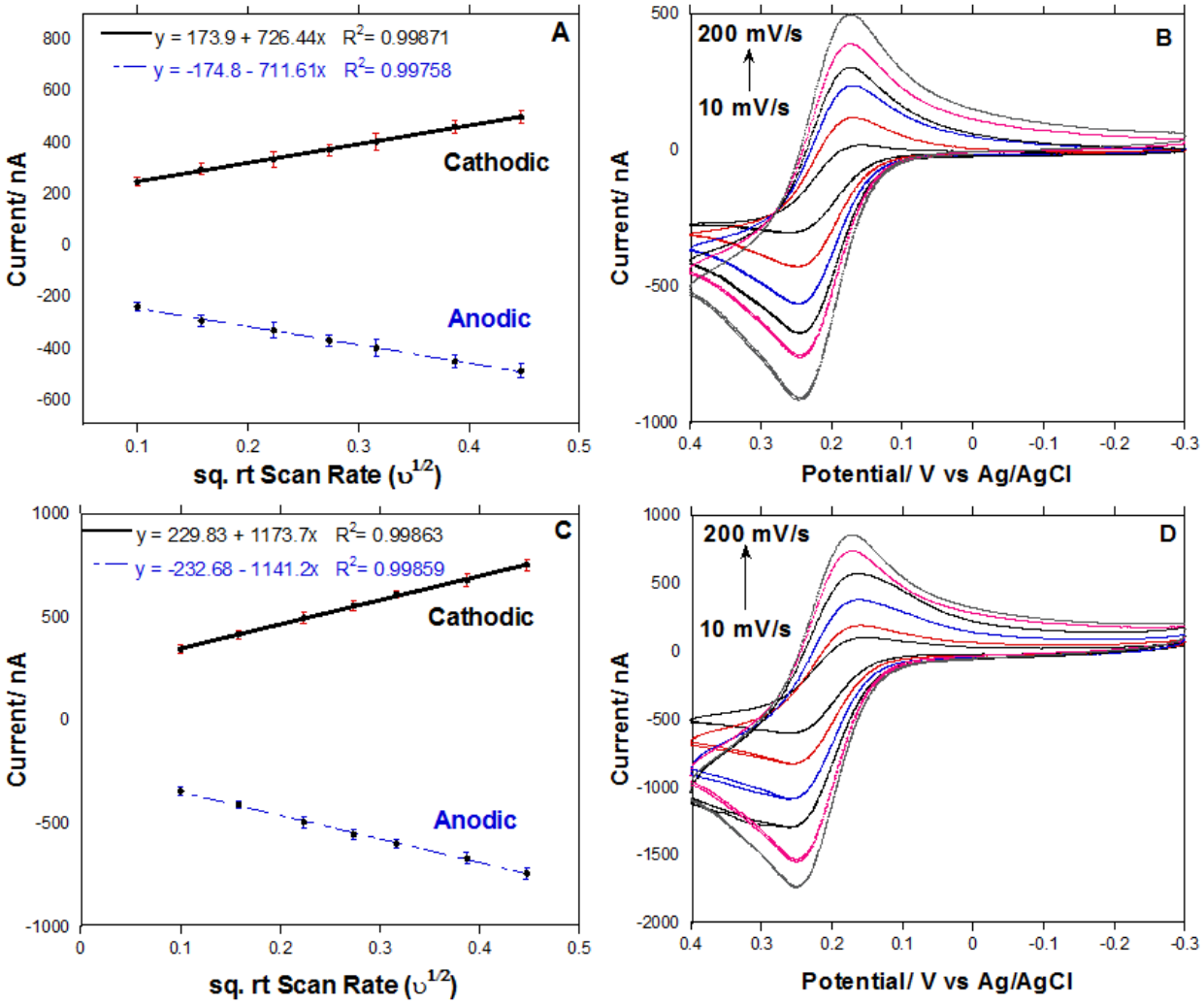

Fig. 2.5 Cyclic voltammetry characterization of bare and ERGO coated sensor array using 0.5 mM Fc-MeOH in 0.1 M TEAP vs Ag/AgCl (0.14M NaCl) showing (A) Plot of peak current vs. square root of the scan rate for the bare electrode, (B) Cyclic voltammograms at different scan rates (from 10 to 200 mV/s) for bare electrode, (C) Peak current plot for ERGO coated electrode, (D) Cyclic voltammograms at different scan rates (from 10 to 200 mV/s) for ERGO coated electrode.

The increase in electrochemical active surface area is due to the increased roughness of the surface after deposition of ERGO (Fig. 2.6).

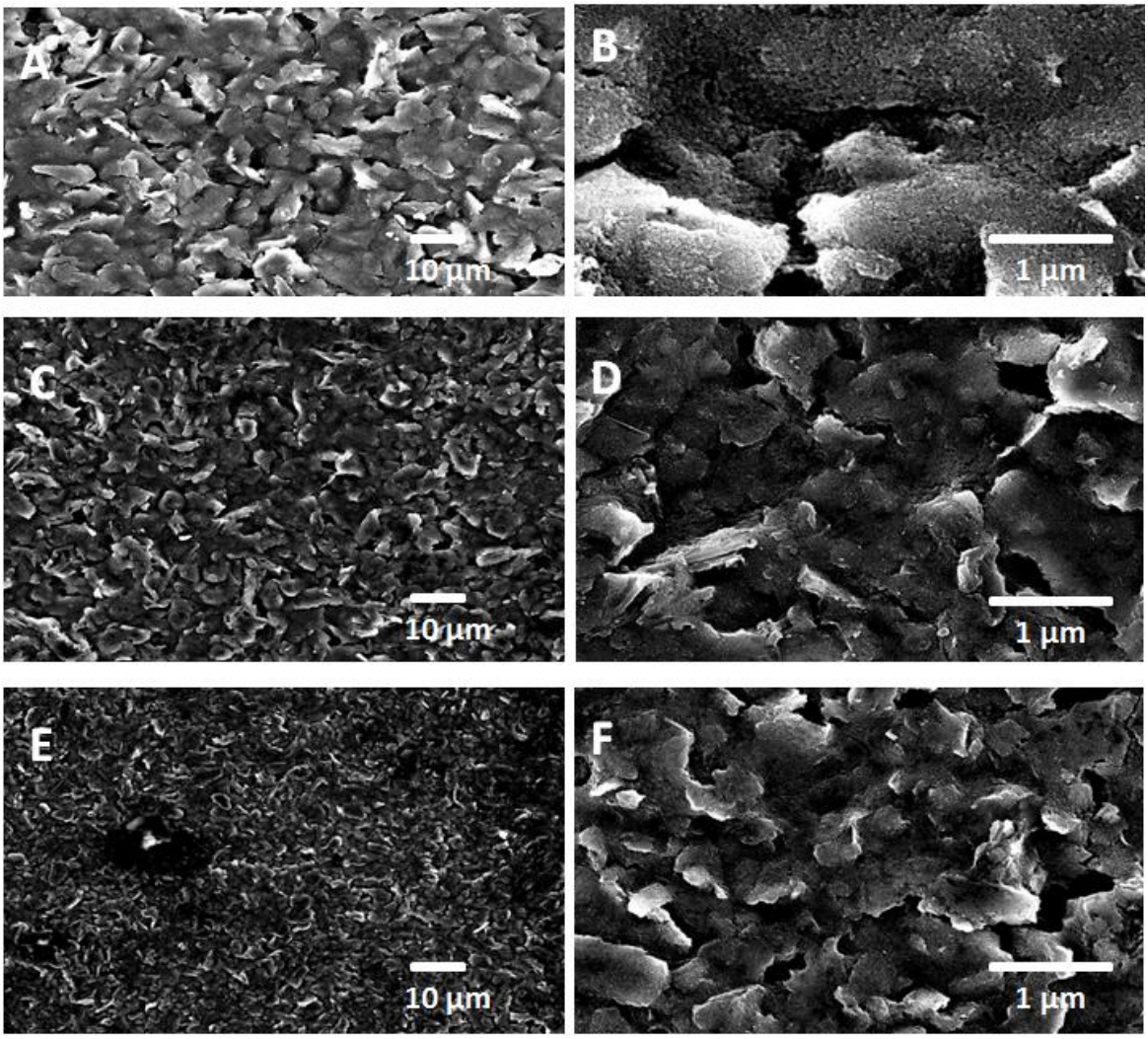

Fig. 2.6 Morphology of the Kanichi® carbon electrodes: (A), (B) SEM images of bare electrode, (C), (D) SEM images of electrode after first reduction cycle in 4 mg/mL GO/0.1 M $LiClO_4$ at -1.2V vs Ag/AgCl (0.14 M NaCl) reference electrode, and (E),(F) SEM images of electrode after second reduction cycle in 4 mg/mL GO/0.5 M $LiClO_4$ at -1.2V vs. Ag/AgCl (0.14 M NaCl) reference electrode

2.4.3. Optimization

Analytes chosen to demonstrate system performance (PSA and PMSA) in serum are overexpressed in prostate cancers. PSA is an intercellular glycoprotein (34 kDa kallikrein-like protease) that is locally synthesized in prostatic tissue.[44] PSA levels higher than 4 ng/mL or rising levels with time are indicatives of prostate cancer.[45] PSMA is a cell-surface glycoprotein with average plasma levels in males above 50 at 360 ng/mL and 275 ng/mL in males younger than 50.[46] Plasma levels can increase above 600 ng/mL in prostate cancer patients.[47]

The system in Figure 1 was optimized to measure the analyte proteins with specific capture antibodies attached onto the sensors. The analyte proteins were first captured by detection antibodies (Ab_2) immobilized on Fe_3O_4@GO in a test tube and magnetically separated. Then the protein-Ab_2-Fe_3O_4@GO bio-conjugate was delivered to the detection chamber (See Experimental). The protein-Ab_2-Fe_3O_4@GO conjugates were captured by Ab_1 on sensor surfaces under stopped flow, and unbound conjugates were then washed away. Amounts of Fe_3O_4@GO bound to the sensor were proportional to the specific protein concentrations, as was the amperometric peak current due to the decomposition of H_2O_2 catalyzed by Fe_3O_4 nanoparticles in the detection step.

Concentrations of Ab_1 on sensors and Ab_2 on Fe_3O_4@GO were optimized first in order to achieve the largest signal to noise ratio for PSA and PSMA proteins in undiluted calf serum. To optimize Ab_1, other experimental parameters including Ab_2 concentration were kept constant while varying Ab_1 concentration. Similar procedures were used to optimize Ab_2 concentration while keeping Ab_1 constant. Optimal Ab_1 concentrations in the sensor reaction mixture were 100 µg/mL for both PSA and PSMA, while the optimal Ab_2 concentration was 20 µg/mL for PSA and 25 µg/mL for PSMA (Fig. 2.7).

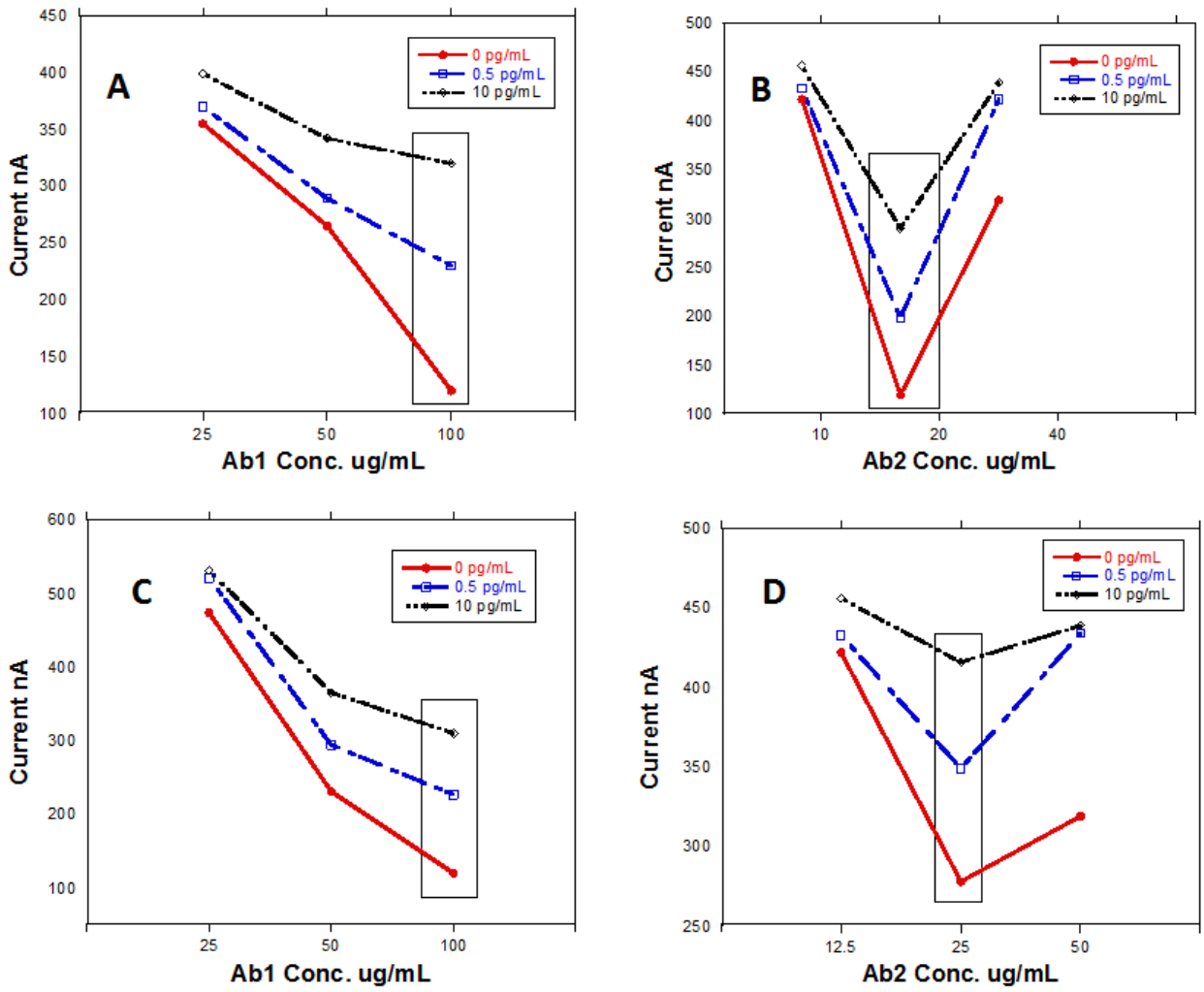

Fig. 2.7 Optimization of capture antibodies (Ab1) Concentrations on the sensor array for (A) PSA and (C) PSMA. Optimization of detection antibodies (Ab2) concentrations loaded om magnetic beads for (B) PSA and (D) PSMA. Signals were generated by injecting 5 mM H_2O_2 in 0.1 M PBS buffer at –0.3 V against Ag/AgCl (0.14 M NaCl)

2.4.4. Detection of PSA and PSMA

Optimized Ab_1 and Ab_2 concentrations were used to detect single biomarker proteins utilizing different concentrations of the Fe_3O_4@GO to tune the dynamic range and limits of detection (LOD, as 3X SD above blank) of the assay. For the most sensitive PSA assay, we used a high concentration of Fe_3O_4@GO (2 mg/mL) to get a linear correlation with 0.0361

nA/(log(pg/mL)sensitivity, LOD 15 fg/mL and dynamic range of 61 fg/mL to 3.9 pg/mL. To achieve a higher concentration dynamic range, we used a lower concentration of Fe_3O_4@GO (0.5mg/mL) to get 105 nA/(log(pg/mL) sensitivity with a LOD 4.9 pg/mL and dynamic range of 9.8 pg/mL to 624 pg/mL (Fig.2.8).

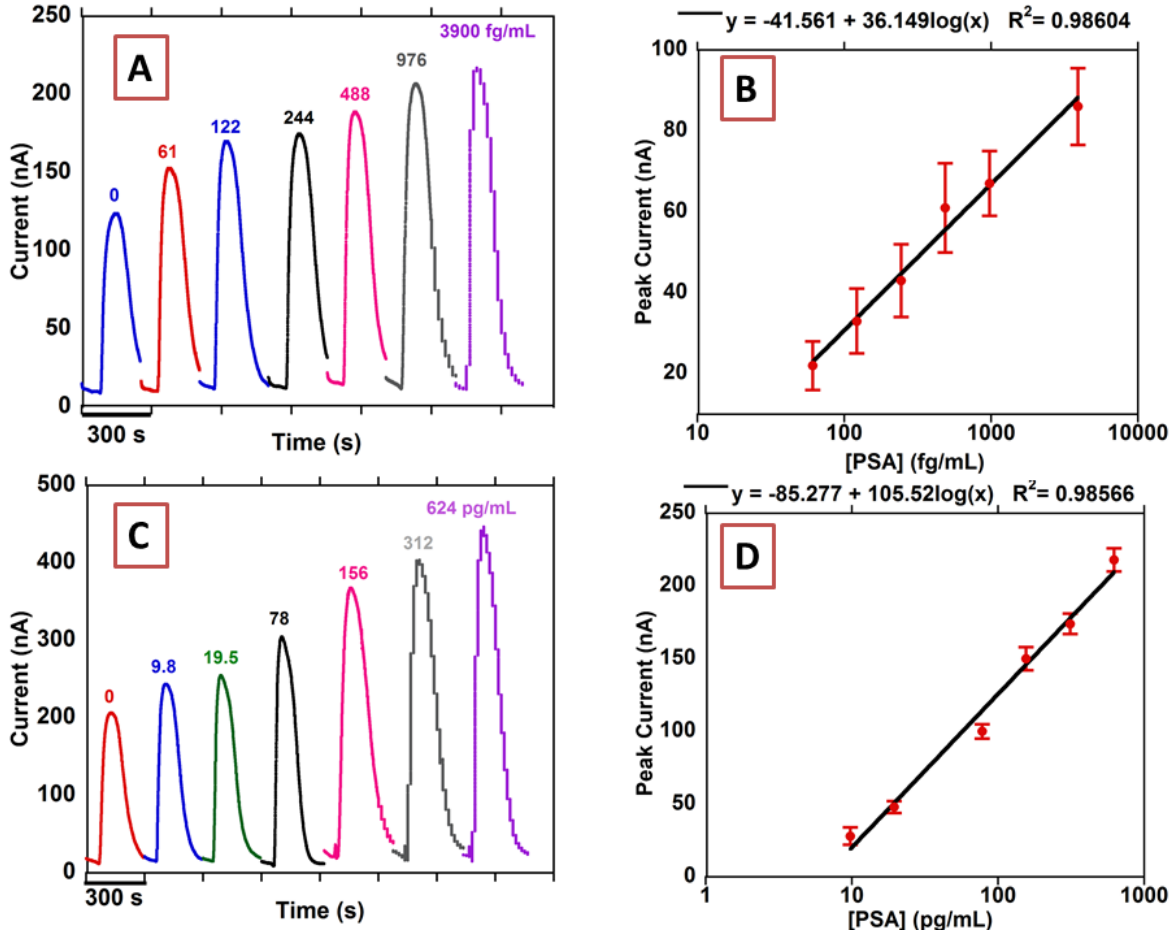

Fig. 2.8 Results from n=8. microfluidic array for standard solutions of PSA in calf serum (A) peak currents using 2 mg/mL Fe_3O_4@GO and (B) calibration plot (control subtracted) using 2 mg/mL Fe_3O_4@GO, n=8 (C) peak currents using 0.5 mg/mL Fe_3O_4@GO and (D) calibration plot (control subtracted) using 0.5 mg/mL Fe_3O_4@GO , n=8. Signals at -0.3 V vs Ag/AgCl (0.14 M NaCl) after injecting 100 µL 5 mM H_2O_2

For PSMA, using a 2 mg/mL concentration of Fe_3O_4@GO, LOD was 4.8 fg/mL with 0.0611 nA/(log(pg/mL) sensitivity and dynamic range was 9.8 fg/mL to 10 pg/mL. With 0.5 mg/mL Fe_3O_4@GO, and LOD 15.6 pg/mL , the dynamic range was 15.6 pg/mL to 7.8 ng/mL with 25.9 nA/(log(pg/mL) sensitivity (Fig. 2.9).

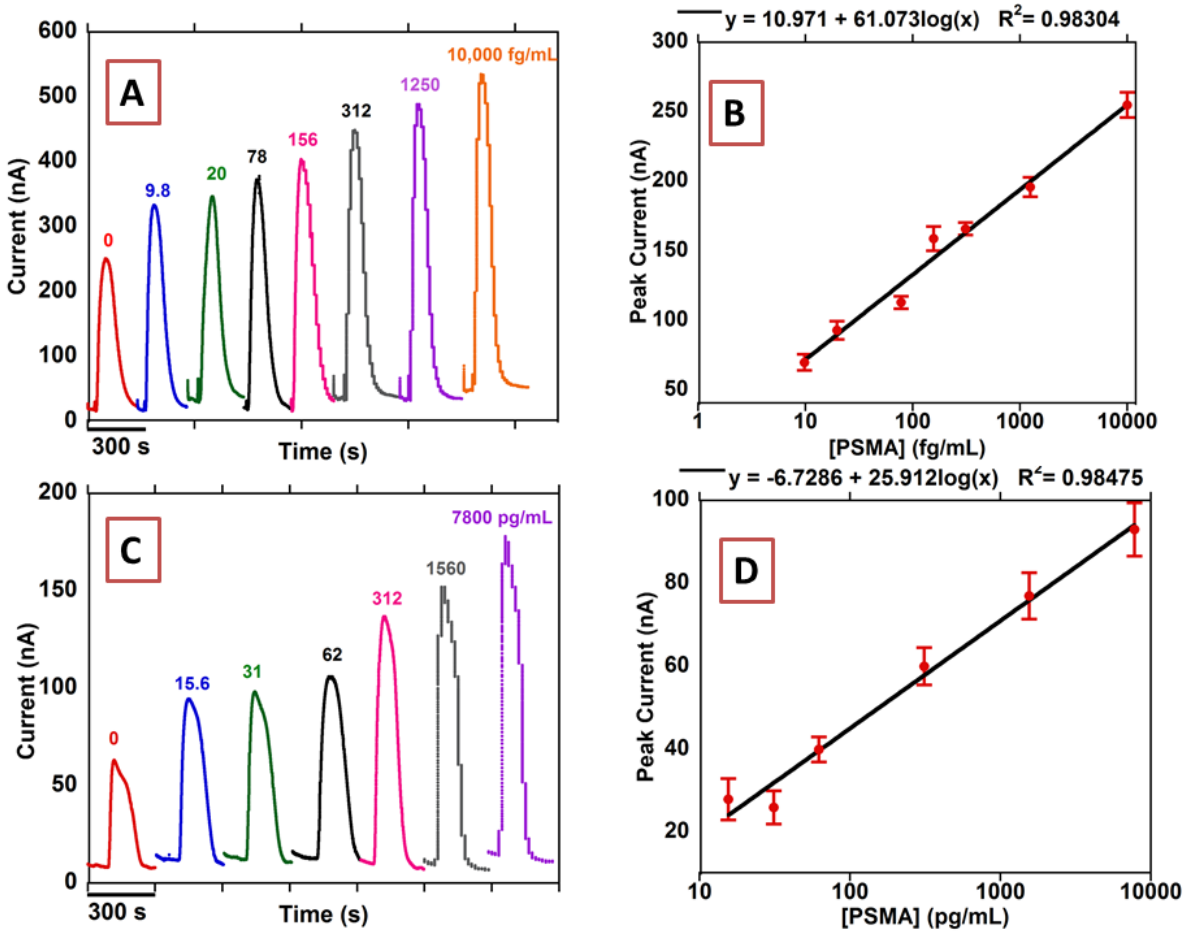

Fig. 2.9 Amperometric responses in the microfluidic immunoarray for (A) standard PMSA in undiluted calf serum and (B) calibration plot using 2 mg/mL Fe_3O_4@GO, control subtracted, n=8 (C) Amperometric responses for individual standard solutions of PMSA in undiluted calf serum and (D) calibration plot using 0.5 mg/mL Fe_3O_4@GO, control subtracted, n=8. Signals developed by injecting 100 µL 5 mM H_2O_2 detected at -0.3 V vs Ag/AgCl (0.14 M NaCl).

Serum levels for PSA in prostate cancer patients is >4 ng/mL and that for PSMA is >300 ng/mL.[45,47] Concentrations of Fe_3O_4@GO were tuned for multiplexing both biomarkers on the same sensor array to avoid excessive dilution of patient samples. To prepare Ab_2-Fe_3O_4@GO bio-

conjugates, 0.5 mg/mL Fe_3O_4@GO was used to label PSMA Ab_2 while 1.0 mg/mL Fe_3O_4@GO was used to label PSA Ab_2. Using this protocol, the PSA was tuned to LOD 1.25 pg/mL with a dynamic range of 1.25 to 1000 pg/mL while PSMA was tuned to LOD 9.7 pg/mL with a dynamic range of 9.7 to 5000 pg/mL (Fig. 2.10). This approach allowed dilution of patient serum by 100-fold in buffer to bring concentrations into dynamic ranges.

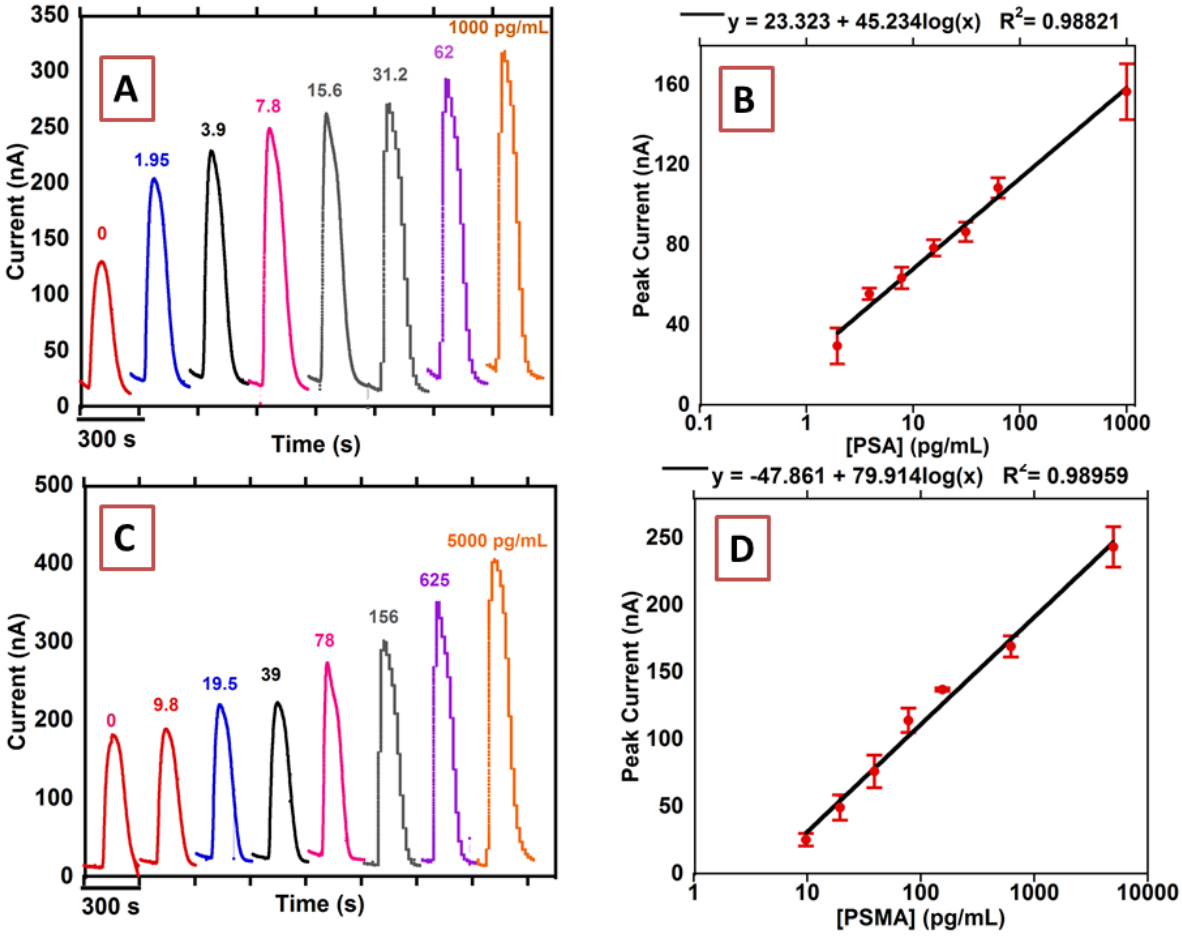

Fig. 2.10 Amperometric responses from microfluidic immunoarray in mixtures: (A) PSA and (C) PSMA. Along with multiplexed calibrations of: (B) PSA and (D) PSMA in calf serum using 1 mg/mL Fe_3O_4@GO after injecting 5 mM H_2O_2 at -0.3 V vs. Ag/AgCl(0.14 M NaCl), Controls subtracted, n=8

2.4.5. Assay validation

PSA and PSMA were determined in 3 pooled prostate cancer patient serum samples and one negative control human sample (Capital Bioscience Inc.) and compared to single protein ELISA assays. 10 µL of each sample was diluted 100x in PBS. Samples were also spiked with varying concentrations (100-500 ng/mL) of PSMA as an additional accuracy test, since initial analyses showed very low concentrations of this protein (less than 20 ng/mL). Immunoarray results showed very good correlation with the results obtained from single protein ELISA (Fig. 2.11). Linear correlation plots of the immunoassay against ELISA showed slopes near unity, 1.118±0.042 for PSA and 1.025±0.019 for PSMA, and intercepts close to zero, -0.611±0.319 for PSA and 2.0±6.6 for PSMA (Fig. 2.11).

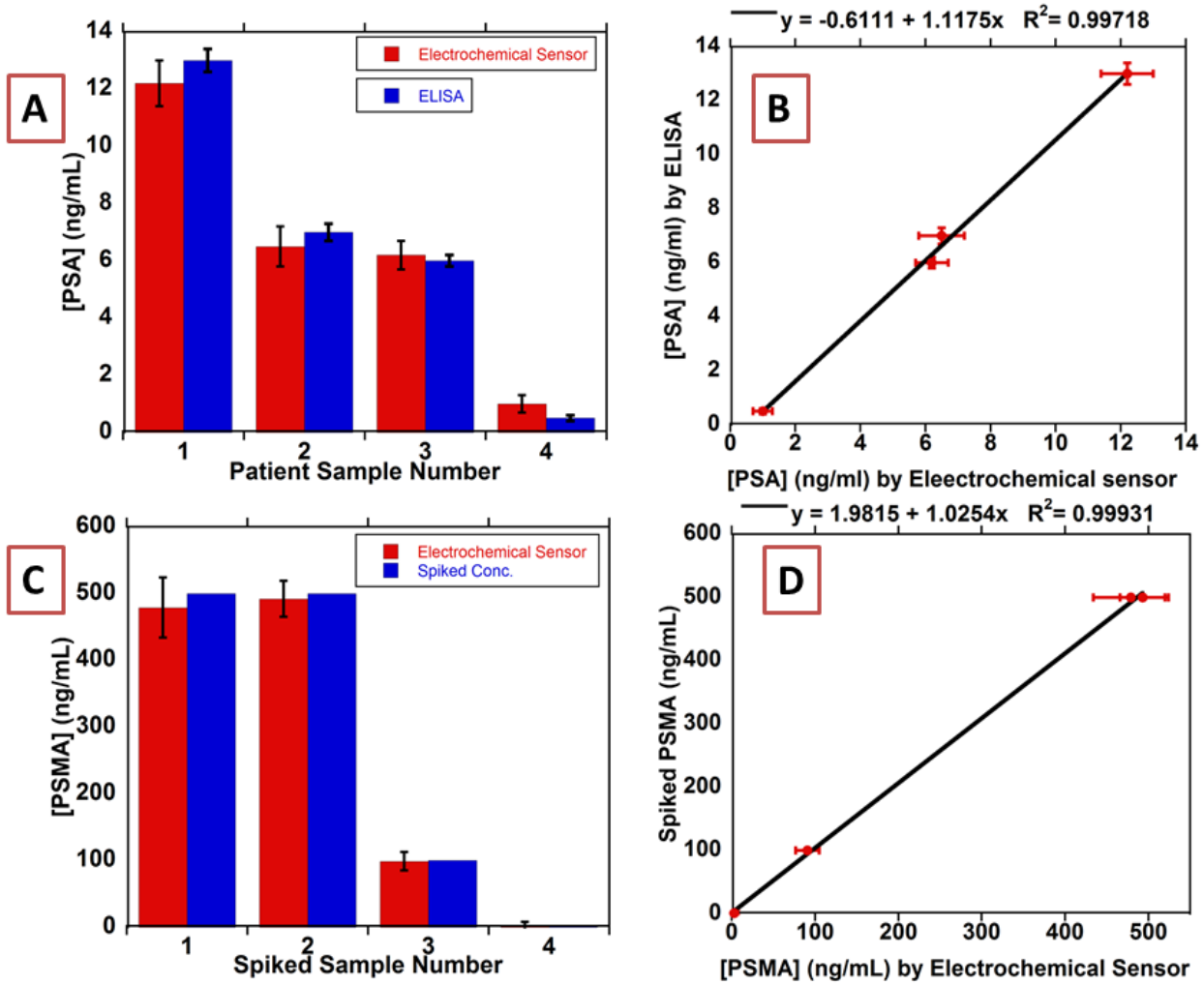

Fig. 2.11 Multiplexed immunoarray compared to single-protein ELISA results for patient samples for (A) PSA and (B) PSMA and linear correlation plots of immunoarray against ELISA for (C) PSA and (D) PSMA

The above results demonstrated the use of Fe_3O_4 nanoparticles on graphene oxide sheets (Fig. 2.2) decorated with antibodies to facilitate both analyte protein capture and electrochemical detection (Scheme 2.1) in a simple microfluidic device for sensitive measurements of proteins. Prostate cancer biomarker proteins PSA and PSMA were detected in diluted serum with LODs in the low fg/mL range and with very high sensitivity. Attachment of multiple Fe_3O_4 nanoparticles on each

GO sheet provides a huge amplification of the amperometric signal per protein. The GO sheets also allow attachment of a large number of detection antibodies leading very efficient protein capture, analogous to other multi-antibody particles.[48] In addition to previous advantages of using GO sheets, we believe micrometer-sized GO sheets facilitated the transfer of electrons from electrode surface to nanoparticles which further improve their catalytic properties. This approach provided sensitivity roughly equivalent to that obtained using 1 μm diam. magnetic beads coated with massive numbers of Ab_2 and HRP labels.[13,38] This LOD is 1000-fold better than the only previous report of using Fe_3O_4 (as gold-Fe_3O_4) as an electrochemical label for detection of PSA.[27]

Excellent reproducibility was obtained as evidenced by the small error bars in multiple measurements (Figures 2.8, 2.9 and 2.10). The Fe_3O_4@GO conjugates provide a low-cost material stabilized by virtue of multiple co-operative binding events on the GO sheets. In addition to catalytic activity of Fe_3O_4 nanoparticles providing the detection approach, they also provide magnetic control that facilitates separation and washing. Electrodes decorated with capture antibodies were stable for 3 days at 4℃ after which 20% of the activity were lost on day 4 (Fig. 2.12).

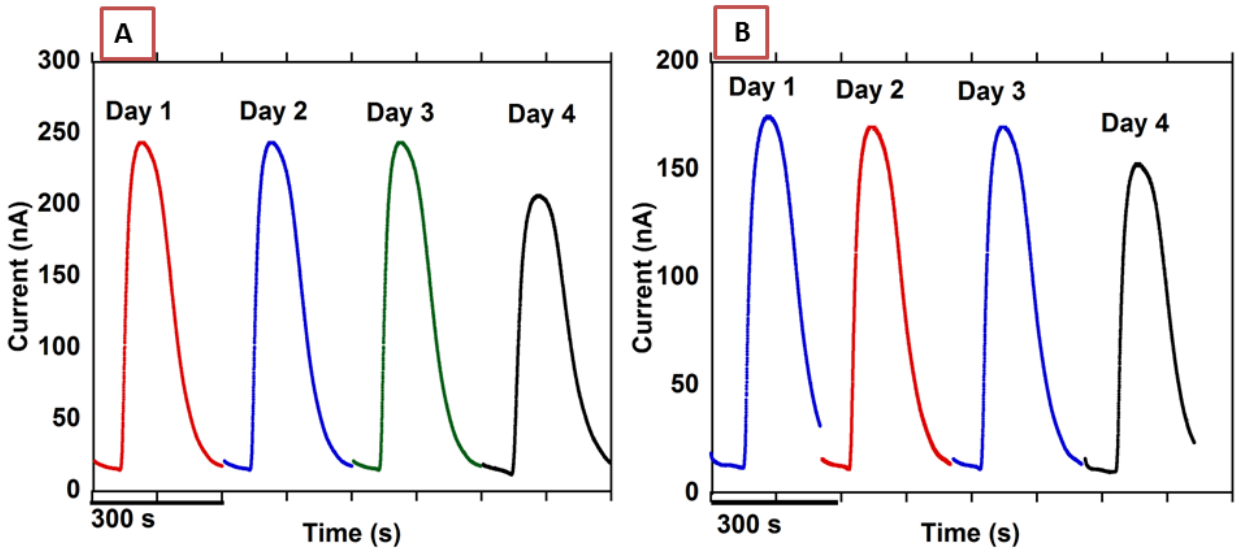

Fig. 2.12 Amperometric responses in the microfluidic immunoarray for (A) standard 20 pg/mL PSA in undiluted calf serum in 4 successive days, (B) standard 7ng /mL PSMA in undiluted calf serum in 4 successive days

Sensitivities as given by the slopes of the calibration curves (Fig. 2.8 and Fig. 2.9) and LODs in calf serum can be easily tuned in this system by adjusting the amounts of Fe_3O_4@GO composite used in the assay. For PSA, sensitivity can be tuned from 0.036 nA/log (pg/mL) to 10.5 nA/log (pg/mL) and from 0.061 nA/log (pg/mL) to 25.9 nA/log (pg/mL) for PSMA. In contrast, other assay done using the same offline protein capture technique in a similar microfluidic device utilizing magnetic beads labeled with 400,000 HRP had a sensitivity of 5.9 to 6.8 nA/log (pg/mL).[38] LOD was 15 fg/mL for PSA and 4.8 fg/mL for PSMA which is comparable to those obtained in other multiplexed protein assays using commercial magnetic beads labeled with multiple HRPs and Ab_2. [13,14] Tuning of these enzyme-label assays can be done by changing the number of HRPs on the beads and/or by changing bead size, but both approaches require new syntheses of the HRP-Ab_2-coated magnetic beads. Maintaining the ultra-low LODs, the cost of

reagents for 2-protein assays using Fe_3O_4@GO was $0.85, only 30% of the cost of the same assay with commercial magnetic beads and HRP which cost around $3.00 / 2-protein assays.[14]

Multiplexing is important in protein-based cancer diagnostics to lower incidence false positives and false negatives encountered with less reliable single protein biomarker-based assays.[3] Multiplexed protein detection is easily optimized in the present assay system by tuning the dynamic range of the assay for each protein concentration level expected in the particular samples at hand by adjusting the amount of Fe_3O_4@GO used to prepare Ab_2-Fe_3O_4@GO for each protein (Figure 4). Tuning the dynamic ranges allowed simultaneous detection of two protein biomarkers in the same assay here, in which the serum level of PSMA can be up to 80-fold larger than that of PSA (Fig. 2.11).

Coating the screen-printed carbon sensor electrodes with electrochemically reduced GO facilitated immobilization of a large number of capture antibodies and also improves the conductivity of the electrode surface. While GO is a semiconductor with 52 (±11) S/cm conductivity, incorporation of Fe_3O_4 onto the surface did not impair semi-conductive character of the Fe_3O_4@GO composite that had a conductivity of 17 (±2) S/cm.[49]

The assay gave excellent accuracy as shown by the good correlation to single protein ELISA with slopes of unity and near zero intercepts (Fig. 2.11). Sample required was only 10 µL diluted 100 times to fit into the dynamic range of the multiplexed assay that was enough for three or more runs. Ability to detect PSA and PSMA in human serum samples that contain hundreds of other proteins demonstrated the high selectivity of the assay.

2.5. Conclusion

An ultrasensitive, tunable mediator-free, enzyme-free immunoarray protocol using magnetic Fe_3O_4@GO composites was demonstrated for the detection of two prostate cancer biomarkers. Fe_3O_4@GO composites serve the dual function of magnetic analyte isolation and labels for

detection. Ease of tunability allowed easy tailoring of protocols to simultaneously detect PSMA at levels up to 80-fold more concentrated than PSA in patient samples. Accuracy was demonstrated by excellent correlation of patient serum sample immunoarray results with ELISA.

2.6. References

[1] Kulasingam, V.; Diamandis, E. P. Strategies for Discovering Novel Cancer Biomarkers through Utilization of Emerging Technologies. *Nat. Clin. Pract. Oncol.* **2008**, *5* (10), 588–599.

[2] de Gramont, A.; Watson, S.; Ellis, L. M.; Rodón, J.; Tabernero, J.; de Gramont, A.; Hamilton, S. R. Pragmatic Issues in Biomarker Evaluation for Targeted Therapies in Cancer. *Nat. Rev. Clin. Oncol.* **2015**, *12* (4), 197–212.

[3] Rusling, J. F.; Bishop, G. W.; Doan, N.; Papadimitrakopoulos, F. Nanomaterials and Biomaterials in Electrochemical Arrays for Protein Detection. *J. Mater. Chem. B Mater. Biol. Med.* **2014**, *2* (1).

[4] Zhang, Y.; Guo, Y.; Xianyu, Y.; Chen, W.; Zhao, Y.; Jiang, X. Nanomaterials for Ultrasensitive Protein Detection. *Adv. Mater. Deerfield Beach Fla* **2013**, *25* (28), 3802–3819.

[5] Meissner, E. G.; Decalf, J.; Casrouge, A.; Masur, H.; Kottilil, S.; Albert, M. L.; Duffy, D. Dynamic Changes of Post-Translationally Modified Forms of CXCL10 and Soluble DPP4 in HCV Subjects Receiving Interferon-Free Therapy. *PLOS ONE* **2015**, *10* (7), e0133236.

[6] Kelley, S. O.; Mirkin, C. A.; Walt, D. R.; Ismagilov, R. F.; Toner, M.; Sargent, E. H. Advancing the Speed, Sensitivity and Accuracy of Biomolecular Detection Using Multi-Length-Scale Engineering. *Nat. Nanotechnol.* **2014**, *9* (12), 969–980.

[7] Das, J.; Kelley, S. O. Protein Detection Using Arrayed Microsensor Chips: Tuning Sensor Footprint to Achieve Ultrasensitive Readout of CA-125 in Serum and Whole Blood. *Anal. Chem.* **2011**, *83* (4), 1167–1172.

[8] Lam, B.; Das, J.; Holmes, R. D.; Live, L.; Sage, A.; Sargent, E. H.; Kelley, S. O. Solution-Based Circuits Enable Rapid and Multiplexed Pathogen Detection. *Nat. Commun.* **2013**, *4*, 2001.

[9] Rusling, J. F. Multiplexed Electrochemical Protein Detection and Translation to Personalized Cancer Diagnostics. *Anal. Chem.* **2013**, *85* (11), 5304–5310.

[10] Lequin, R. M. Enzyme Immunoassay (EIA)/Enzyme-Linked Immunosorbent Assay (ELISA). *Clin. Chem.* **2005**, *51* (12), 2415–2418.

[11] Zhang, Y.; Guo, Y.; Xianyu, Y.; Chen, W.; Zhao, Y.; Jiang, X. Nanomaterials for Ultrasensitive Protein Detection. *Adv. Mater. Deerfield Beach Fla* **2013**, *25* (28), 3802–3819.

[12] Dixit, C. K.; Kadimisetty, K.; Otieno, B. A.; Tang, C.; Malla, S.; Krause, C. E.; Rusling, J. F. Electrochemistry-Based Approaches to Low Cost, High Sensitivity, Automated, Multiplexed Protein Immunoassays for Cancer Diagnostics. *The Analyst* **2016**, *141* (2), 536–547.

[13] Otieno, B. A.; Krause, C. E.; Latus, A.; Chikkaveeraiah, B. V.; Faria, R. C.; Rusling, J. F. On-Line Protein Capture on Magnetic Beads for Ultrasensitive Microfluidic Immunoassays of Cancer Biomarkers. *Biosens. Bioelectron.* **2014**, *53*, 268–274.

[14] Krause, C. E.; Otieno, B. A.; Latus, A.; Faria, R. C.; Patel, V.; Gutkind, J. S.; Rusling, J. F. Rapid Microfluidic Immunoassays of Cancer Biomarker Proteins Using Disposable Inkjet-Printed Gold Nanoparticle Arrays. *ChemistryOpen* **2013**, *2* (4), 141–145.

[15] Zhang, L.; Zhai, Y.; Gao, N.; Wen, D.; Dong, S. Sensing H2O2 with Layer-by-Layer Assembled Fe3O4–PDDA Nanocomposite Film. *Electrochem. Commun.* **2008**, *10* (10), 1524–1526.

[16] Chang, Q.; Deng, K.; Zhu, L.; Jiang, G.; Yu, C.; Tang, H. Determination of Hydrogen Peroxide with the Aid of Peroxidase-like Fe3O4 Magnetic Nanoparticles as the Catalyst. *Microchim. Acta* **2009**, *165* (3–4), 299.

[17] Liu, Y.; Yuan, M.; Qiao, L.; Guo, R. An Efficient Colorimetric Biosensor for Glucose Based on Peroxidase-like Protein-Fe3O4 and Glucose Oxidase Nanocomposites. *Biosens. Bioelectron.* **2014**, *52*, 391–396.

[18] Wei, H.; Wang, E. Fe3O4 Magnetic Nanoparticles as Peroxidase Mimetics and Their Applications in H2O2 and Glucose Detection. *Anal. Chem.* **2008**, *80* (6), 2250–2254.

[19] Ma, M.; Xie, J.; Zhang, Y.; Chen, Z.; Gu, N. Fe3O4@Pt Nanoparticles with Enhanced Peroxidase-like Catalytic Activity. *Mater. Lett.* **2013**, *105*, 36–39.

[20] Fang, H.; Pan, Y.; Shan, W.; Guo, M.; Nie, Z.; Huang, Y.; Yao, S. Enhanced Nonenzymatic Sensing of Hydrogen Peroxide Released from Living Cells Based on Fe3O4/Self-Reduced Graphene Nanocomposites. *Anal. Methods* **2014**, *6* (15), 6073–6081.

[21] Liu, X.; Zhu, H.; Yang, X. An Amperometric Hydrogen Peroxide Chemical Sensor Based on Graphene-Fe3O4 Multilayer Films Modified ITO Electrode. *Talanta* **2011**, *87*, 243–248.

[22] Yang, X.; Wang, L.; Zhou, G.; Sui, N.; Gu, Y.; Wan, J. Electrochemical Detection of H2O2 Based on Fe3O4 Nanoparticles with Graphene Oxide and Polyamidoamine Dendrimer. *J. Clust. Sci.* **2014**, *26* (3), 789–798.

[23] Sun, X.; Guo, S.; Liu, Y.; Sun, S. Dumbbell-like PtPd–Fe3O4 Nanoparticles for Enhanced Electrochemical Detection of H2O2. *Nano Lett.* **2012**, *12* (9), 4859–4863.

[24] Sun, H.; Jiao, X.; Han, Y.; Jiang, Z.; Chen, D. Synthesis of Fe3O4-Au Nanocomposites with Enhanced Peroxidase-Like Activity. *Eur. J. Inorg. Chem.* **2013**, *2013* (1), 109–114.

[25] Gao, L.; Wu, J.; Lyle, S.; Zehr, K.; Cao, L.; Gao, D. Magnetite Nanoparticle-Linked Immunosorbent Assay. *J. Phys. Chem. C* **2008**, *112* (44), 17357–17361.

[26] Zhang, Z.; Wang, Z.; Wang, X.; Yang, X. Magnetic Nanoparticle-Linked Colorimetric Aptasensor for the Detection of Thrombin. *Sens. Actuators B Chem.* **2010**, *147* (2), 428–433.

[27] Wei, Q.; Xiang, Z.; He, J.; Wang, G.; Li, H.; Qian, Z.; Yang, M. Dumbbell-like Au-Fe3O4 Nanoparticles as Label for the Preparation of Electrochemical Immunosensors. *Biosens. Bioelectron.* **2010**, *26* (2), 627–631.

[28] Dong, Y.; Zhang, H.; Rahman, Z. U.; Su, L.; Chen, X.; Hu, J.; Chen, X. Graphene Oxide-Fe3O4 Magnetic Nanocomposites with Peroxidase-like Activity for Colorimetric Detection of Glucose. *Nanoscale* **2012**, *4* (13), 3969–3976.

[29] Wu, X.; Zhang, Y.; Han, T.; Wu, H.; Guo, S.; Zhang, J. Composite of Graphene Quantum Dots and Fe3O4 Nanoparticles: Peroxidase Activity and Application in Phenolic Compound Removal. *RSC Adv.* **2013**, *4* (7), 3299–3305.

[30] Liu, M.; Chen, C.; Hu, J.; Wu, X.; Wang, X. Synthesis of Magnetite/Graphene Oxide Composite and Application for Cobalt(II) Removal. *J. Phys. Chem. C* **2011**, *115* (51), 25234–25240.

[31] Han, Q.; Wang, Z.; Xia, J.; Chen, S.; Zhang, X.; Ding, M. Facile and Tunable Fabrication of Fe3O4/Graphene Oxide Nanocomposites and Their Application in the Magnetic Solid-Phase Extraction of Polycyclic Aromatic Hydrocarbons from Environmental Water Samples. *Talanta* **2012**, *101*, 388–395.

[32] Jiao, T.; Liu, Y.; Wu, Y.; Zhang, Q.; Yan, X.; Gao, F.; Bauer, A. J. P.; Liu, J.; Zeng, T.; Li, B. Facile and Scalable Preparation of Graphene Oxide-Based Magnetic Hybrids for Fast and Highly Efficient Removal of Organic Dyes. *Sci. Rep.* **2015**, *5*, 12451.

[33] Wei, H.; Yang, W.; Xi, Q.; Chen, X. Preparation of Fe3O4@graphene Oxide Core–Shell Magnetic Particles for Use in Protein Adsorption. *Mater. Lett.* **2012**, *82*, 224–226.

[34] Deng, H.; Li, X.; Peng, Q.; Wang, X.; Chen, J.; Li, Y. Monodisperse Magnetic Single-Crystal Ferrite Microspheres. *Angew. Chem. Int. Ed.* **2005**, *44* (18), 2782–2785.

[35] Kim, M. I.; Kim, M. S.; Woo, M.-A.; Ye, Y.; Kang, K. S.; Lee, J.; Park, H. G. Highly Efficient Colorimetric Detection of Target Cancer Cells Utilizing Superior Catalytic Activity of Graphene Oxide-Magnetic-Platinum Nanohybrids. *Nanoscale* **2014**, *6* (3), 1529–1536.

[36] Hummers, W. S.; Offeman, R. E. Preparation of Graphitic Oxide. *J. Am. Chem. Soc.* **1958**, *80* (6), 1339–1339.

[37] Sheng, K.; Sun, Y.; Li, C.; Yuan, W.; Shi, G. Ultrahigh-Rate Supercapacitors Based on Eletrochemically Reduced Graphene Oxide for Ac Line-Filtering. *Sci. Rep.* **2012**, *2*.

[38] Malhotra, R.; Patel, V.; Chikkaveeraiah, B. V.; Munge, B. S.; Cheong, S. C.; Zain, R. B.; Abraham, M. T.; Dey, D. K.; Gutkind, J. S.; Rusling, J. F. Ultrasensitive Detection of Cancer

Biomarkers in the Clinic by Use of a Nanostructured Microfluidic Array. *Anal. Chem.* **2012**, *84* (14), 6249–6255.

[39] Loh, K. P.; Bao, Q.; Eda, G.; Chhowalla, M. Graphene Oxide as a Chemically Tunable Platform for Optical Applications. *Nat. Chem.* **2010**, *2* (12), 1015–1024.

[40] Biochemica, B. M. G. *Biochemica information: a revised biochemical reference source*; Boehringer Mannheim GmbH, Biochemica, 1987.

[41] Noble, J. E.; Bailey, M. J. A. Quantitation of Protein. *Methods Enzymol.* **2009**, *463*, 73–95.

[42] Smits, F. M. Measurement of Sheet Resistivities with the Four-Point Probe. *Bell Syst. Tech. J.* **1958**, *37* (3), 711–718.

[43] Bard, A. J.; Faulkner, L. R. *Electrochemical Methods: Fundamentals and Applications*; Wiley, 2000.

[44] Stamey, T. A.; Teplow, D. B.; Graves, H. C. B. Identity of PSA purified from seminal fluid by different methods: Comparison by amino acid analysis and assigned extinction coefficients. *The Prostate* **1995**, *27* (4), 198–203.

[45] Smith, R. A.; Cokkinides, V.; Eyre, H. J. American Cancer Society Guidelines for the Early Detection of Cancer, 2005. *CA. Cancer J. Clin.* **2005**, *55* (1), 31–44; quiz 55–56.

[46] O'Keefe, D. S.; Su, S. L.; Bacich, D. J.; Horiguchi, Y.; Luo, Y.; Powell, C. T.; Zandvliet, D.; Russell, P. J.; Molloy, P. L.; Nowak, N. J.; et al. Mapping, Genomic Organization and Promoter Analysis of the Human Prostate-Specific Membrane Antigen Gene. *Biochim. Biophys. Acta* **1998**, *1443* (1–2), 113–127.

[47] Xiao, Z.; Adam, B. L.; Cazares, L. H.; Clements, M. A.; Davis, J. W.; Schellhammer, P. F.; Dalmasso, E. A.; Wright, G. L. Quantitation of Serum Prostate-Specific Membrane Antigen by a Novel Protein Biochip Immunoassay Discriminates Benign from Malignant Prostate Disease. *Cancer Res.* **2001**, *61* (16), 6029–6033.

[48] Mani, V.; Wasalathanthri, D. P.; Joshi, A. A.; Kumar, C. V.; Rusling, J. F. Highly Efficient Binding of Paramagnetic Beads Bioconjugated with 100,000 or More Antibodies to Protein-Coated Surfaces. *Anal. Chem.* **2012**, *84* (23), 10485–10491.

[49] Li, Z. J.; Yang, B. C.; Zhang, S. R.; Zhao, C. M. Graphene Oxide with Improved Electrical Conductivity for Supercapacitor Electrodes. *Appl. Surf. Sci.* **2012**, *258* (8), 3726–3731.

Chapter Three

Accessible Telemedicine Diagnostics with ELISA in a 3D Printed Pipette Tip

3.1 Abstract

We report herein a novel pipette-based "ELISA in a Tip" as a new versatile diagnostic tool featuring better sensitivity, shorter incubation time, accessibility, and low sample and reagent volumes compared to traditional ELISA. Capture and analysis of data by a cell phone facilitates electronic delivery of results to health care providers. Pipette tips were designed and 3D printed as adapters to fit most commercial 50-200 µL pipettes. Capture antibodies (Ab_1) are immobilized on inner walls of the pipette tip that serves as the assay compartment where samples and reagents are moved in and out by pipetting. Signals are generated using colorimetric or chemiluminescent (CL) reagents and can be quantified using a cell phone, CCD camera, or plate reader. We utilized pipette-tip ELISA to detect four cancer biomarkers proteins with detection limits similar to or lower than microplate ELISAs at 25% assay cost and time. Recoveries of these proteins from spiked human serum was 85-115% or better, depending slightly on detection mode. Using CCD camera quantification of CL with femto-luminol reagent gave limits of detection (LOD) as low as 0.5 pg/mL. Patient samples (13) were assayed for 3 biomarker proteins with results well correlated to conventional ELISA and an established microfluidic electrochemical immunoassay.

3.2 Introduction

Enzyme Linked Immunosorbent Assay (ELISA) has long been the gold standard for measuring proteins, pathogens, antibodies and other biomolecules in complex matrices.[1,2,3] Recent research has focused on developing innovative and accessible systems in order to decrease cost and assay time, and increase sensitivity. Many ELISA systems use microplates with different volumes and sizes as assay compartments to immobilize antibodies that specifically capture target molecules followed by labor intensive, time-consuming incubation and washing steps. Recent approaches have included design of new labels to replace enzymes,[4,5] utilizing magnetic beads,[6,7] signal enhancement by nanomaterials,[8] and developing more accessible plate readers.[9,10] 3D printing has been utilized to increase microwell surface area improved the performance of microplate ELISA.[11] Remaining challenges that hinder the use of ELISA for low cost diagnostics include limited surface area for antibody immobilization, fluid handling, multiplexing, and sample size.[12]

Commercial alternatives for biomolecule detection include multiplexed microbead immunoassay technologies with optical or electrochemiluminescent (ECL) readout with LODs for proteins similar to standard ELISA at 1-10 pg mL^{-1}.[13,14,15] The Simoa HD-1[16] single protein counting device detects proteins with much better LODs, e.g. 4-70 fg mL^{-1}.[17] However, instrument and assay costs for these methods are high and prohibitive for many applications.

Incorporation of microfluidics into molecular diagnostic devices facilitates fluid control, decreases sample and reagent volumes, decreases assay time and cost, and can enable remote sensing.[18] Microfluidics has improved immunoassay performance by enhancing reaction kinetics, providing multiplexing and decreasing assay time and cost.[19,20] ELISA has been integrated into PDMS chips,[21,22] centrifugal assay platforms, [23,24] disposable patterned discs [25,26] and microfluidic chips with optical sensor[27] to offer fast, cost-effective alternatives to microplate ELISA. However,

there are as yet few off-the-shelf systems available, so for widespread lab use these approaches will require in-house fabrication that will not be familiar or desirable to many users.[28,29]

3D printing provides fast, low cost, readily accessible fabrication of microfluidic devices.[30,31,32] Desktop 3D printing allows laboratories around the world to reproduce bioanalytical diagnostic microfluidic devices at low cost.[33] 3D printed microfluidic electrochemical immunoarrays have been developed for determining proteins, [34,35,36,37,38] nucleic acids,[39,40,41] and small molecules.[42,43] Other detection modes are also possible and we have reported 3D printed microfluidic immunoarrays to detect up to 8 proteins utilizing electrochemiluminescence (ECL) or chemiluminescence (CL).[44,45,46]

In the present paper, we report the first example of ELISA in 3D printed pipette tips. Our goal was to develop a simple, easy-to-use, low cost methodology for sandwich ELISA assays for virtually any protein. The tips were designed to fit to most commercially available 50-200 µL single and multichannel pipettes. The inner fluidic chamber of the tip serves as a solid support to strongly adsorb chitosan hydrogel, allowing covalent immobilization of capture antibodies (Ab_1). The microfluidic nature of the assay chamber decreases assay time due to larger volume/surface area ratios than microwells. Sample and reagents are drawn into the tip and incubated there, and measurement of resulting absorbance or CL is done with a CCD camera, cell phone or plate reader. Four protein biomarkers, Prostate Specific Antigen (PSA), Vascular Endothelial Growth Factor (VEGF), Insulin like Growth Factor-1 (IGF-1) and Cluster of Differentiation-14 (CD-14), were detected simultaneously using tetramethylbenzidine (TMB) reagent and an 8-channel pipette tip adaptor. Limits of detection (LOD) were 5 pg/mL for PSA, 25 pg/mL for VEGF, 2.5 pg/mL for IGF-1 and 0.5 pg/mL for CD-14 which are lower than or similar to microplate ELISA in <25% of the assay time. Cell phone image capture and analysis was demonstrated for VEGF with LOD 50

pg/mL and for IGF-1 with LOD 20 pg/mL. Integration with chemiluminescence (CL) detection was shown by measuring PSA using West Femto luminol with LOD 1 pg/mL. Recoveries from spiked human serum samples were between 85%-115%. In addition, proteins PSA, CD-14 and IGF-1 were quantified in 13 patient samples and data correlated well with both conventional ELISA and an established electrochemical immunoassay. Cell phone image capture was also used to quantify IGF-1 levels in 13 patient samples with good correlation to conventional ELISA.

3.3 Results and Discussion

Design of ELISA tip adapter. We used 2 different designs for the pipette tips. The first was a single channel tip and the second was an 8-channel tip that fits 8-channel pipettes (Fig. 3.2A). Tips were designed in 123D® design software (Autodesk) and transferred to Form2® stereolithographic 3D printer where they were printed using Formlabs clear resin. The pipette tip has three main compartments, the pipette housing, immunoassay chamber and inlet cylinder. The inlet cylinder has outer diameter 3 mm and 15 mm length, suitable for drawing samples and reagents into the immunoassay chamber from ordinary microcentrifuge tubes. Total fill volume of immunoassay chamber and inlet cylinder is 50±3 µL (45 µL immunoassay chamber 5 µL inlet cylinder). The pipette housing compartment was designed as a conical cylinder to facilitate fitting onto different commercially available pipettes and was equipped with an overflow feature near the immunoassay chamber to prevent possible contamination of the pipette with reagents or samples (Fig. 3.1). Four different commercially available pipettes, Finnpipette® II, Eppendorf®, V-Pette®, and Acumax®, were tested. Designed tips snuggly fitted into these pipettes by applying less than 3 kg of force with pipetted volume variation <±1%.

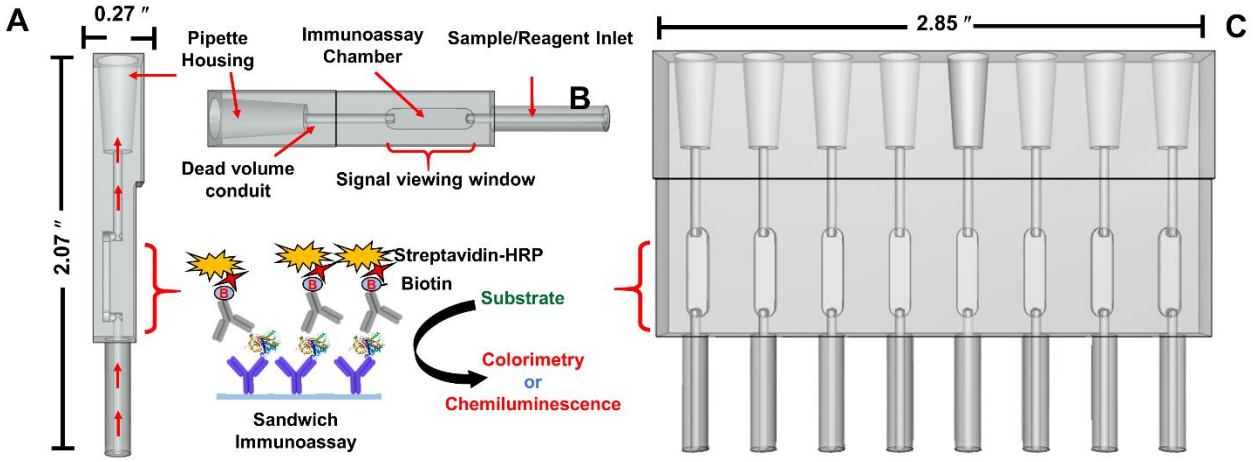

Fig. 3.1 3D Design of ELISA tip platform. (A) A single pipette ELISA tip array, side view showing flow of reagents from bottom into the immunoassay chamber derived by vacuum suction applied through pipette attached at pipette housing on the top. (B) Front view, immunoassay chamber as a colorimetric/chemiluminescent viewing window. Inset showing sandwich immunoassay on the surface of immunoassay chamber. (C) Multi-chamber pipette ELISA tip used via a multichannel pipette for multianalyte or multiplex detection.

Hydrogel film characterization. Chitosan is a naturally occurring polysaccharide that we found to adsorb strongly and irreversibly to the 3D-printed polyacrylate. A flat 1 x 1 cm 3D printed chip was coated with chitosan and used to estimate dry hydrogel film mass/cm^2, swelling ratio %, and antibody coverage/cm^2 in the ELISA tips. White light interferometry analysis of 3D printed surface coated with chitosan on showed large peaks of varying heights (5µm- 33 µm) intercalated with small valleys that occupied ~10% of the chip area (Fig. 3.3).

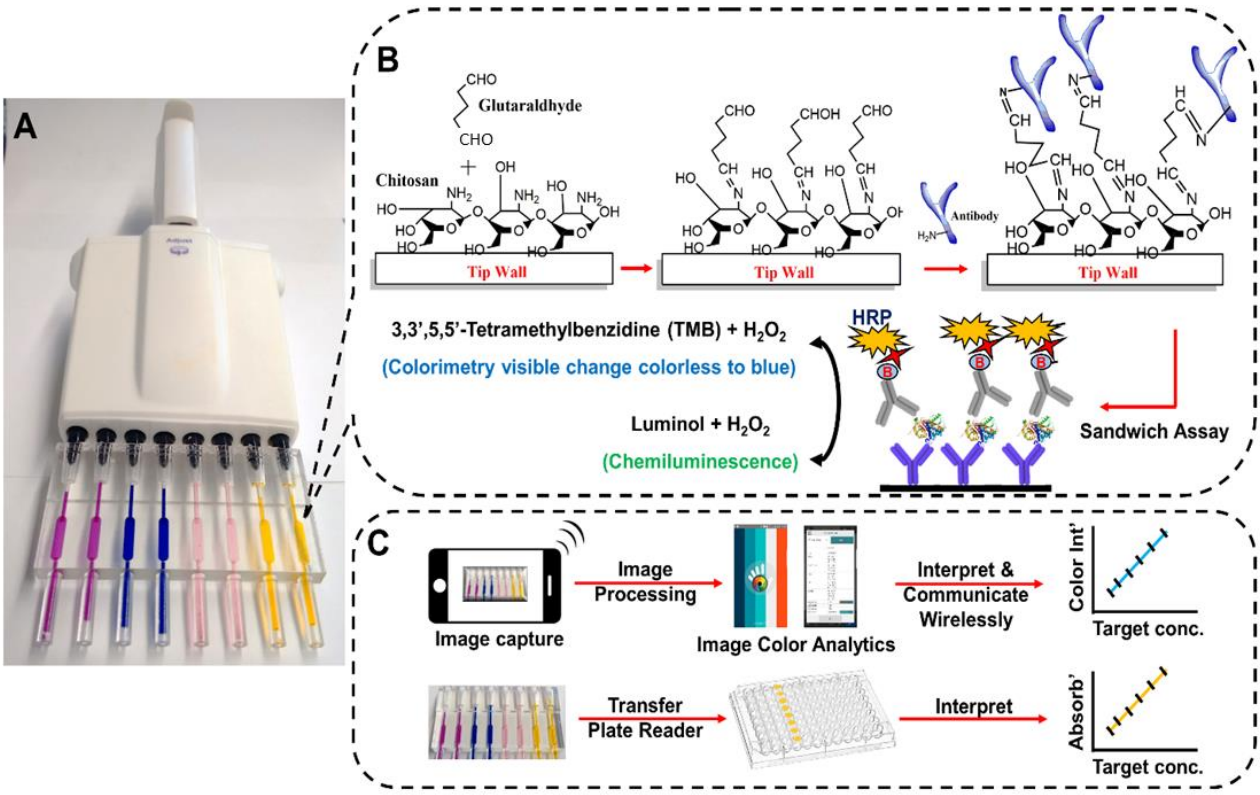

Fig. 3.2 Representation of sandwich immunoassays in ELISA tips with protocols: (A) Fully transparent 8-pipette 3D printed array loaded with food dyes; (B) Schematic illustration of pre-coating steps showing immobilization of capture antibodies on immunoarray tip wall coated with chitosan followed by sandwich immunoassay and signal measurement for colorimetry and CL. (C) Signal capture and processing flow using smartphone or microplate reader.

It is likely that this roughness and chitosan swelling contributes to performance of the tip ELISA as it increases surface area for chitosan-Ab_1 immobilization. Dry film loading capacity of the 3D printed chip was 0.10±0.01 mg chitosan/cm^2. Film mass after hydration with water in a humidity chamber was 1.1±0.05 mg indicated swelling ratio % of 1100% from Eq 1. [47]

$$\text{Swelling ratio (\%)} = \frac{\text{Ws}-\text{Wd}}{\text{Wd}} \times 100\ \% \qquad (1)$$

where W_s is weight of the swollen film and W_d is weight of dry chitosan film. Ab_1 was anchored onto the chitosan film using glutaraldehyde as a cross linker for covalent immobilization (Fig. 3.2B). Ab_1 coverage calculated from BCA total protein assay was 10.0 ± 0.5 µg/cm^2 which is approximately 1.0x10^{13} antibodies/cm^2 (SI, Fig. S4). We also estimated swelling of chitosan film after immobilizing Ab_1. Dried chitosan films with Ab_1 had mass 0.9±0.03 mg and the mass of the chitosan-Ab_1 film after hydration increased to 5.5±0.04 mg for a swelling ratio of 600%.

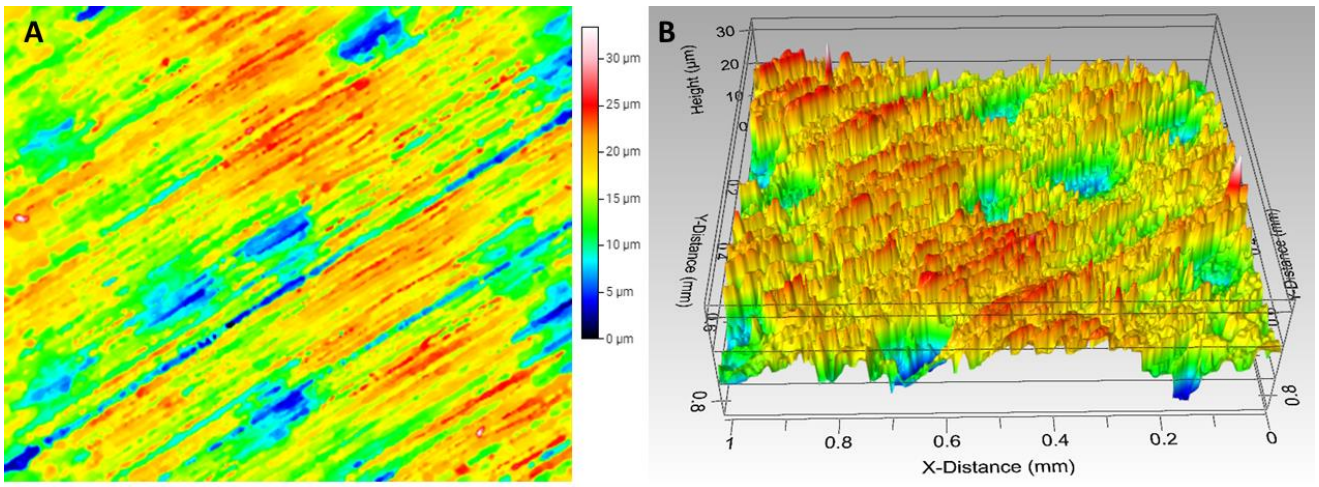

Fig. 3.3 Surface profile of 3D printed chip (A) Top View and (B) 3D view showing surface roughness with peaks of 5-33 µm intercalated by valleys that occupy ~10% of the 3D printed surface

Single Protein Assays. Assay precision was evaluated at several analyte concentrations (n≥ 3) in calf serum (Fig. 3), which is an effective human serum surrogate for immunoassays.[48] Fig. 3.4A shows reproducibility of colorimetry from 4 different tips at 1.3 and 12 ng/mL VEGF in calf serum, Fig. 3D shows images of colorimetric assays from 3 different tips at 1.3 and 5.5 ng/mL IGF-1 in calf serum, Standard deviations for each concentration were reproducible within ±5%. Day-to-day standard deviations were less than ±7%. The assay was also done in cell phone-assisted mode. We utilized a simple photograph, and instant signal integration with a commercial color analytics app, Color Grab (Fig. 3.5). Fig. 3.4B and 3.4E show colorimetric signals imaged after 10 min color

reaction with increasing concentrations of VEGF and IGF-1. Images were captured and analyzed with the Color Grab mobile application. VEGF had a detection limit of 50 pg/mL and dynamic range 50 pg/mL to 10 ng/mL. Fig. 3.4C shows calibration curves obtained by plotting %K values as a measure of color intensity vs. VEGF concentration. IGF-1 had LOD of 20 pg/mL and dynamic range of 20 pg/mL to 5.5 ng/mL. Fig. 3F shows calibration curves obtained by plotting %K values measuring color intensity vs. IGF-1 concentration. Percent recoveries of VEGF from spiked human serum samples were found to validate accuracy of the cell phone-based assay and were 90-110% (Table 1). Stability of antibodies immobilized in the tip was estimated by measuring the same concentration of IGF-1 (625 pg/mL) daily for tips stored at 4˚ C over 7 days. Antibodies lost 5% activity after 3 days and maintained 80% of initial activity after 7 days storage (Fig. 3.6).

CL capture from tips by CCD camera was demonstrated using PSA as the test protein, Here, HRP oxidized femto-luminol to an excited state that decays and emits light that was captured and integrated over 120 s using a CCD camera in a dark box. Fig. 3.4H shows recolorized CL images that showing increased CL intensity with increasing PSA concentration. Fig. 3.4I is a calibration curve obtained by plotting CL intensities against PSA concentration. CL assay for PSA on calf serum had LOD 1 pg/mL and dynamic range from 1 pg/mL to 100 ng/mL.

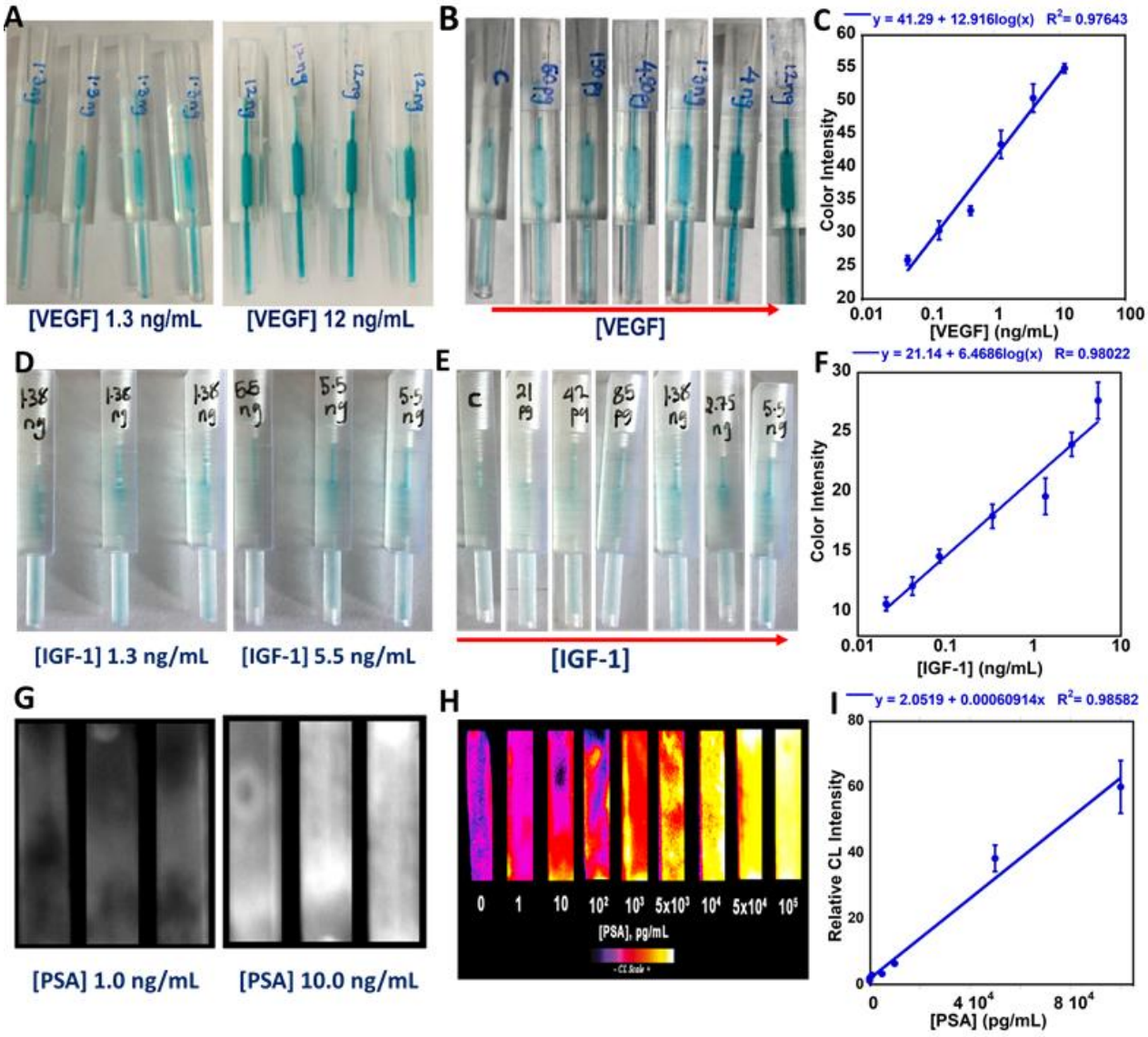

Fig. 1.4 Single tip assays in calf serum using iphone and CCD camera imaging: (A) Reproducibility of colorimetric detection (n=4) for VEGF; (B) Change in colorimetric signal with increasing concentration of VEGF, (C) Calibration curve obtained via iphone imaging color intensity (K%) vs. [VEGF], (D) Reproducibility of colorimetric detection (n=3) for IGF-1; (E) Change in colorimetric signal with increasing concentration of IGF-1, (F) Calibration curve obtained via iphone K% vs. [IGF-1], (G) Raw CL images captured by CCD camera for PSA, (H) Recolorized images showing change in CL intensity vs. [PSA], (I) Calibration curve of relative CL vs. [PSA].

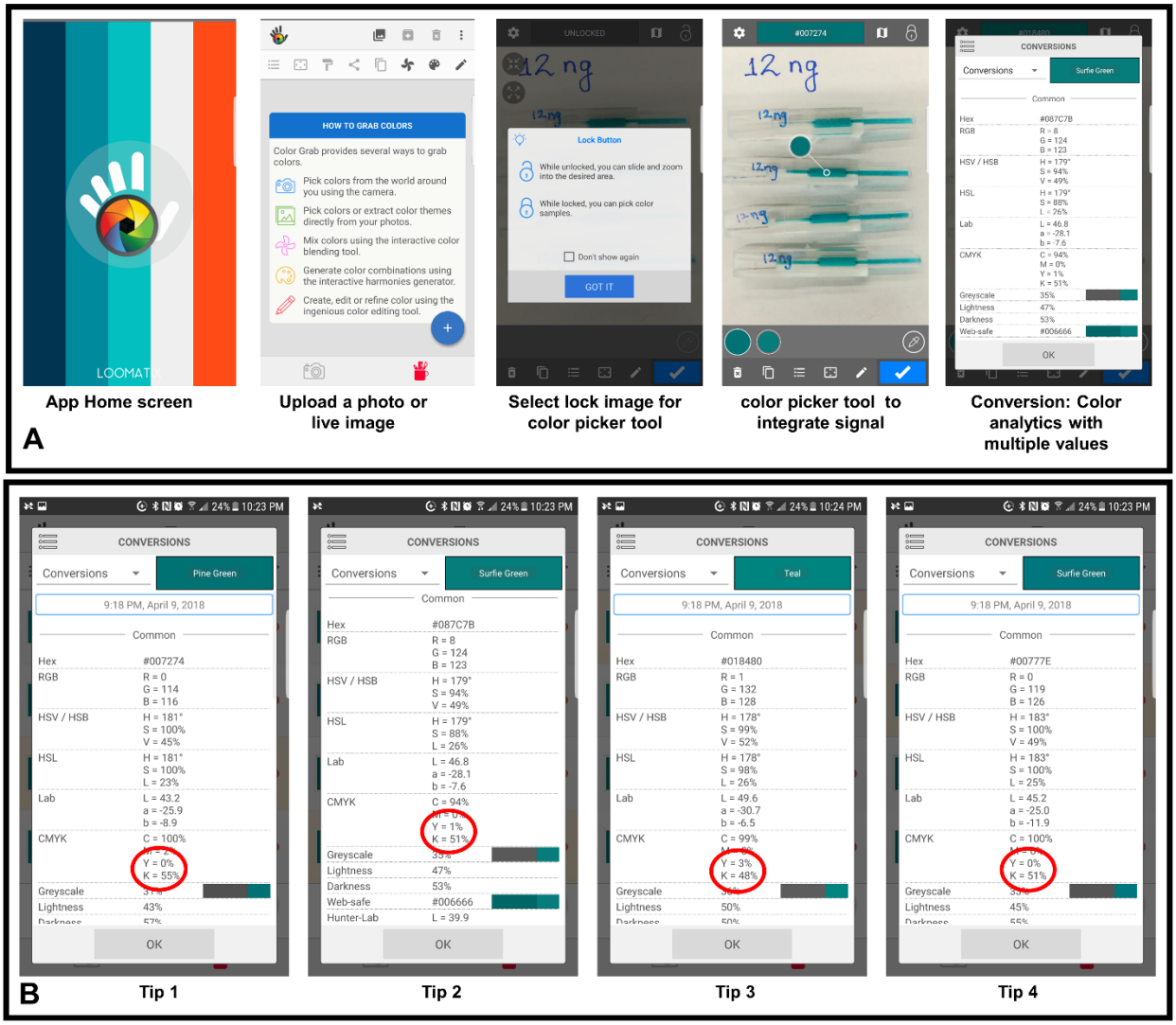

Fig. 3.5 Screen shots from smartphone color analysis software "ColorGrap" of the ELISA in a Tip array. (A) Simple color analysis is showed step wise from upload to a photo to picking color to provide color analytics. (B) Color analysis sample output for 4 tip arrays as a part of reproducibility experiments and highlighted in the red circles is the selected parameter of developing calibration curves.

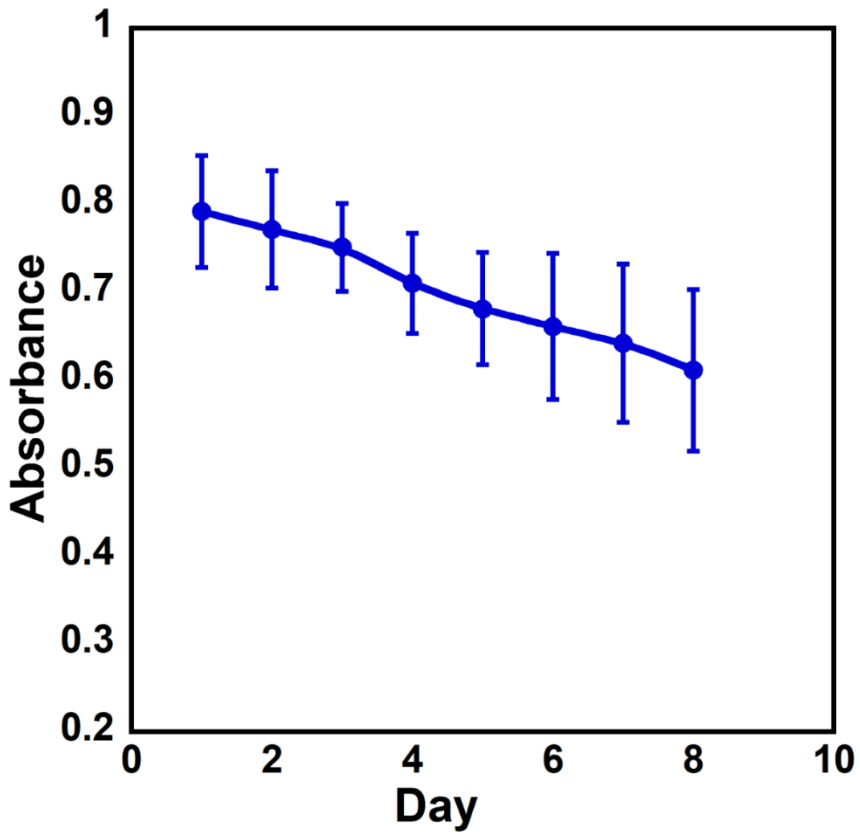

Fig. 3.6 Antibody stability study. Colorimetric absorbance at 450 nm measured after running assay in tips stored at 4˚C for up to 7 days. Tips maintained 80% of its original activity after 7 days of storage (n=3)

Multiplexed ELISA in a tip. The colorimetric assay was tested to simultaneously quantify 4 proteins in undiluted calf serum. A multichannel pipette tip adapter (Fig. 3.2) was used with 2 channels for each protein. Here we used a plate reader for absorbance detection to illustrate versatility of the approach. Fig. 3.7 shows calibration curves for the proteins, where standard deviation for each concentration was less than 15%. LODs were 5 pg/mL for PSA, 25 pg/mL for VEGF, 2.5 pg/mL for IGF-1 and 0.5 pg/mL for CD-14. Dynamic ranges were 5 to 10,000 pg/mL for PSA, 50 to 10,000 pg/mL for VEGF, 4 to 8,000 pg/mL for IGF-1 and 1 to 10,000 pg/mL for CD-14.

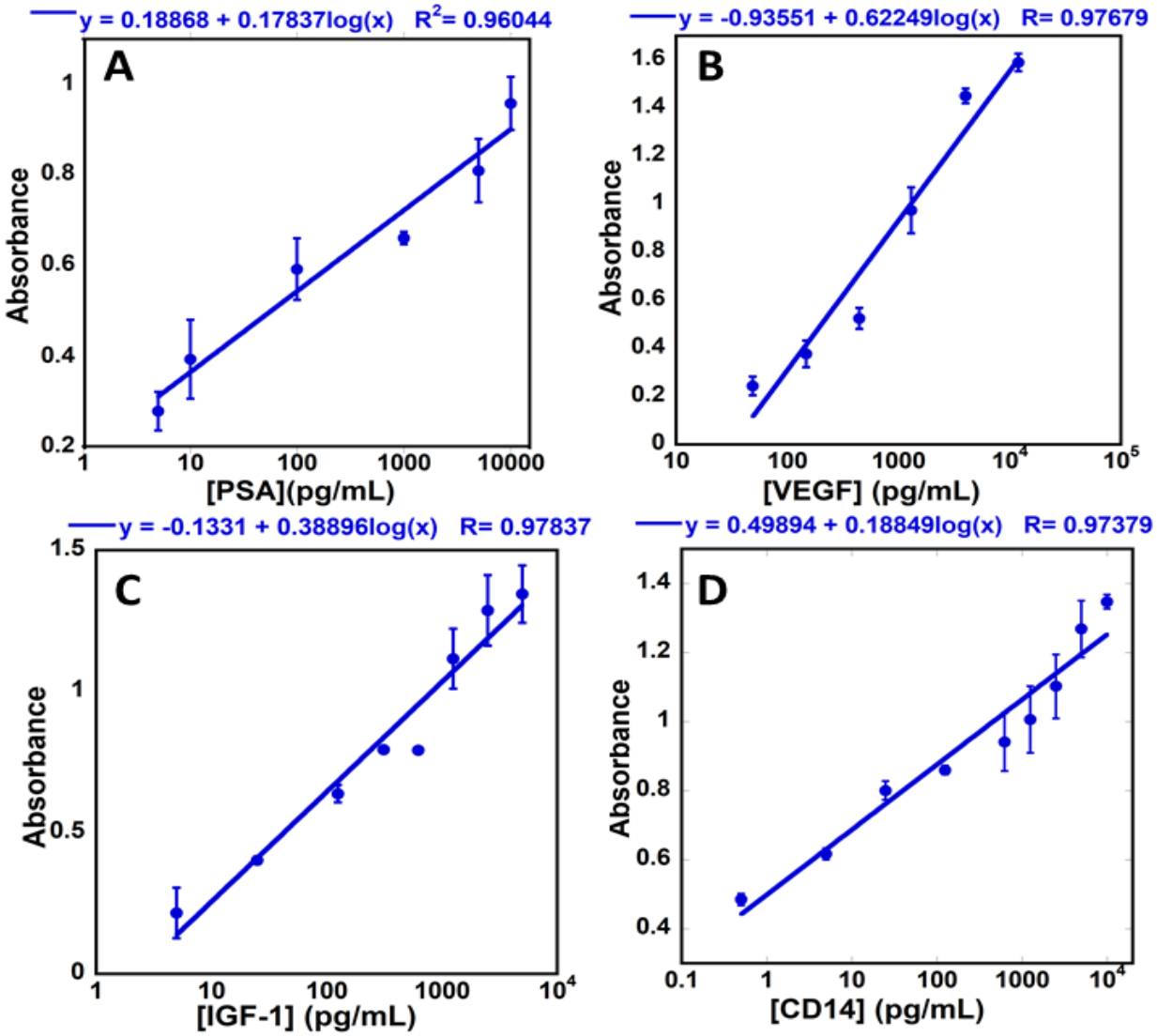

Fig. 3.7 Calibration curves for ELISA tip colorimetric multiplexed detection of (A) PSA, (B) VEGF, (C) IGF-1 and ((D) CD-14. Absorbance was measured at 450 nm in a plate reader (n=4).

Recoveries from spiked, diluted human serum were measured to validate accuracy of multiplexed ELISA in a tip. Human serum was diluted 100-fold before spiking to bring native protein levels below or equal to the protein LODs. Calibration curves in calf serum were used to

estimate recoveries from spiked human serum. Recoveries estimated after subtracting the signals from control serum and were in an analytically acceptable range[49] of 100±20% (Table 1).

Table 3.1. Spike-recovery results from single and multiplex immunoassays in human serum.

Method	Biomarker protein	Spiked concentrations (pg/mL)	Found Concentrations* (pg/mL)	(%) recovery (±SD)
Cell phone-assisted Single Tip Assay	**VEGF**	100	107 (± 6)	107 (± 7)
		1000	950 (± 84)	95 (± 9)
		4000	4133 (± 454)	103(± 7)
Colorimetric 8 Chamber Tip Assay	**PSA**	20	21 (± 1.5)	105 (± 7)
		300	296 (± 38)	98 (± 13)
		2000	2397 (± 144)	119 (± 6)
	VEGF	125	122 (± 15)	98 (± 12)
		500	436 (± 42)	87 (± 9)
		2000	2051 (± 287)	102 (±14)
	IGF-1	125.0	121 (± 16)	100 (± 13)
		800	925 (± 138)	98.5 (± 15)
		2000	2134 (± 320)	93 (± 15)
	CD-14	10	11 (± 0.89)	113 (± 7)
		500	450 (± 43)	90 (± 9)
		5000	5402 (± 486)	108 (± 9)
***after subtraction of the control human serum concentration**				

Patient sample analyses. PSA, IGF-1 and CD-14 represent promising biomarkers for prostate cancer diagnostics.[50,51,52] and were measured in 13 patient serum samples by multiplexed analysis. The sample cohort consisted of 3 normal cancer-free individuals, 5 samples collected from patients with indolent prostate cancer (Gleason score <7) and 5 samples from patients with aggressive prostate cancer (Gleason score >7). Samples were analyzed by colorimetric tip ELISA and results

were compared to both micro-well plate ELISA (Table 3.2-3.4) and an established validated microfluidic electrochemical assay.

Table 3.2. Comparison between calculated conc. of PSA in patient samples between Micro-well ELISA and Tip-ELISA

Cancer Status	Patient Sample Code	PSA			
		Tip-ELISA		Micro-well ELISA	
		Found Conc. ng/mL	St. Dev.	Found Conc. ng/mL	St. Dev.
Controls	**C3**	0.21	0.00	0.72	0.08
	C8	0.49	0.04	0.45	0.03
	C18	0.28	0.01	1.23	0.17
Indolent Prostate cancer (Gleason score <7)	**23**	1.01	0.45	8.87	1.15
	24	0.31	0.03	0.23	0.02
	25	2.81	0.03	0.72	0.06
	27	4.77	0.75	10.70	1.18
	28	1.27	0.01	1.58	0.16
Aggressive Prostate cancer (Gleason score >7)	**1114**	3.09	0.14	2.54	0.15
	1115	9.45	17.20	10.81	1.41
	1123	7.90	18.10	2.34	0.05
	1136	1030.67	33.74	800.05	56.00
	1138	64.25	1.80	62.61	5.01

Table 3.3. Comparison between calculated conc. of IGF-1 in patient samples between Micro-well ELISA and Tip-ELISA

Cancer Status	Patient Sample Code	IGF-1			
		Tip-ELISA		Micro-well ELISA	
		Found Conc. ng/mL	St. Dev.	Found Conc. ng/mL	St. Dev.
Controls	**C3**	6.99	0.04	4.27	0.05
	C8	5.97	0.07	4.78	0.04
	C18	4.81	0.00	5.02	0.07
Indolent Prostate cancer (Gleason score <7)	**23**	2.77	0.12	2.35	0.02
	24	31.45	0.40	26.83	0.13
	25	2.42	0.01	2.28	0.00
	27	1.83	0.00	2.07	0.01
	28	2.32	0.03	2.13	0.01
Aggressive Prostate cancer (Gleason score >7)	**1114**	24.84	0.15	24.65	0.35
	1115	29.36	0.85	29.37	0.21
	1123	11.13	0.00	9.60	0.07
	1136	2.46	0.71	2.16	0.02
	1138	3.24	0.47	2.30	0.18

Table 3.4. Comparison between calculated conc. of CD-14 in patient samples between Micro-well ELISA and Tip-ELISA

Cancer Status	Patient Sample Code	CD-14			
		Tip-ELISA		Micro-well ELISA	
		Found Conc. ng/mL	St. Dev.	Found Conc. ng/mL	St. Dev.
Controls	**C3**	0.17	0.01	0.35	0.03
	C8	0.26	0.01	0.53	0.07
	C18	0.76	0.07	0.87	0.07
Indolent Prostate cancer (Gleason score <7)	**23**	0.66	0.01	1.07	0.10
	24	0.62	0.03	1.25	0.04
	25	1.14	0.03	1.20	0.08
	27	4.90	0.20	4.82	0.05
	28	1.48	0.10	1.12	0.13
Aggressive Prostate cancer (Gleason score >7)	**1114**	2855.21	6.75	2220.26	310.84
	1115	3006.53	9.82	3053.69	335.91
	1123	2530.48	20.15	2434.10	121.70
	1136	602.40	33.24	610.16	42.71
	1138	532.71	34.37	630.76	94.61

Tip ELISA gave excellent correlation with microwell ELISA and the electrochemical assay as demonstrated by correlation coefficients and slopes near 1.0 and intercepts near zero. Correlation coefficients with the electrochemical assay were 0.999 for PSA, 0.991 for IGF-1, and 0.992 for CD-14 and slopes were 1.17 for PSA, 0.87 for IGF-1 and 1.23 for CD-14 (Fig. 3.8).

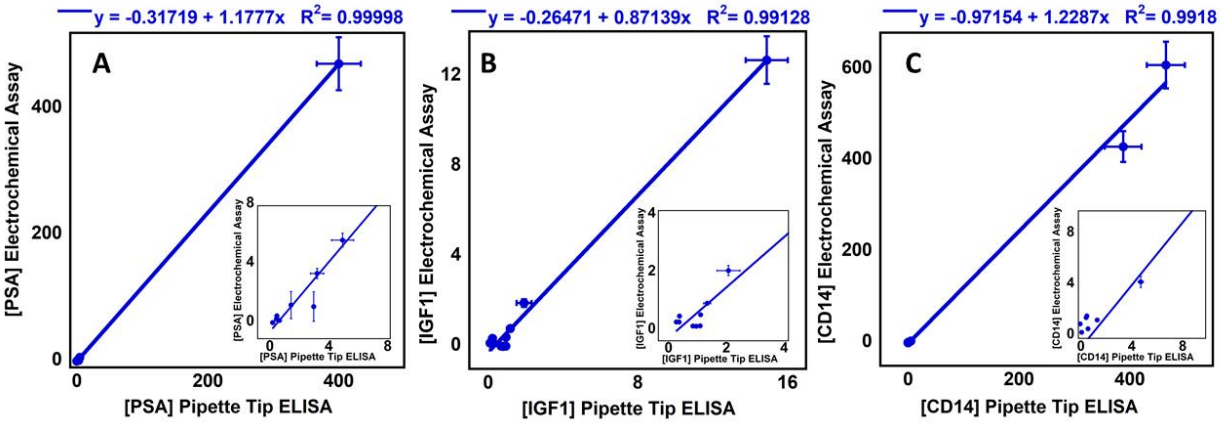

Fig. 3.8 Linear correlations for pipette tip ELISA vs. referee assay for (A) PSA, (B) IGF1, and (C) CD14, quantified in ng/mL (n=3) in patient samples. Insets show low concentration ranges.

Correlation coefficients with micro-well plate ELISA were 0.999 for PSA, 0.986 for IGF-1 and 0.981 for CD-14 and slopes were 0.775 for PSA, 0.949 for IGF-1 and 0.917 for CD-14 (Fig. 3.9).

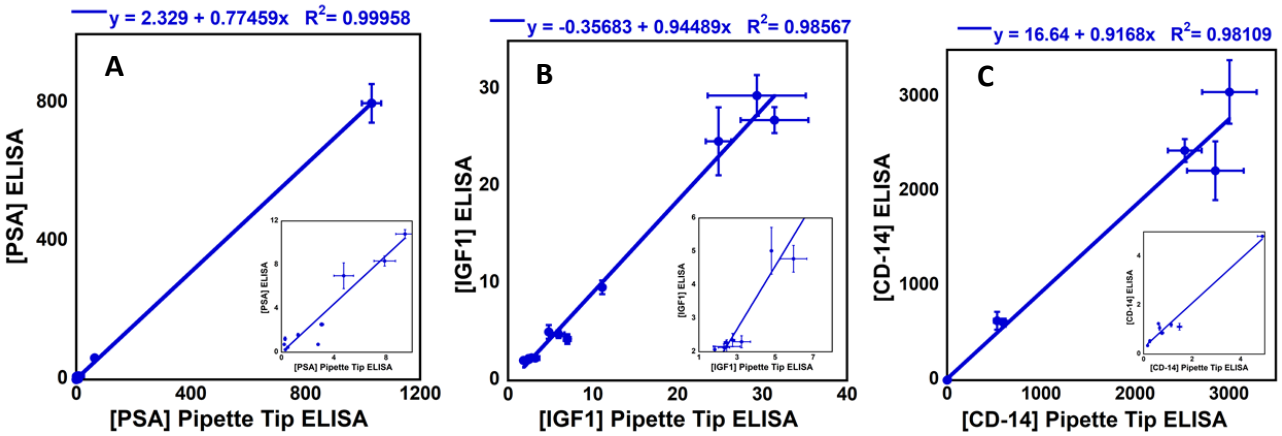

Fig. 3.9 Linear correlations for pipette tip ELISA vs. micro-well plate ELISA for (A) PSA, (B) IGF1, and (C) CD14, quantified in ng/mL (n=3) in patient samples. Insets show low concentration ranges.

IGF-1 concentration in 10X diluted serum samples was also estimated using iphone imaging colorimetric assay and had correlation coefficient of 0.973 vs. conventional ELISA with slope of 0.978 (Fig. 3.10 and Table 3.5). Linear correlations of tip ELISA with the referee methods gave correlation coefficients for the three proteins >0.90, slopes close to unity, and intercepts close to zero. Insets show correlations in the lower concentration range.

Table 3.5. Comparison between calculated conc. of IGF-1 in patient samples between Micro-well ELISA and Tip-ELISA using smart phone imaging with ColorGrab®

Cancer Status	Patient Sample Code	IGF-1			
		Tip-ELISA		Micro-well ELISA	
		Found Conc. ng/mL	St. Dev.	Found Conc. ng/mL	St. Dev.
Controls	**C3**	4.78	0.15	4.27	0.05
	C8	4.90	0.10	4.78	0.04
	C18	5.26	0.16	5.02	0.07
Indolent Prostate cancer (Gleason score <7)	**23**	1.81	0.06	2.35	0.02
	24	28.68	0.78	26.83	0.13
	25	2.29	0.03	2.28	0.00
	27	1.46	0.19	2.07	0.01
	28	2.29	0.13	2.13	0.01
Aggressive Prostate cancer (Gleason score >7)	**1114**	19.39	0.84	24.65	0.35
	1115	31.16	2.67	29.37	0.21
	1123	8.45	0.24	9.60	0.07
	1136	1.60	0.10	2.16	0.02
	1138	2.29	0.13	2.30	0.18

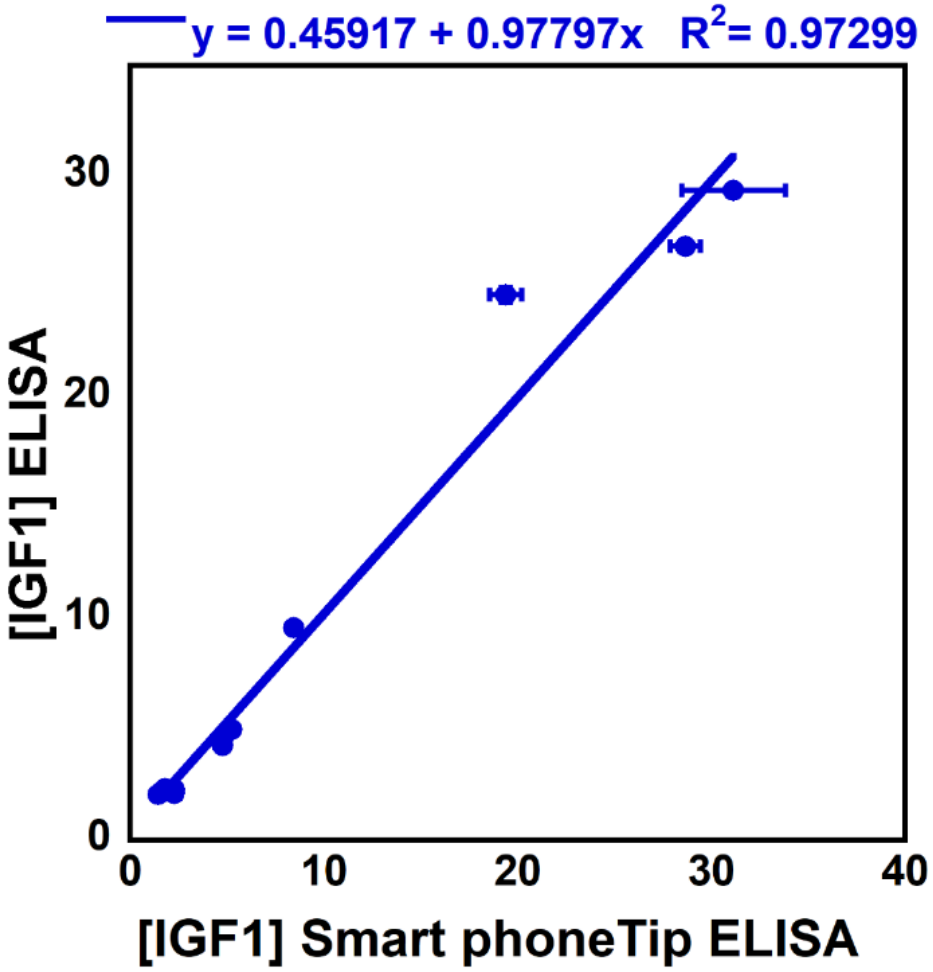

Fig. 3.10 Linear correlations for smart phone pipette tip ELISA vs. referee assay for IGF-1, quantified in ng/mL (n=3) in patient samples.

While the number of samples is much too small for definitive conclusions, receiver operator characteristics (ROC) were analyzed for preliminary diagnostic predictions (Fig. 3.11).

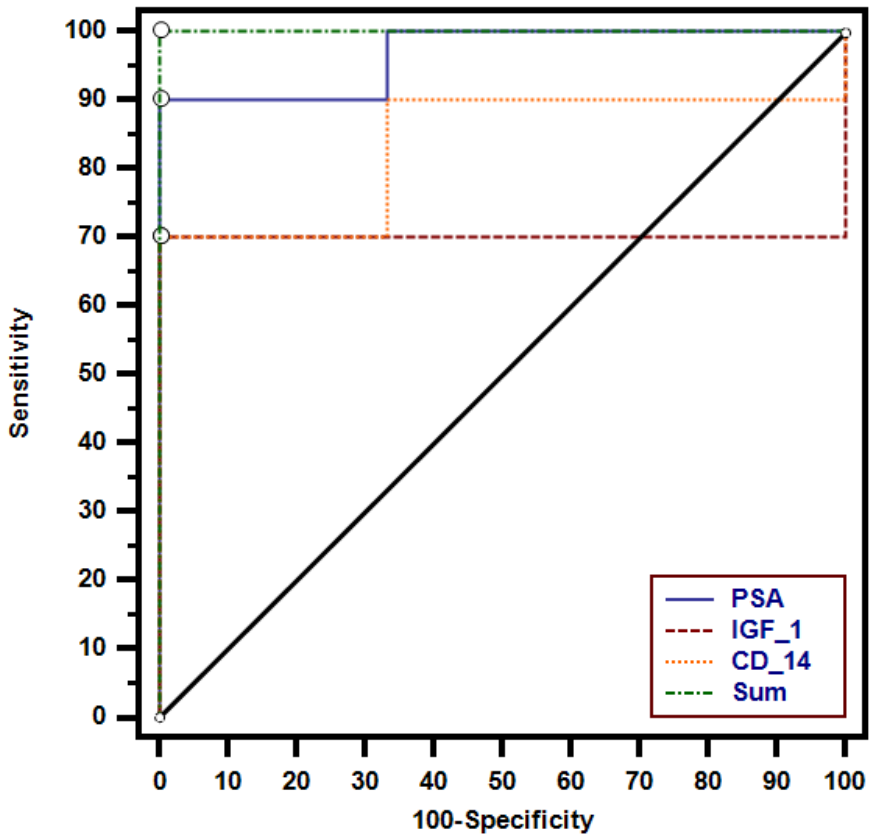

Fig. 3.11 Receiver operating characteristic (ROC) curve for PSA (blue), IGF-1 (red), CD-14 (orange) and sum of the values of the 3 biomarkers (green). Data collected from analysis of 13 real human samples consisting of 3 controls and 10 prostate cancer samples. AUC were 0.967 for PSA, 0.700 for IGF-1, 0.833 for CD-14 and 1.000 for the sum of the concentrations of the 3 biomarkers.

PSA show moderate increases for cancer and aggressive cancer samples, while CD-14 shows very large increase for aggressive prostate cancer. In addition, clustered multiple variables box plots [53] show the found expressions of the three biomarkers in the human serum samples (Fig. 3.12)

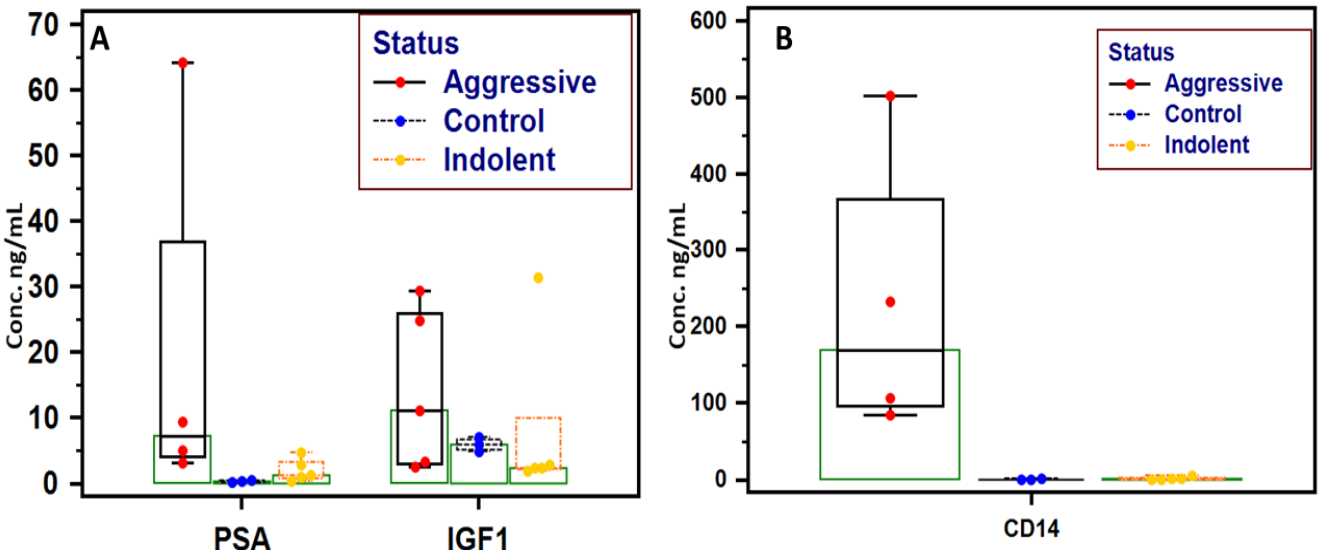

Fig. 3.12 Box-and-whisker plots representing amounts of each biomarker in the human samples: (A) PSA and IGF-1 serum level comparison; (B) CD-14 serum level comparison between control group (blue), indolent prostate cancer group (yellow), and aggressive prostate cancer group (red). Results obtained from tip-based assay using colorimetric procedures (n=3).

Results above demonstrate a novel ELISA in a tip strategy utilizing 25% smaller reagent and samples volumes and 25% shorter assay time than traditional ELISA (Table 3.6). ELISA in a tip offers opportunities that can allow decreases in instrumentation cost and size, e.g. by using cell phone data capture and analysis. The latter approach also facilitates electronic reporting to relevant health care providers and the patients themselves. We demonstrated sensitive detection of 4 cancer biomarkers proteins simultaneously with ELISA in a tip. Users with pipette use knowledge or training should be able to run the assays effortlessly, facilitating use in areas with limited resources.

Pipetting speed and accuracy may slightly affect the performance of the assay, and we did not notice significant variation between users. We believe developing future automated systems engineered for the pipette-tip assay may eliminate user-to-user variation.

Antigen-antibody reactions at a solid-liquid interface as in microplate ELISA are limited by diffusion and antigens, available to interact with immobilized antibodies, are depleted with time.[54,55] Reagent volume/surface area ratios are 131 µL/cm^2 for microwells and 31 µL/cm^2 for the pipette tip chamber. This 4-time lower volume/surface area ratio improves Ag-Ab interaction kinetics reflected in better sensitivities and shorter assay times.

The roughness of the 3D printed surface (Fig. 3.3) of the tip and the use of a highly swelled hydrogel also contribute to effective surface area, which increases the antibody surface loading capacity.[56] Antibody loading in 3D printed tips was 10.0±0.5 µg/cm^2 which is 15-50 times higher than reported capacities for commercial microplates (200-650 ng/cm^2).[57] This high surface loading helped reducing assay time while maintaining similar sensitivity to conventional ELISA. In addition, covalent immobilization of antibodies onto chitosan hydrogel maintains high activity compared to documented loss of activity for passively adsorbed antibodies on polymers surfaces that induce antibody denaturation.[58,59,60]

Table 3.6. Comparison between ELISA in a TIP vs. microplate ELISA

Comparison Type	Tip ELISA (Colorimetry)	Tip ELISA (Chemiluminescence)	Tip ELISA (Cell-phone)	Traditional ELISA
ASSAY TIME				
Sample incubation	30 min	30 min	30 min	150 min
Detection antibody	20 min	20 min	20 min	60 min
Streptavidin-HRP	15 min	15 min	15 min	45 min
Development & Quench	12 min	12 min	12 min	32 min
Detection	2 min	2 min	3-5 sec	2 min
Approx. total wash time	6 min	6 min	6 min	9 min
Total Assay Time	85 min	85 min	83 min	298 min
Reagent/sample volume	50 µL for sample and wash	50 µL for sample and wash	50 µL for sample and wash	150 µL (sample) 300 µL (wash)
LOD (pg/mL) & Dynamic range (pg/mL)	PSA - 5 & 5-10000 VEGF – 25 & 50 - 10000 IGF-1 4 & 4 – 8000 CD-14 - 0.5 & 1-10000	PSA 1 & 1-100,000	IGF-1 20 & 20 – 5500 VEGF 50 & 50 - 10000	PSA - 900 & 900 - 60000 VEGF – 25 & 35 - 2000 IGF-1 – 100 & 100 - 8000 CD-14 - 62 & 62 - 4000
Assay cost per microwell	$1.20/ single tip	$1.20/ single tip	$1.20/ single tip	$4.14/ micro well (Human PSA ELISA Kit – $398)
Required Instrument	Plate reader	CCD Camera	Smart phone	No
Operator	Professional	Simple training	Simple training	Professional
Multiplexity	Yes	Yes	Yeas	No

The transparent tips 3D printed with a low-cost stereolithographic printer was shown to be applicable to colorimetric (Fig. 3.4) and CL detection. CL assays detected of PSA from complex serum matrix with detection limits of 1 pg/mL (Fig. 3.4). No additional steps or modifications are required for CL detection compared to colorimetric assays. CL arrays can be easily integrated with a cell phone making them available for resource limited settings.[61,62] The "ELISA in a Tip" platform was also customized to multiplex multiple analytes and multi-sample assays simultaneously. CAD files for ELISA tip printing can be found at https://rusling.research.uconn.edu/research/3d-printing-designs/. The simple design facilitates extension for multichannel pipettes with 12, 16, 48 & 64 channels.

Cell phone interfacing can enable 3D printed tip arrays for resource limited settings. Using free, commercially available, software 'Color Grab' we demonstrated sensitive detection of colorimetric signals right directly from the tip array and validated accuracy of detection with spiked human serum (Table 3.1) and analyzing real serum samples (Table 3.5). Interfacing cell phones could also help in telemedicine to establish networks between assay technician, centralized labs and physicians. At rural sites in developing countries where availability of resources for traditional ELISA may be limited, cell phone analysis of Tip ELISA can be used at a fraction of the cost and time of standard ELISA kits.

In summary, we describe and demonstrate above an "ELISA in a tip" immunoassay tool designed by 3D printing immunoassay tips for conventional pipettes. "ELISA in a tip" can provide better LODs and dynamic range than microwell ELISA kits, at lower cost, sample volume, and assay time. Multiple signal detection strategies and multiplexed detection are accommodated. Cell phone integration enables the prospect of low-cost detection diagnostics and telemedical communication in normal and low resource environments. This new approach offers a versatile,

sensitive, multiplexing, immunoassay with tips that any lab with a stereolithographic 3D printer can access, with capability that is faster and cheaper than conventional ELISA and may be particularly useful in resource-limited venues.

3.4 Materials and Methods

Materials. All reagents and chemicals were of analytical grade. Chitosan (low molecular weight) and glutaraldehyde were from Sigma Aldrich. Blocker casein in PBS buffer was from Thermo Fisher. ELISA kits for Prostate Specific Antigen (PSA) (DY1344), Vascular endothelial growth factor (VEGF) (DY293B), Insulin-Like Growth Factor 1 (IGF-1) (DY291) and Cluster of Differentiation-14 (CD-14) (DY383) were from R&D systems. Colorimetric signals were generated using R&D systems substrate reagent pack with tetramethylbenzidine (TMB) color reagent and peroxide mixed immediately before use. Chemiluminescence (CL) was generated using Thermo Fisher Supersignal® West Femto chemiluminescent substrate, with luminol and peroxide mixed right immediately before use. All colorimetric measurements were performed after transferring the solutions after color was developed to microplate and absorbance was measured using Synergy® HTX plate reader. CL was measured in pipette tips using a Syngene® dark box with CCD camera. Images were processed using GeneSnap® software. Mobile phone image processing was done using an android/iPhone compatible application Loomatix ColorGrab®. Human prostate cancer patient serum samples and controls were from George Washington University (GWU) Hospital under IRB ethical approval.

Antibody immobilization. Inner walls of tips were coated with a polymeric hydrogel layer of chitosan by dispensing 50 µL of 0.25% chitosan in 0.05 M HCl (pH.4.0) solution into the pipette tip and incubating 3 hrs. Solution was then removed and pipette tips allowed to dry under vacuum at room temperature for 3 hrs, forming a thin, stable film of chitosan onto the inner walls. Amine groups of the hydrogel layer were then activated by filling the tip with 50 µL of 3% glutaraldehyde

in phosphate buffer (PBS, pH.7.4), then incubated for another 3 hrs. Glutaraldehyde solution was then removed and tips were washed with PBS. 50 µL of antibody solution at desired concentrations was pipetted into the tips, which were then incubated overnight (Fig. 3.2B). To compare to microwell plate ELISA, all antibodies were used at concentrations recommended by ELISA kit suppliers. After incubation, antibody solutions were removed, and tips were washed with phosphate buffer- 0.05% Tween 20 solution (PBS-T20, pH.7.4) to remove unbound antibodies and inhibit non-specific binding (NSB).

Chitosan layers were characterized by coating a 1 x 1 cm 3D printed chip with chitosan using white light interferometry and a Filmetrics Profilm3D profilometer equipped with a 20X Mirau objective and Profilm software. Antibody (Ab_1) coverage on the flat 3D printed chip was estimated using the bicinchoninic acid (BCA) total protein assay. [63] Chitosan chips were incubated with 100 µL 3% glutaraldehyde, washed and incubated with 100 µL of 10 µg/mL anti-PSA antibodies overnight. Chips were then washed with PBS-T20 and incubated with 100 µL of BCA reagent (Thermo Fisher®) at 37˚ C for 2 hrs. Reagent was then transferred to a microplate where absorbance was measured at 562 nm. The absorbance was then used to estimate total amount of antibodies on the chip from a calibration curve for standard anti-PSA.

Colorimetric assay. Tips decorated with Ab_1 were filled with 50 µL standard protein or sample solution and incubated 30 min. Tips were then washed 3X with PBS-T20, 50 µL of biotinylated detection antibody (Ab_2) solution in 1% casein in PBS solution were pipetted in and incubated 20 min. Unbound Ab_2 were removed by washing 3X with PBS-T20, tips were filled with 50 µL streptavidin horseradish peroxidase (ST-HRP) diluted according to vendor specifications in 1% BSA in PBS and incubated 15 min. Tips were washed 3X with PBS-T20 and filled with 50 µL of TMB reagent prepared by mixing equal volumes of TMB substrate and

peroxide solution according to vendor specifications and incubated 12 min. Finally, solutions with developed color were transferred from tips into a 96 well microplate and filled with 50 μL of 2N sulfuric acid stop solution, and absorbance at 450 nm was measured using a microplate reader (Fig. 3.2C).

Chemiluminescence (CL) assay. Procedures were the same as for colorimetry except for the CL development and detection. Supersignal® West Femto reagent was used to develop CL that was recorded with a CCD camera in a dark box. Tips with sandwich immunocomplex decorated with HRP were filled with luminol reagent prepared by mixing equal volumes of luminol/enhancer substrate and hydrogen peroxide solution according to vendor specifications. Tips with CL reagent were then immediately placed into the dark box and images captured over 120 s (Fig. 3.2C). Images were analyzed using GeneTools® software (Syngene) to convert to relative CL intensity.

Cell phone-assisted image capture. Using colorimetric assay procedure, images of the developed blue color after incubation of TMB in each tip were captured using an Android cell phone camera with 12 megapixels resolution. Images of each tip were analyzed individually using free mobile app ColorGrap® from Loomatix available for both android cell phones and iPhones. ColorGrap uses image digitizer software to convert color intensity into a set of numbers based on the color composition and intensity of the specific image (Fig. 3.2C). K% values from analysis of each captured image were used to describe the intensity of the blue color developed since it showed the best correlation with color development.

Assay Validation and patient samples analysis. Assays were validated by measuring recoveries of biomarker proteins in spiked human serum samples. 100X diluted sterile, filtered human serum from human male AB plasma (Sigma®) was spiked with different concentrations of protein biomarkers. Colorimetric, CL, or cell phone-assisted quantification of spiked

concentrations were done in triplicate and concentrations were calculated after subtracting the signal from diluted human serum control. In addition, 13 human samples (3 controls, 5 indolent prostate cancer patients and 5 aggressive prostate cancer patients) were analyzed for 3 prostate cancer biomarker proteins, PSA, IGF-1 and CD-14, using the colorimetric assay. Patient samples were diluted 10x in PBS buffer for analysis of PSA and IGF-1 and 100x for analysis of CD-14 in order to bring biomarkers into dynamic range of the assays. Diluted samples were incubated in pipette tips for 30 min, washed 3x with PBS-T20 followed by incubation with 50 µL optimized Ab_2 solution. The same procedure described for colorimetric assays was followed in patient sample analysis using same R&D ELISA kits for tip assay, electrochemical and microwell plate ELISA. The same patient samples dilutions were used for traditional micro-well plate ELISA. Assay results were well correlated with those obtained from micro-well ELISA and well-established electrochemical immunoassay developed in house and similar to a published procedure. [35,36]

3.5 References

([1]) Sato, S.; Murakami, A.; Kuwajima, A.; Takehara, K.; Mimori, T.; Kawakami, A.; Mishima, M.; Suda, T.; Seishima, M.; Fujimoto, M.; et al. Clinical Utility of an Enzyme-Linked Immunosorbent Assay for Detecting Anti-Melanoma Differentiation-Associated Gene 5 Autoantibodies. *PLOS ONE* **2016**, *11*, e0154285.

([2]) Gan, S. D.; Patel, K. R. Enzyme Immunoassay and Enzyme-Linked Immunosorbent Assay. *J. Invest. Dermatol.* **2013**, *133*, 1–3.

([3]) Lequin, R. M. Enzyme Immunoassay (EIA)/Enzyme-Linked Immunosorbent Assay (ELISA). *Clin. Chem.* **2005**, *51*, 2415–2418.

([4]) Miao, L.; Zhu, C.; Jiao, L.; Li, H.; Du, D.; Lin, Y.; Wei, Q. Smart Drug Delivery System-Inspired Enzyme-Linked Immunosorbent Assay Based on Fluorescence Resonance Energy Transfer and Allochroic Effect Induced Dual-Modal Colorimetric and Fluorescent Detection. *Anal. Chem.* **2018**, *90*, 1976–1982.

([5]) Chen, X.; Liang, Y.; Zhang, W.; Leng, Y.; Xiong, Y. A Colorimetric Immunoassay Based on Glucose Oxidase-Induced AuNP Aggregation for the Detection of Fumonisin B1. *Talanta* **2018**, *186*, 29–35.

([6]) Rissin, D. M.; Kan, C. W.; Campbell, T. G.; Howes, S. C.; Fournier, D. R.; Song, L.; Piech, T.; Patel, P. P.; Chang, L.; Rivnak, A. J.; et al. Single-Molecule Enzyme-Linked Immunosorbent Assay Detects Serum Proteins at Subfemtomolar Concentrations. *Nat. Biotechnol.* **2010**, *28*, 595–599.

([7]) Vidal, J. C.; Bertolín, J. R.; Ezquerra, A.; Hernández, S.; Castillo, J. R. Rapid Simultaneous Extraction and Magnetic Particle-Based Enzyme Immunoassay for the Parallel Determination of Ochratoxin A, Fumonisin B1 and Deoxynivalenol Mycotoxins in Cereal Samples. *Anal. Methods* **2017**, *9*, 3602–3611.

([8]) Liu, D.; Li, X.; Zhou, J.; Liu, S.; Tian, T.; Song, Y.; Zhu, Z.; Zhou, L.; Ji, T.; Yang, C. A Fully Integrated Distance Readout ELISA-Chip for Point-of-Care Testing with Sample-in-Answer-out Capability. *Biosens. Bioelectron.* **2017**, *96*, 332–338.

([9]) Berg, B.; Cortazar, B.; Tseng, D.; Ozkan, H.; Feng, S.; Wei, Q.; Chan, R. Y.-L.; Burbano, J.; Farooqui, Q.; Lewinski, M.; et al. Cellphone-Based Hand-Held Microplate Reader for Point-of-Care Testing of Enzyme-Linked Immunosorbent Assays. *ACS Nano* **2015**, *9*, 7857–7866.

([10]) Wang, L.-J.; Chang, Y.-C.; Sun, R.; Li, L. A Multichannel Smartphone Optical Biosensor for High-Throughput Point-of-Care Diagnostics. *Biosens. Bioelectron.* **2017**, *87*, 686–692.

([11]) Singh, H.; Shimojima, M.; Shiratori, T.; An, L. V.; Sugamata, M.; Yang, M. Application of 3D Printing Technology in Increasing the Diagnostic Performance of Enzyme-Linked Immunosorbent Assay (ELISA) for Infectious Diseases. *Sensors* **2015**, *15*, 16503–16515.

([12]) Tan, X.; Oo, M. K. K.; Gong, Y.; Li, Y.; Zhu, H.; Fan, X. Glass Capillary Based Microfluidic ELISA for Rapid Diagnostics. *Analyst* **2017**, *142*, 2378–2385.

([13]) Rusling, J; Kumar, C; Gutkind, J; Patel, V; Measurement of Biomarker Proteins for Point-of-Care Early Detection and Monitoring of Cancer, *Analyst* **2010**, 135, 2496–2511.

([14])Srinivas, P; Kramer, B;Srivastava, S; Trends in biomarker research for cancer detection. *Lancet Oncol*. **2001**, 2, 698-704.

([15]) http://www.quansysbio.com/multiplex/multiplex-assays/ Last accessed 01/18/2019.

([16]) Rissin, D. M.; Kan, C. W.; Campbell, T. G.; Howes, S. C.; Fournier, D. R.; Song, L.; Piech, T.; Patel, P. P.; Chang, L.; Rivnak, A. J.; et al. Single-Molecule Enzyme-Linked Immunosorbent Assay Detects Serum Proteins at Subfemtomolar Concentrations. *Nat. Biotechnol.* **2010**, *28*, 595–599.

([17]) Rissin, D. M.; Kan, C. W.; Song, L.; Rivnak, A. J.; Fishburn, M. W.; Shao, Q.; Piech, T.; Ferrell, E. P.; Meyer, R. E.; Campbell, T. G.; et al. Multiplexed Single Molecule Immunoassays. *Lab. Chip* **2013**, *13*, 2902–2911.

([18]) Jung, W.; Han, J.; Choi, J.-W.; Ahn, C. H. Point-of-Care Testing (POCT) Diagnostic Systems Using Microfluidic Lab-on-a-Chip Technologies. *Microelectron. Eng.* **2015**, *132*, 46–57.

([19]) Han, K. N.; Li, C. A.; Seong, G. H. Microfluidic Chips for Immunoassays. *Annu. Rev. Anal. Chem.* **2013**, *6*, 119–141.

([20]) Das, T.; Chakraborty, S. Perspective: Flicking with Flow: Can Microfluidics Revolutionize the Cancer Research? *Biomicrofluidics* **2013**, *7*.

([21]) Costantini, F.; Sberna, C.; Petrucci, G.; Manetti, C.; de Cesare, G.; Nascetti, A.; Caputo, D. Lab-on-Chip System Combining a Microfluidic-ELISA with an Array of Amorphous Silicon Photosensors for the Detection of Celiac Disease Epitopes. *Sens. Bio-Sens. Res.* **2015**, *6*, 51–58.

([22]) Yu, L.; Ming Li, C.; Liu, Y.; Gao, J.; Wang, W.; Gan, Y. Flow-through Functionalized PDMS Microfluidic Channels with Dextran Derivative for ELISAs. *Lab. Chip* **2009**, *9*, 1243–1247.

([23]) Aeinehvand, M. M.; Ibrahim, F.; Harun, S. W.; Djordjevic, I.; Hosseini, S.; Rothan, H. A.; Yusof, R.; Madou, M. J. Biosensing Enhancement of Dengue Virus Using Microballoon Mixers on Centrifugal Microfluidic Platforms. *Biosens. Bioelectron.* **2015**, *67*, 424–430.

([24]) Burger, R.; Amato, L.; Boisen, A. Detection Methods for Centrifugal Microfluidic Platforms. *Biosens. Bioelectron.* **2016**, *76*, 54–67.

([25]) Hoegger, D.; Morier, P.; Vollet, C.; Heini, D.; Reymond, F.; Rossier, J. S. Disposable Microfluidic ELISA for the Rapid Determination of Folic Acid Content in Food Products. *Anal. Bioanal. Chem.* **2007**, *387*, 267–275.

([26]) Wang, G.; Das, C.; Ledden, B.; Sun, Q.; Nguyen, C.; Kumar, S. Evaluation of Disposable Microfluidic Chip Design for Automated and Fast Immunoassays. *Biomicrofluidics* **2017**, *11* (1).

([27]) Weng, X.; Gaur, G.; Neethirajan, S. Rapid Detection of Food Allergens by Microfluidics ELISA-Based Optical Sensor. *Biosensors* **2016**, *6* (2).

([28]) Benjamin Ho, C. M.; Huan Ng, S.; Holden Li, K. H.; Yoon, Y.-J. 3D Printed Microfluidics for Biological Applications. *Lab. Chip* **2015**, *15*, 3627–3637.

([29]) He, Y.; Wu, Y.; Fu, J.; Gao, Q.; Qiu, J. Developments of 3D Printing Microfluidics and Applications in Chemistry and Biology: A Review. *Electroanalysis* **2016**, *28*, 1658–1678.

([30]) Waheed, S.; Cabot, J. M.; Macdonald, N. P.; Lewis, T.; Guijt, R. M.; Paull, B.; Breadmore, M. C. 3D Printed Microfluidic Devices: Enablers and Barriers. *Lab. Chip* **2016**, *16*, 1993–2013.

([31]) Yazdi, A. A.; Popma, A.; Wong, W.; Nguyen, T.; Pan, Y.; Xu, J. 3D Printing: An Emerging Tool for Novel Microfluidics and Lab-on-a-Chip Applications. *Microfluid. Nanofluidics* **2016**, *20*, 50.

([32]) Sharafeldin, M.; Jones, A.; Rusling, J. F. 3D-Printed Biosensor Arrays for Medical Diagnostics. *Micromachines* **2018**, *9*, 394.

([33]) G. Rackus, D.; H. Shamsi, M.; R. Wheeler, A. Electrochemistry, Biosensors and Microfluidics: A Convergence of Fields. *Chem. Soc. Rev.* **2015**, *44*, 5320–5340.

([34]) Sharafeldin, M.; Bishop, G. W.; Bhakta, S.; El-Sawy, A.; Suib, S. L.; Rusling, J. F. Fe_3O_4 Nanoparticles on Graphene Oxide Sheets for Isolation and Ultrasensitive Amperometric Detection of Cancer Biomarker Proteins. *Biosens. Bioelectron.* **2017**, *91*, 359–366.

([35]) Krause, C. E.; Otieno, B. A.; Bishop, G. W.; Phadke, G.; Choquette, L.; Lalla, R. V.; Peterson, D. E.; Rusling, J. F. Ultrasensitive Microfluidic Array for Serum pro-Inflammatory Cytokines and C-Reactive Protein to Assess Oral Mucositis Risk in Cancer Patients. *Anal. Bioanal. Chem.* **2015**, *407*, 7239–7243.

([36]) Otieno, B. A.; Krause, C. E.; Latus, A.; Chikkaveeraiah, B. V.; Faria, R. C.; Rusling, J. F. On-Line Protein Capture on Magnetic Beads for Ultrasensitive Microfluidic Immunoassays of Cancer Biomarkers. *Biosens. Bioelectron.* **2014**, *53*, 268–274.

([37]) Tang, C. K.; Vaze, A.; Shen, M.; Rusling, J. F. High-Throughput Electrochemical Microfluidic Immunoarray for Multiplexed Detection of Cancer Biomarker Proteins. *ACS Sens.* **2016**, *1*, 1036–1043.

([38]) Sánchez-Tirado, E.; Salvo, C.; González-Cortés, A.; Yáñez-Sedeño, P.; Langa, F.; Pingarrón, J. M. Electrochemical Immunosensor for Simultaneous Determination of Interleukin-1 Beta and Tumor Necrosis Factor Alpha in Serum and Saliva Using Dual Screen Printed Electrodes Modified with Functionalized Double–walled Carbon Nanotubes. *Anal. Chim. Acta* **2017**, *959*, 66–73.

([39]) Das, J.; Ivanov, I.; Montermini, L.; Rak, J.; Sargent, E. H.; Kelley, S. O. An Electrochemical Clamp Assay for Direct, Rapid Analysis of Circulating Nucleic Acids in Serum. *Nat. Chem.* **2015**, *7*, 569–575.

([40]) Malecka, K.; Stachyra, A.; Góra-Sochacka, A.; Sirko, A.; Zagórski-Ostoja, W.; Radecka, H.; Radecki, J. Electrochemical Genosensor Based on Disc and Screen Printed Gold Electrodes for Detection of Specific DNA and RNA Sequences Derived from Avian Influenza Virus H5N1. *Sens. Actuators B Chem.* **2016**, *224*, 290–297.

([41]) Conde, J.; Edelman, E. R.; Artzi, N. Target-Responsive DNA/RNA Nanomaterials for microRNA Sensing and Inhibition: The Jack-of-All-Trades in Cancer Nanotheranostics? *Adv. Drug Deliv. Rev.* **2015**, *81*, 169–183.

([42]) Schoukroun-Barnes, L. R.; Wagan, S.; White, R. J. Enhancing the Analytical Performance of Electrochemical RNA Aptamer-Based Sensors for Sensitive Detection of Aminoglycoside Antibiotics. *Anal. Chem.* **2014**, *86*, 1131–1137.

([43]) Somerson, J.; Plaxco, K. W. Electrochemical Aptamer-Based Sensors for Rapid Point-of-Use Monitoring of the Mycotoxin Ochratoxin A Directly in a Food Stream. *Molecules* **2018**, *23*, 912.

([44]) Kadimisetty, K.; Malla, S.; Bhalerao, K. S.; Mosa, I. M.; Bhakta, S.; Lee, N. H.; Rusling, J. F. Automated 3D-Printed Microfluidic Array for Rapid Nanomaterial-Enhanced Detection of Multiple Proteins. *Anal. Chem.* **2018**, *90*, 7569–7577.

([45]) Kadimisetty, K.; P. Spak, A.; S. Bhalerao, K.; Sharafeldin, M.; M. Mosa, I.; H. Lee, N.; F. Rusling, J. Automated 4-Sample Protein Immunoassays Using 3D-Printed Microfluidics. *Anal. Methods* **2018**, *10*, 4000–4006.

([46]) Tang, C; Vaze , A; Rusling, J; Automated 3D-Printed Unibody Immunoarray for Chemiluminescence Detection of Cancer Biomarker Proteins, *Lab-on-Chip*, **2017**, 91, 359–366.

([47]) Park, H.; Guo, X.; Temenoff, J. S.; Tabata, Y.; Caplan, A. I.; Kasper, F. K.; Mikos, A. G. Effect of Swelling Ratio of Injectable Hydrogel Composites on Chondrogenic Differentiation of Encapsulated Rabbit Marrow Mesenchymal Stem Cells In Vitro. *Biomacromolecules* **2009**, *10*, 541–546.

([48]) Yu, X.; Munge, B.; Patel, V.;., Jensen, G.; Bhirde, A.; Gong, J. D.;, Kim, S.-N., Gillespie, J.; Gutkind J. S.; Papadimitrakopoulos, F.; Rusling, J. F. Carbon Nanotube Amplification Strategies for Highly Sensitive Immunosensing of Cancer Biomarkers in Serum and Tissue, *J. Am. Chem. Soc*., **2006**, *128,* 11199-11205.

([49]) Shah, V. P.; Midha, K. K.; Findlay, J. W.; Hill, H. M.; Hulse, J. D.; McGilveray, I. J.; McKay, G.; Miller, K. J.; Patnaik, R. N.; Powell, M. L. Bioanalytical method validation. *Pharm. Res.* 2000, *17*, 1551-1557.

([50]) Prensner, J. R.; Rubin, M. A.; Wei, J. T.; Chinnaiyan, A. M. Beyond PSA: The Next Generation of Prostate Cancer Biomarkers. *Sci. Transl. Med.* **2012**, *4*, 127rv3.

([51]) Aguiar, B. B. de; Girardi, I.; Paskulin, D. D.; França, E. de; Dornelles, C.; Dias, F. S.; Bonorino, C.; Alho, C. S. CD14 Expression in the First 24h of Sepsis: Effect of −260C>T CD14 SNP. *Immunol. Invest.* **2008**, *37*, 752–769.

([52]) Svensson, J.; Carlzon, D.; Petzold, M.; Karlsson, M. K.; Ljunggren, Ö.; Tivesten, A.; Mellström, D.; Ohlsson, C. Both Low and High Serum IGF-I Levels Associate with Cancer Mortality in Older Men. *J. Clin. Endocrinol. Metab.* **2012**, *97*, 4623–4630.

([53]) Mcgill, R.; Tukey, J.; Larsen, W.; Variations of Box Plots, *The American Statistician* **1978,** *32*, 12-16.

([54]) Stenberg, M.; Nygren, H. Kinetics of Antigen-Antibody Reactions at Solid-Liquid Interfaces. *J. Immunol. Methods* **1988**, *113*, 3–15.

([55]) Nygren, H.; Werthen, M.; Stenberg, M. Kinetics of Antibody Binding to Solid-Phase-Immobilised Antigen: Effect of Diffusion Rate Limitation and Steric Interaction. *J. Immunol. Methods* **1987**, *101*, 63–71.

([56]) Malhotra, R.; Papadimitrakopoulos, F.; Rusling. J. F. Sequential Layer Analysis of Protein Immunosensors based on Single Wall Carbon Nanotube Forests, *Langmuir*, **2010**, *26*, 15050–15056

([57]) Esser, P. *Activity of Adsorbed Antibodies*; 11b; Application note; Thermo Scientific, 1997.

([58]) Butler, J. E.; Ni, L.; Brown, W. R.; Joshi, K. S.; Chang, J.; Rosenberg, B.; Voss, E. W. The Immunochemistry of Sandwich elisas—VI. Greater than 90% of Monoclonal and 75% of Polyclonal Anti-Fluorescyl Capture Antibodies (CAbs) Are Denatured by Passive Adsorption. *Mol. Immunol.* **1993**, *30*, 1165–1175.

([59]) Butler, J. E.; Ni, L.; Nessler, R.; Joshi, K. S.; Suter, M.; Rosenberg, B.; Chang, J.; Brown, W. R.; Cantarero, L. A. The Physical and Functional Behavior of Capture Antibodies Adsorbed on Polystyrene. *J. Immunol. Methods* **1992**, *150*, 77–90.

([60]) Isobe, N.; Lee, D.-S.; Kwon, Y.-J.; Kimura, S.; Kuga, S.; Wada, M.; Kim, U.-J. Immobilization of Protein on Cellulose Hydrogel. *Cellulose* **2011**, *18*, 1251.

([61]) Zangheri, M.; Cevenini, L.; Anfossi, L.; Baggiani, C.; Simoni, P.; Di Nardo, F.; Roda, A. A Simple and Compact Smartphone Accessory for Quantitative Chemiluminescence-Based Lateral Flow Immunoassay for Salivary Cortisol Detection. *Biosens. Bioelectron.* **2015**, *64*, 63–68.

([62]) Roda, A.; Michelini, E.; Cevenini, L.; Calabria, D.; Calabretta, M. M.; Simoni, P. Integrating Biochemiluminescence Detection on Smartphones: Mobile Chemistry Platform for Point-of-Need Analysis. *Anal. Chem.* **2014**, *86*, 7299–7304.

([63]) Smith, P. K.; Krohn, R. I.; Hermanson, G. T.; Mallia, A. K.; Gartner, F. H.; Provenzano, M. D.; Fujimoto, E. K.; Goeke, N. M.; Olson, B. J.; Klenk, D. C. Measurement of Protein Using Bicinchoninic Acid. *Anal. Biochem.* **1985**, *150*, 76–85.

Chapter Four

Cancer Metastasis Biomarker Detection at Single Cell Levels using a 3D-Printed Microfluidic Immunoarray

4.1 Abstract

A microarray device capable of lysing cells and quantifying biomarker proteins released was designed and 3D-printed. Cell samples were lysed on-chip using RIPA lysis buffer augmented with 2 s pulse of a 50 KHz cell disruptor. Detection of desmoglein 3 (DSG3), a metastatic biomarker for head and neck squamous cell carcinoma (HNSCC), at single cell levels in multiple oral cancer cell cultures was demonstrated. The chip was equipped with a lysis chamber containing lysis buffer and sonication probe and reagent compartments that deliver samples and reagents to detection chambers. A sandwich immunoassay protocol captures target analytes in specified detection chambers decorated with specific capture antibodies immobilized on a hydrogel 3D chitosan film. Analytes were labeled with biotinylated secondary antibodies, which then capture streptavidin poly[horse radish peroxidase] (Poly-HRP). Chemiluminescence was then generated by delivering enhanced luminol reagent including H_2O_2 and captured with a CCD camera. Analytes include DSG3, a biomarker protein that resides in HNSCC cells that invade lymph nodes in metastasis, vascular endothelial growth factor-C (VEGF-C) as a positive control overexpressed in HSNCC, and beta-tubulin (β-Tub) as a loading control to estimate the number of cells in each sample. Detection limits were 0.10 fg/mL for DSG3, 0.20 fg/mL for VEGF-C and 0.20 fg/mL for β-Tub. Dynamic ranges were 0.10 – 100 fg/mL for DSG3, 0.20 – 200 fg/mL for VEGF-C and 0.10 – 100 fg/mL for β-Tub. With reported detection limits we were able to quantify proteins from a single cell lysate. Strong correlation between results obtained from on-chip cell lysis and conventional lysis technique was observed.

4.2 Introduction

Ninety percent of all cancer deaths are caused by metastasis (spreading) of original tumors.[1] It is well established that early detection leads to improved survival of cancer patients,[2] which holds for metastasis as well.[3] In this paper, we present a new automated microfluidic immunoarray to enable rapid, ultrasensitive detection of metastasis biomarkers.

While the approach reported here is applicable to any cancer and virtually any type of tissue, we focus here on desmoglein 3 (DSG3) as a high quality membrane-bound diagnostic biomarker for lymph node metastasis in oral cancer, or head and neck squamous cell carcinoma (HNSCC).[4,5] We recently established membrane protein DSG3 as a biomarker for occult lymph node metastasis of HNSCC.[6] DSG3 is highly expressed in metastatic oral cancer cells that have invaded neck lymph nodes, but not found in non-invaded lymph nodes.[7] HNSCC is one of the ten most common cancers worldwide, and accounts for ~10,000 deaths/year in the USA, with a 57% five year survival rate for newly diagnosed patients.[8] Oral cancer has an unusually high tendency to metastasize due to an extensive neck lymphatic network nearby.[9-12] Incidence of occult lymph node metastasis ranges between 10 - 50%.[13-19]Thus, rapid, sensitive diagnosis of lymph node metastasis is essential for HNSCC prognosis and key for clinical staging and treatment decisions.[14,10,20,]

Diagnosis of neck lymph node metastasis in HNSCC patients is currently addressed by pathological tests.[21-23] The current histopathological hematoxylin-eosin (H&E)-immunohistochemistry (IHC) assay can detect lesions <0.2 mm in lymph nodes to assess metastatic oral cancer, [30b] but requires days and cannot be used for in-operative staging. Modern imaging tools,[24-26] and assays of circulating cancer cells[3] are not yet sensitive enough to detect very

early metastasis. Real time (RT)-PCR methods can detect metastasis, but is relatively expensive, requires a skilled technician, and lacks single cell sensitivity.[27-29] Pathological evaluation of lymph nodes remains the preferred option, despite many false negatives due to failure to detect lesions <0.2 mm.[30-32] In addition, high incidence of HNSCC metastasis dictates that most node-negative patients undergo elective neck dissection to fully remove lymph nodes for assessment, resulting in potentially debilitating post-surgical overtreatment in over half of HNSCC patients.[33,34] Thus, there is an urgent need for fast, accurate, and ultrasensitive in-operative detection of metastatic oral cancer.

Microfluidic sensors offer a fast and reliable platform for ultrasensitive automated multi-protein assays.[35] We used an amperometric microfluidic immunosensor previously to investigate DSG3 as an oral cancer biomarker for metastasis in lymph nodes.[6] Other microfluidic immunosensors using electrochemical, electrochemiluminescent (ECL), and chemiluminescent (CL) detection have been developed to measure multiple protein and peptide biomarkers for diagnostics.[36-39] Also, desktop 3D printing now offers a simple, low cost, tool for development and fabrication of high performance microfluidic arrays.[40-43]

In this paper, we describe a 3D printed microfluidic array for ultrasensitive CL detection of DSG3 at single cell levels. Intact cell samples are introduced into the device and are lysed by ultrasonic-assisted chemical lysis. Detection chambers were coated with a hydrogel chitosan film that swells into a 3D structure where capture antibodies were immobilized. This 3D structure of chitosan helped increase antibody surface coverage which in addition to using poly HRP and ultrasensitive femto-luminol reagent helped reaching ultra-high assay sensitivity (<1 fg/mL). For comprehensive assessment of the samples, vascular endothelial growth factor-C (VEGF-C), a biomarker for HNSCC expressed into blood,[44] was also detected in the assay as positive control,

and beta-tubulin (β-Tub) was measured as a marker of the number of lysed cells (Scheme 4.1). DSG3 was detected at the single cell level with limit of detection (LOD) 0.10 fg/mL and 0.25 relative CL unit (CLU)/ log(fg/mL) sensitivity. VEGF-C had LOD 0.10 fg/mL and sensitivity of 0.08 CLU/log (fg/mL) and β-Tub had a 0.20 fg/mL LOD and 0.05 CLU/log (fg/mL).

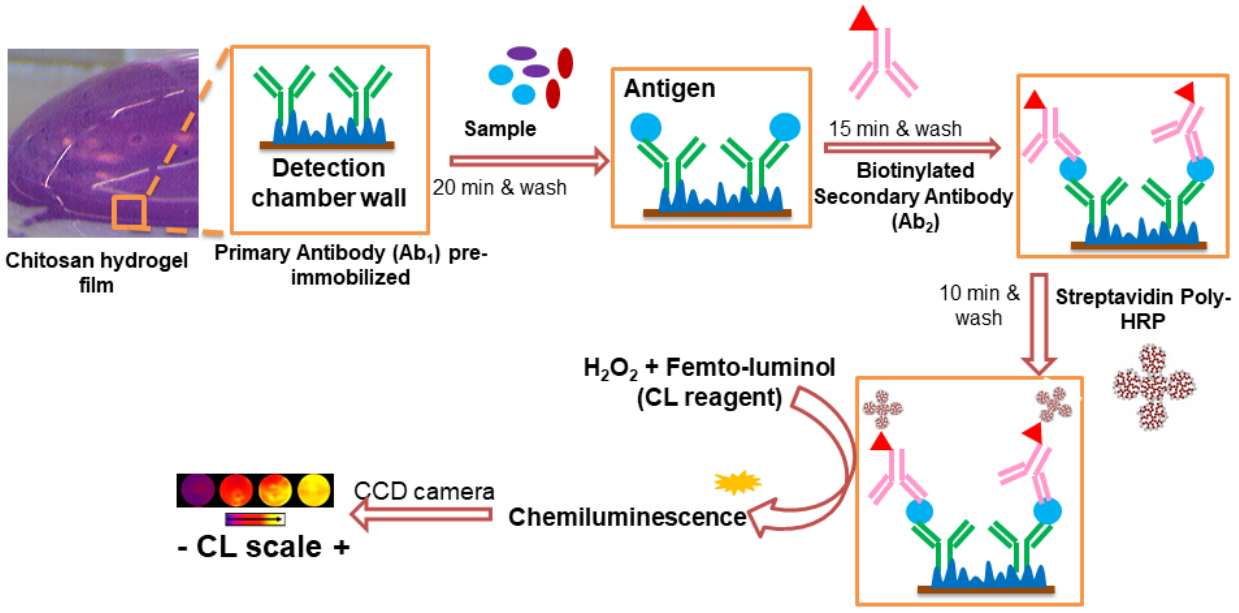

Scheme 4.1. Assay protocol and chemiluminescence signal generation using Femto-luminol reagent and re-colorized image of the signal captured using CCD camera

4.3 Materials and Methods

Materials. All reagents and chemicals were of analytical grade. Chitosan (low molecular weight) and glutaraldehyde were from Sigma Aldrich. Blocker casein in PBS buffer was from Thermo Fisher. ELISA kit for Vascular Endothelial Growth Factor-C (VEGF-C) (DY752B) was from R&D Systems. Human Desmoglein3 (DSG3) monoclonal antibody (MAB1720), human DSG3 biotinylated polyclonal antibody (BAF1720), recombinant human DSG3 chimera protein (1720-DM) and bovine serum albumin (BSA) were purchased from R&D Systems. Monoclonal [EP1331Y] beta-Tubulin antibody, biotinylated monoclonal [BT7R] beta-Tubulin antibody and recombinant human beta-Tubulin protein (ab70187) were from Abcam®. RIPA lysis buffer (50

mM Tris-HCl, pH 8.0, with 150 mM sodium chloride, 1.0% Igepal CA-630 (NP-40), 0.5% sodium deoxycholate, and 0.1% sodium dodecyl sulfate, and 2% Halt Protease and Phosphatase Inhibitor Single-Use Cocktail) was from Sigma Aldrich. Chemiluminescence (CL) was generated using Thermo Fisher Supersignal® West Femto chemiluminescent substrate, containing femto-luminol and hydrogen peroxide mixed immediately before use. Streptavidin-Poly(Horseradish Peroxidase) (Poly-HRP80) conjugate was obtained from Fitzgerald®. CL was measured using a Syngene® dark box with CCD camera. Images were processed using GeneSnap® software. Phosphate buffer saline (PBS) pH 7.4 was 0.01 M sodium phosphate in 0.14 M NaCl, 2.7 mM KCl and phosphate buffer saline-tween20 (PBS-T20) was 0.01 M sodium phosphate in 0.14 M NaCl, 2.7 mM KCl and 0.5% Tween-20. Cell lines CAL27 was from ATCC (Va), HN12, HN13 and HN30 were provided by Dr. Silvio Gutkind, University of California San Diego, and cultured Dulbecco's modified Eagle medium supplemented with 10% fetal bovine serum at 37°C in the presence of 5% CO2 as described previously.[45]

Microfluidic chip design. In order to reduce interaction between different reagents and samples before reaching the detection compartment, a five-inlet microfluidic chip design was adopted. The chip was equipped with five 80 μL chambers for sample, biotinylated antibodies, poly-HRP, CL reagent and wash buffer (PBS-T20) sequentially. An 8-chamber detection compartment for detection of the 3 selected biomarkers in duplicates and 2 chambers for BSA negative control each chamber volume capacity was 8 μL. The chip was connected to 5 programmable peristaltic micropumps (Takasago Fluidic Systems, RP-Q1.2N-P20Z) controlled by an Arduino® microcontroller (Fig. 4.1). The micropumps were housed in a 3D printed support that also accommodate an ultrasonic probe (Sonic Soak) placed directly under the sample chamber.

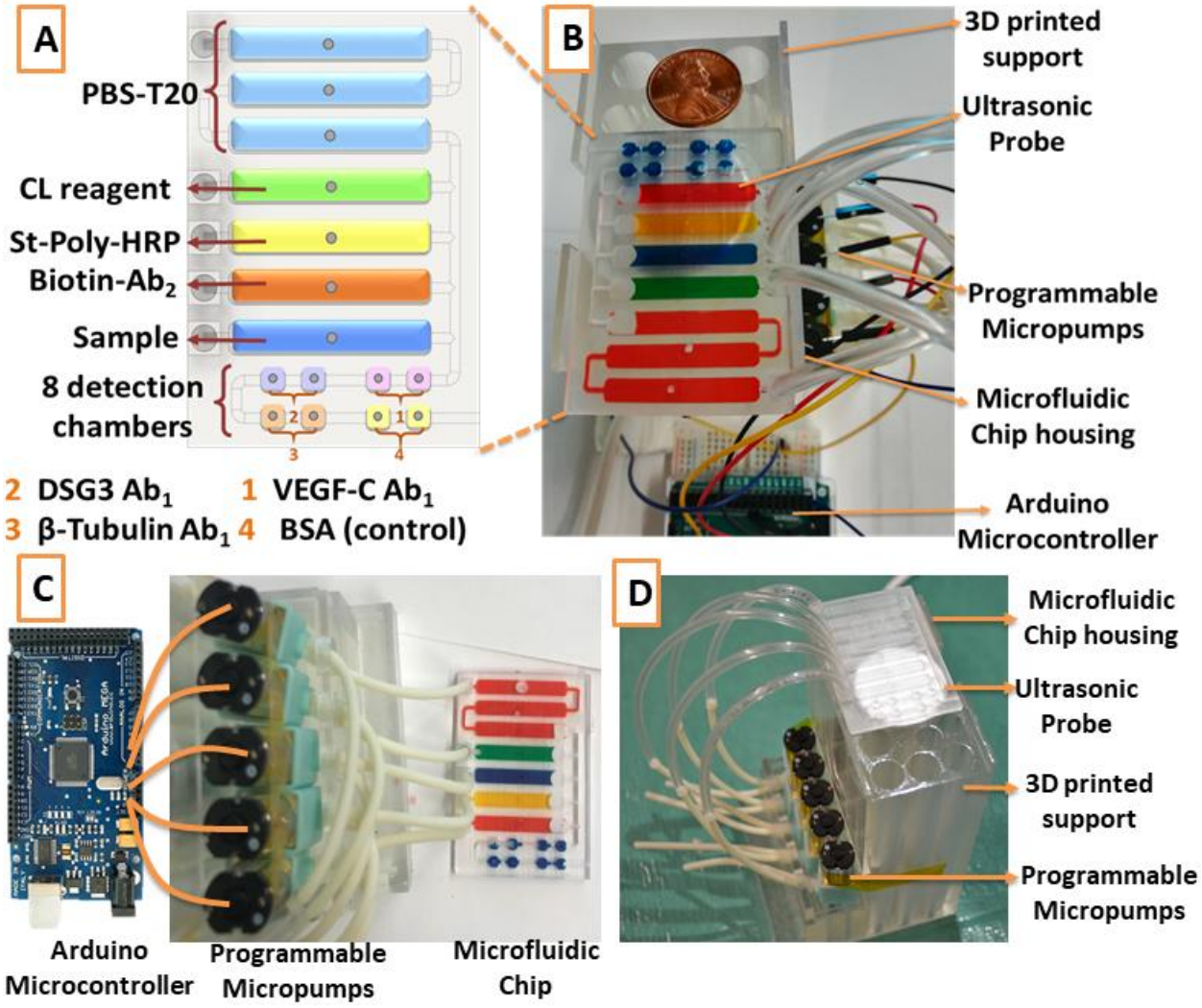

Fig. 4.1 Device design (A) Microfluidic chip design with 5 inlets connected to peristaltic micropumps, sample and reagent chambers with capacity of 80± 5 µL, and 8 detection chambers with 8±1 µL capacity each. (B) Microfluidic chip mounted on the support equipped with the sonication probe and connected to micropumps controlled by Arduino microcontroller. (C) programmable micropumps connected to microfluidic chip and controlled by an Arduino microcontroller. (D) 3D printed support with the microfluidic chip housing suiting the sample chamber right above ultrasonic probe, housing the peristaltic programmable micropumps and a reagent reservoir**.**

Antibody immobilization. Capture antibodies (Ab_1) were immobilized on the inner walls of each detection chamber using previously reported chitosan/glutaraldehyde chemistry.[46] Briefly, a thin film of chitosan on the inner walls of detection chambers was formed by adding 8 μL of 0.5 mg/mL chitosan in 0.05 M HCl (pH 4.0) into each detection chamber and were allowed to incubate for 3 hrs. Chitosan solution was drained out and the liquid film was dried under vacuum at RT overnight. 8 μL of 3% glutaraldehyde in PBS (pH 8.0) was added to detection chambers for 3 hrs, washed with DI water and 8 μL of capture antibodies at pre-optimized concentrations were added and incubated overnight. Unbound antibodies were washed with PBS-T20 and detection compartment was incubated with 1% casein blocker buffer for 1 hr. Detection compartment was washed with PBS-T20 and chips were stored at 4˚C until used.

Multiplexed biomarker chemiluminescence assay. 80 μL of standards with different concentrations of biomarker panel prepared in RIPA buffer/5% calf serum to mimic cell lysate surrogates were introduced into sample compartment. Samples were delivered to detection compartment by activating sample pump for 25s at a flow rate of 200 μL/min, incubated for 20 min, and washed by activating the PBS-T20 pump for 1 min a flow rate of 200 μL/min. Biotinylated detection antibodies (Ab2) were delivered to detection compartment by activating Ab2 pump for 20 s at 200 μL/min, incubated for 15 min and washed with 200 μL PBS-T20 by activating PBS-T20 pump for 1 min. Poly-HRP was flowed to detection compartment by activating HRP pump for 20s, incubated for 10 min, and washed with 200 μL of PBS-T20. Finally, femto luminol chemiluminescence reagent was delivered to detection compartment and Chemiluminescence signal was captured using a CCD camera for 15s.

Assay Validation. To assess the accuracy of assay, estimated concentration of each biomarker from spiked protein depleted cell lysates. Same chemiluminescence procedures were adapted to estimate concertation of each protein biomarker.

Cell culture. Cell cultures, HN12, HN13, HN30 and CAL27 were analyzed for the selected biomarker panel. Cells were cultured in DMEM supplemented with 10% fetal bovine serum (FBS) in presence of 5% CO_2 at 37˚C. Cells with culture medium were collected by mechanical separation of adherent cell layer from culture plates and number of cells per mL were estimated using manual cell counting.

Biomarker quantification form offline cell lysates. Offline cell lysis was used as standard method to prepare cell lysates that was introduced directly into the sample chamber and delivered right away to detection compartment. Cells were lysed by incubation with RIPA lysis buffer for 20 min with intermittent vertexing. Cell lysates originally estimated to have 1 x 10^6 cells/mL were diluted 10^5X before introducing 80 μL of lysate (~ 1 cell contents) into the sample chamber in order to bring biomarkers into the working concentration of the assay. Same chemiluminescence assay procedures were followed.

Biomarker quantification after online cell lysis. Collected cells with culture medium was diluted 10^4 times and 5 μL of the dilute cell solution was introduced into the sample chamber containing 75 μL of RIPA lysis buffer. Once introduced, the ultrasonic probe (50 KHz) was activated for 2s to mix the cells with the lysis buffer and augment the lysis process. Solution was kept in the sample compartment for 20 min, delivered to detection compartment and incubated for 20 min. Similar procedure were followed to quantify protein biomarkers using chemiluminescence procedures.

4.4 Results

Chitosan film characterization. Thin chitosan film formed on the inner wall of the detection chamber offer an expandable hydrogel layer allowing anchoring of massive numbers of Ab1. The 3D printed surface coated with chitosan has large peaks with different heights (5-33 μm) intercalated with approximately 10% valleys as shown in white light interferometry images (Fig. 2) The chitosan film after swelling had ~ 600% water of its total mass.[46] In addition, the volume of chitosan film increased approximately 1000% after swelling (Fig. 4.2). This huge increase in volume and mass with the surface roughness allowed the immobilization of approximately $1.0x10^{13}$ antibodies/cm^2.

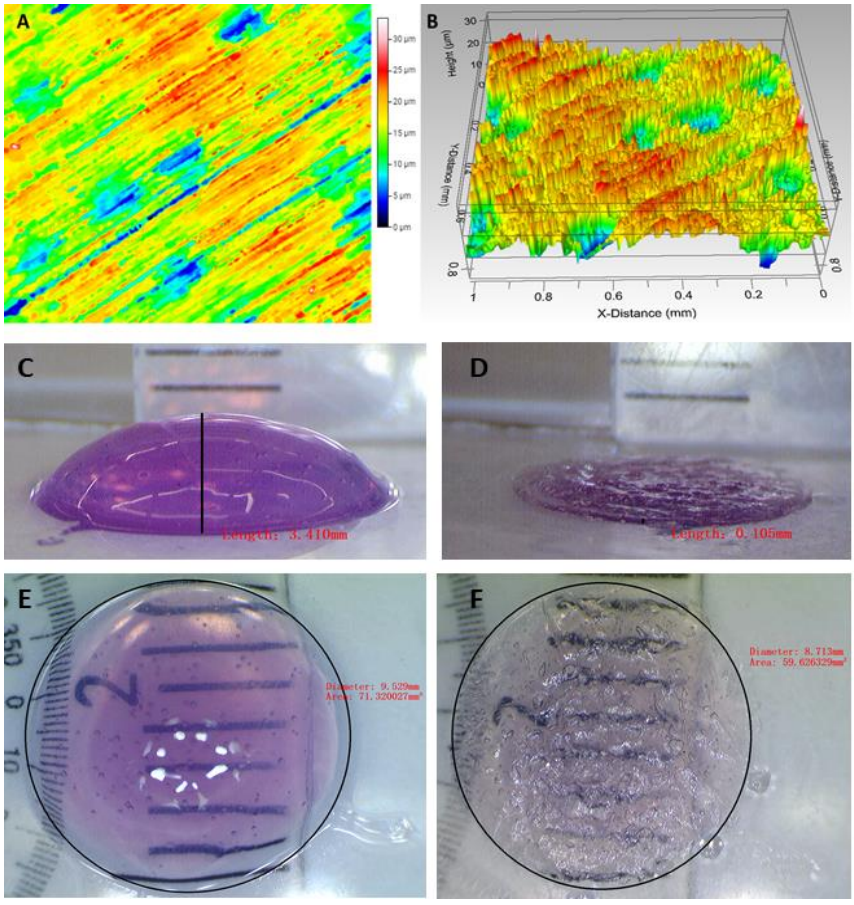

Fig. 4.2 White light interferometry surface profile of chitosan coated 3D printed chip (A) top view (B) Side view. Digital microscope images of side view of chitosan hydrogel hemisphere loaded with methylene blue dye (C) with water, (D) after drying. Digital microscope images of top view of chitosan hydrogel hemisphere loaded with methylene blue dye (E) with water, (F) after drying. Images show ~ 1000% increase in hemisphere volume after wetting with water.

Multiplexed biomarker assay. Capture and detection antibody concentrations along with incubation time of sample and detection antibodies in detection compartment were optimized for highest signal to noise ratio (Fig4.3-Fig. 4.6).

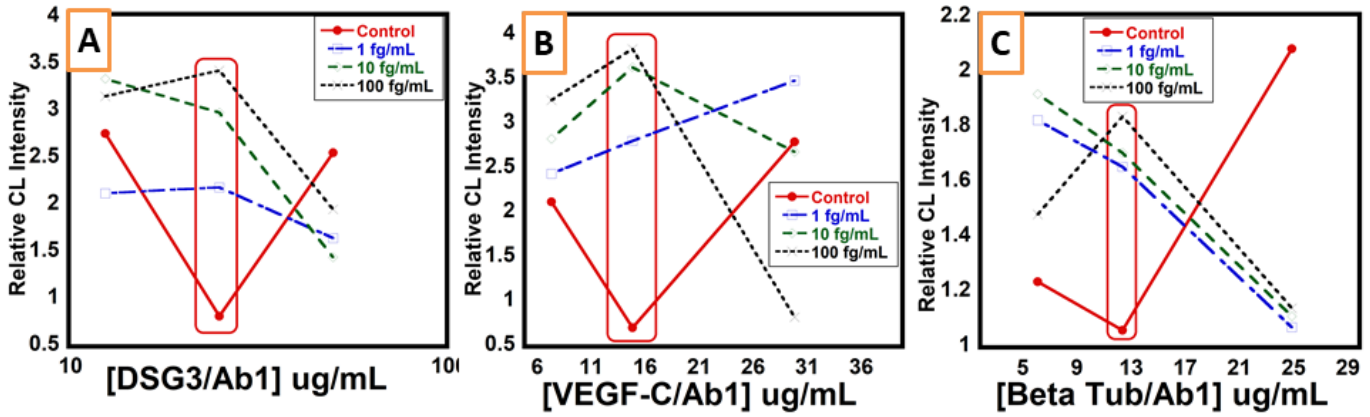

Fig. 4.3 Optimization of the immobilized capture antibody (Ab_1) concentration for (A) DSG3, (B) VEGF-C and (C) Beta Tub. Other experimental parameters were held constant while testing different Ab_1 concentrations. Signals were generated after flowing 100 µL west femto® luminol chemiluminescence substrate and images were captured for 15s using a CCD camera in dark box and relative intensity were calculated using GeneSnap® software

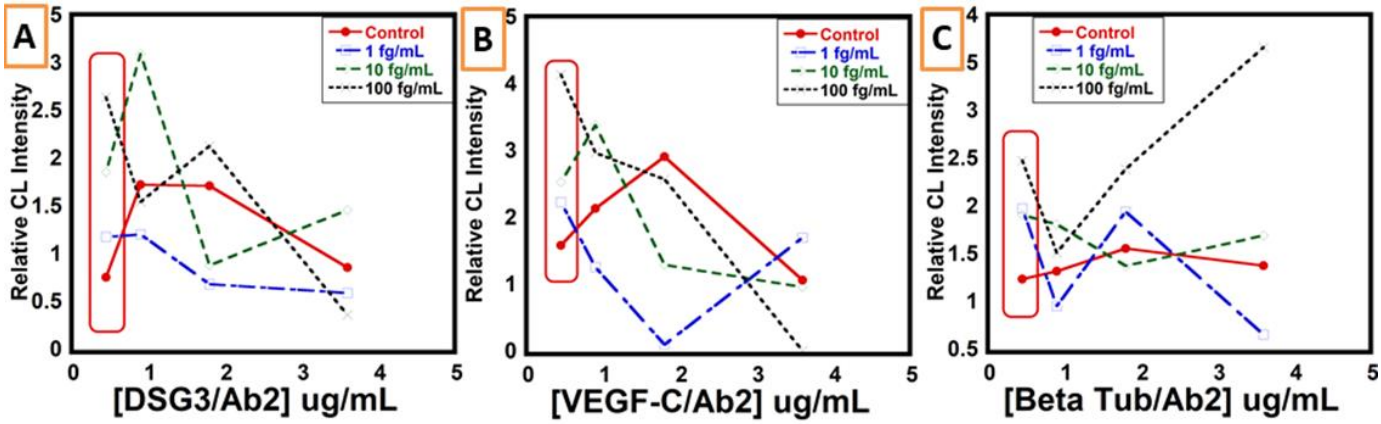

Fig. 4.4 Optimization of the immobilized detection antibody (Ab_2) concentration for (A) DSG3, (B) VEGF-C and (C) Beta Tub. Other experimental parameters were held constant while testing different Ab_1 concentrations. Signals were generated after flowing 100 µL west femto® luminol chemiluminescence substrate and images were captured for 15s using a CCD camera in dark box and relative intensity were calculated using GeneSnap® software

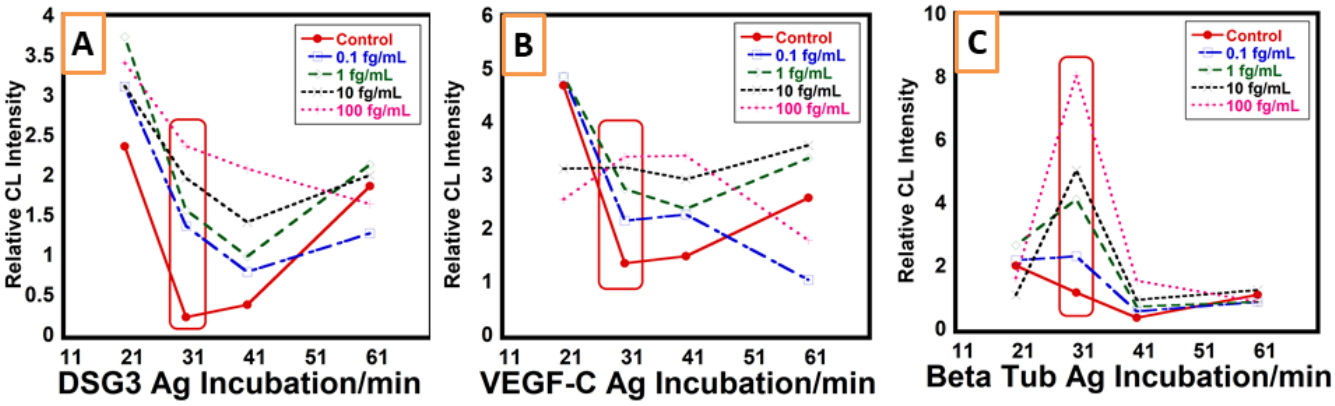

Fig. 4.5 Optimization of the incubation times for different antigens while stabilizing other experimental parameters (A) DSG3, (B) VEGF-C and (C) Beta Tub. Signals were generated after flowing 100 µL west femto® luminol chemiluminescence substrate and images were captured for 15s using a CCD camera in dark box and relative intensity were calculated using GeneSnap® software

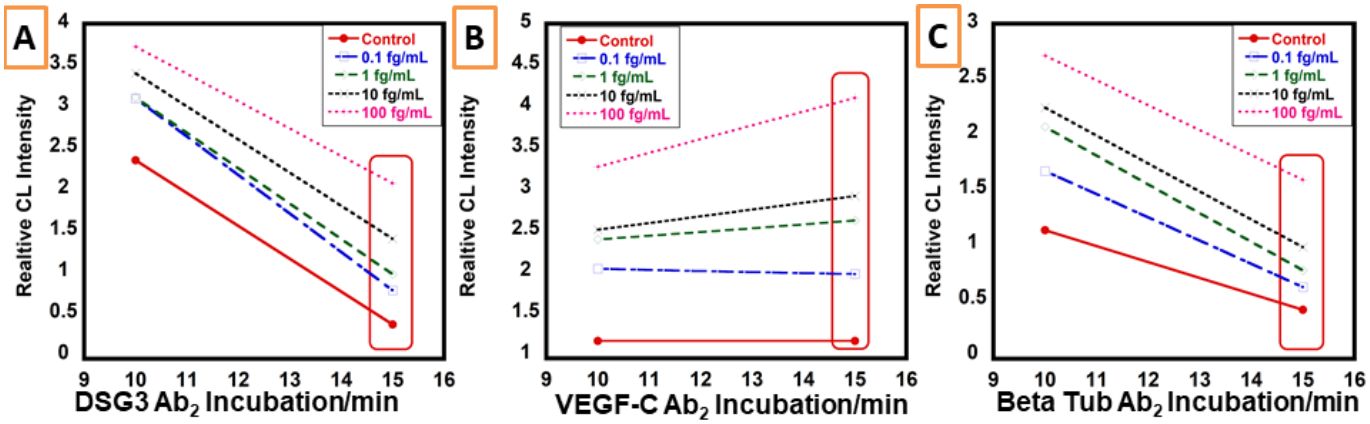

Fig. 4.6 Optimization of the incubation times for Ab_2 for (A) DSG3, (B) VEGF-C and (C) Beta Tub while stabilizing other experimental parameters. Signals were generated after flowing 100 µL west femto® luminol chemiluminescence substrate and images were captured for 15s using a CCD camera in dark box and relative intensity were calculated using GeneSnap® software

Preoptimized assay parameters were used to quantify the selected panel of biomarkers to assess the metastasis of HNC. Standards were prepared in RIPA lysis buffer spiked with 5x diluted calf serum to mimic the cell lysate matrix. Fig. 4.7 show the calibration curves for the selected biomarker proteins with standard deviations less than 20% for each concentration. Limit of

detections (LOD) were 0.10 fg/mL for DSG3, 0.20 fg/mL for VEGF-C and 0.20 fg/mL for β-Tub and dynamic ranges were 0.10-100 fg/mL for DSG3, 0.20-200 fg/mL for VEGF-C and 0.20-100 fg/mL for β-Tub. The ability to detect sub femtogram levels of DSG3 and VEGF-C promise single cell discovery in analyzed samples. DSG3 had expression levels of 90-250 fg/tumor cell which lies perfectly above the assay detection limit. Similarly, VEGF-C is secreted into the cell culture media and expressed in levels higher than 100 pg/mL which also perfectly fit the assay dynamic range after dilution.

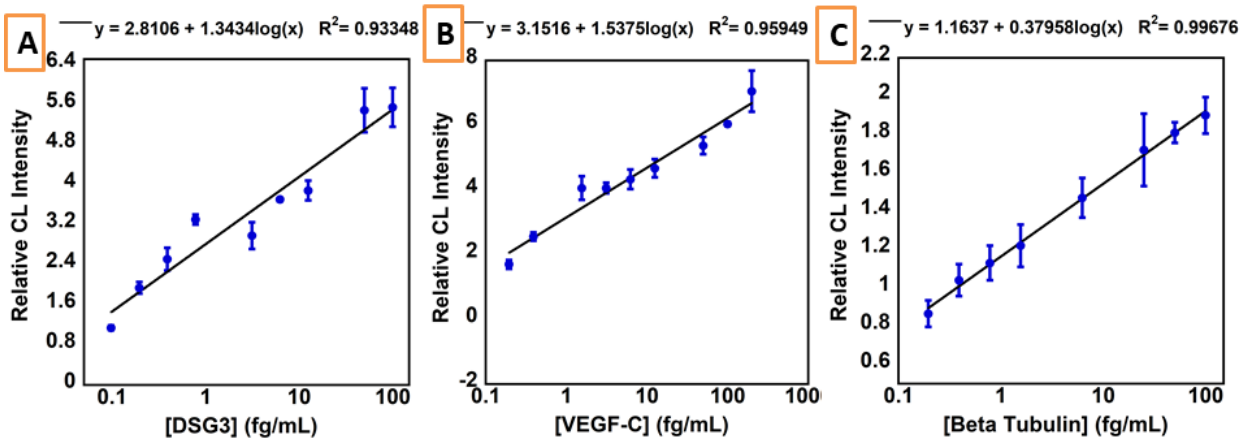

Fig. 4.7 Calibration curves obtained with the microfluidic microchip for (A) DSG3, (B) VEGF-C and (C) β-Tub. Cl signal was captured using a=CCD camera for 15 s. (n=4)

Effect of Sonication. To test the effect of sonication on the lysis efficiency, lysis step was performed in presence of lysis buffer without sonication and compared to applying 2s and 10s sonication. In addition, lysis step was also tested with PBS buffer (without the use of lysis buffer) in absence of sonication and with 2s and 10s sonication. In absence of sonication, both lysis buffer and PBS buffer samples showed concentration of VEGF-C (10±4.8 pg/mL) with negligible response for DSG3 and β-Tub. With 2s sonication in lysis buffer, DSG3 and β-Tub showed 50-150 fg/mL concentration with VEGF-C concentration of 11±3.2 pg/mL. PBS buffer with 2s sonication also had a relatively significant levels of both DSG3 and β-Tub (2-10 fg/mL) but still lower than same experiment with lysis buffer. With 10s sonication in lysis buffer there was no

noticeable change in both biomarkers' concentration compared to 2s sonication while 10s sonication in PBS buffer showed an increase in DSG-3 and β-Tub compared to 2s sonication (Fig. 4.8).

Fig. 4.8 Effect of sonication time on the extraction and quantitation of (A) DSG3, (B) VEGF-C, and (C) β-Tub in RIPA lysis buffer (blue line) and PBS buffer (Red dotted line) (n=4)

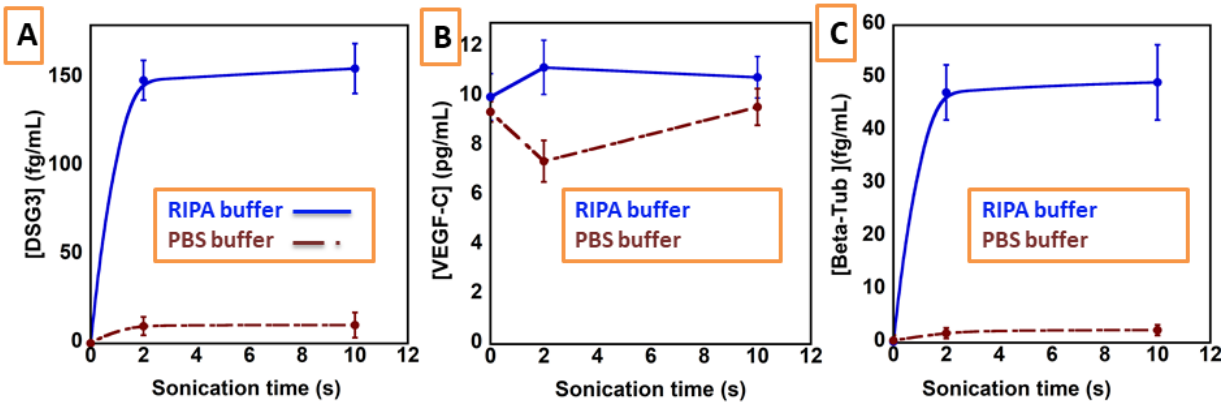

Assay validation. Selected concentrations of the biomarker panel were analyzed on the same day using different chips to estimate intra-day assay variation. Calculated relative standard deviations (RSD) were 11% for DSG3, 9% for VEGF-C and 14% for β-Tub. Similarly, assays were repeated over a span of five days to assess inter-day variation, RSD were 13% for DSG3, 12% for VEGF-C and 17% for β-Tub. In addition, recoveries of biomarkers panel from spiked protein depleted cell lysates were estimated to assess the accuracy of the assay. Percent recoveries after subtracting signals from controls varied between 80% and 120% indicating accuracy of the analytical technique (Table 4.1).[47]

Table 4.2. Spike-Recovery results for multiplexed biomarker proteins spiked in RIPA buffer with 5% human serum (n=4)

Biomarker protein	Spiked concentrations (fg/mL)	Found Concentrations* (fg/mL)	(%) recovery (±SD)
DSG3	12.5	11.8 (± 1.1)	94 (± 8)
	50	59 (± 4)	118 (± 8)
	100	111 (± 13)	111(± 13)
VEGF-C	10	8.7 (± 1.5)	87 (± 15)
	40	34 (± 4)	85 (± 10)
	80	92 (± 11)	115 (± 14)
B-Tub	15	13 (± 2)	87 (± 13)
	45	43 (± 4)	95 (± 8)
	90	101 (± 11)	112 (±12)
***after subtraction of the control RIPA lysis buffer with 5% calf serum**			

Comparison of online and offline cell lysis. 4 different cell lines were used to challenge the performance of the developed assay to lyse cells online and quantify target biomarker proteins in the lysates. HN12, HN13, HN30 and Cal27 cell lines were lysed offline using a previously reported lysis protocol and target analytes were quantified in their lysates using the microfluidic chip. Results obtained from online lysis of the same cell lines were obtained and compared to the offline lysis results. Strong correlation between results obtained from both techniques demonstrated the efficiency of the online cell lysis protocol. In addition, cell samples were lysed using offline lysis protocol and target protein biomarkers were quantified in lysates using ELISA. Good agreement

between results obtained by both techniques confirmed the accuracy of the developed microfluidic chip technology (Fig. 4.9).

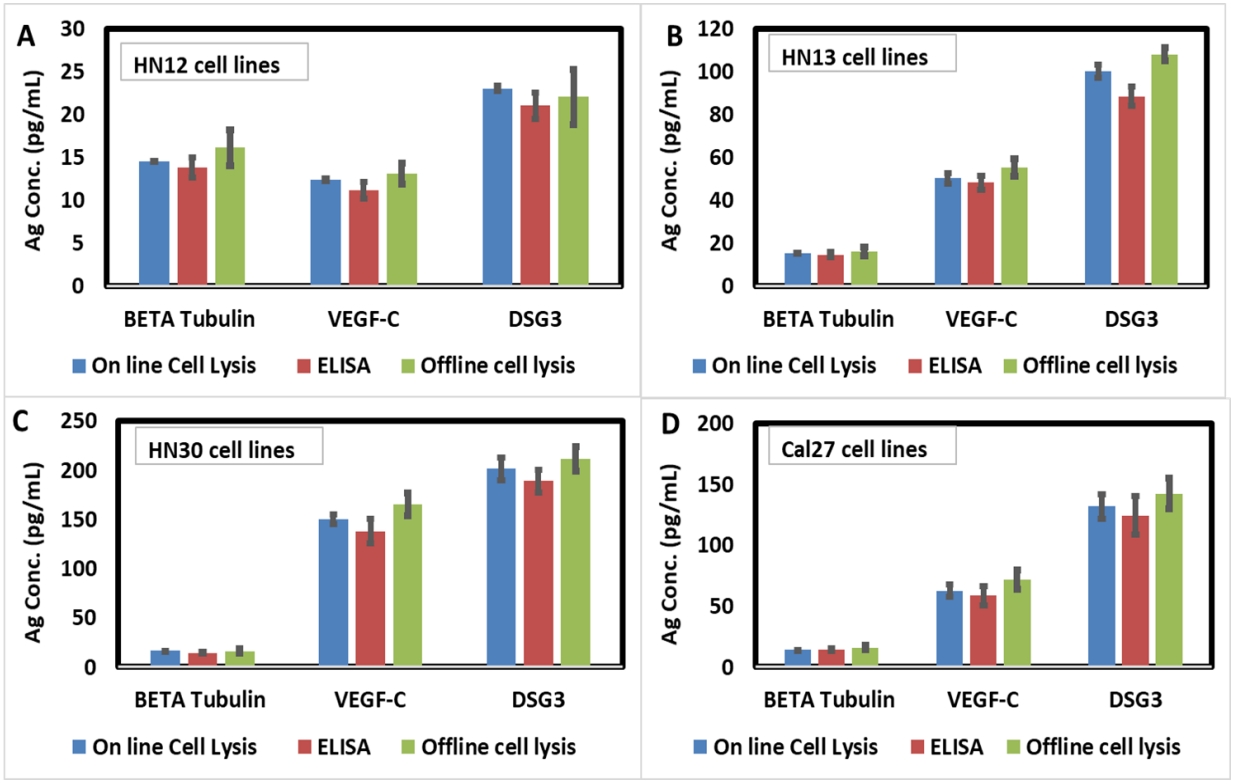

Fig. 4.9 Comparison of results obtained using online lysis, offline lysis and ELISA techniques for (A) HN12, (B) HN13, (C)HN30 and (D) CAL27 cell lines. (n=4)

Single Cell Analysis

In order to challenge assay sensitivity, cell cultures were diluted 1 million times to test the expression of the selected biomarker proteins in a single cell. 10 µL of the diluted samples (~Equivalent to single cell) were analyzed after an online lysis step and concentrations of the protein biomarkers were estimated. Due to cell-to cell variation and absence of cells in some diluted samples DSG3, VEGF-C and β-Tub expressions showed high degree of variation between runs for the same cell lines (Fig. 4.10)

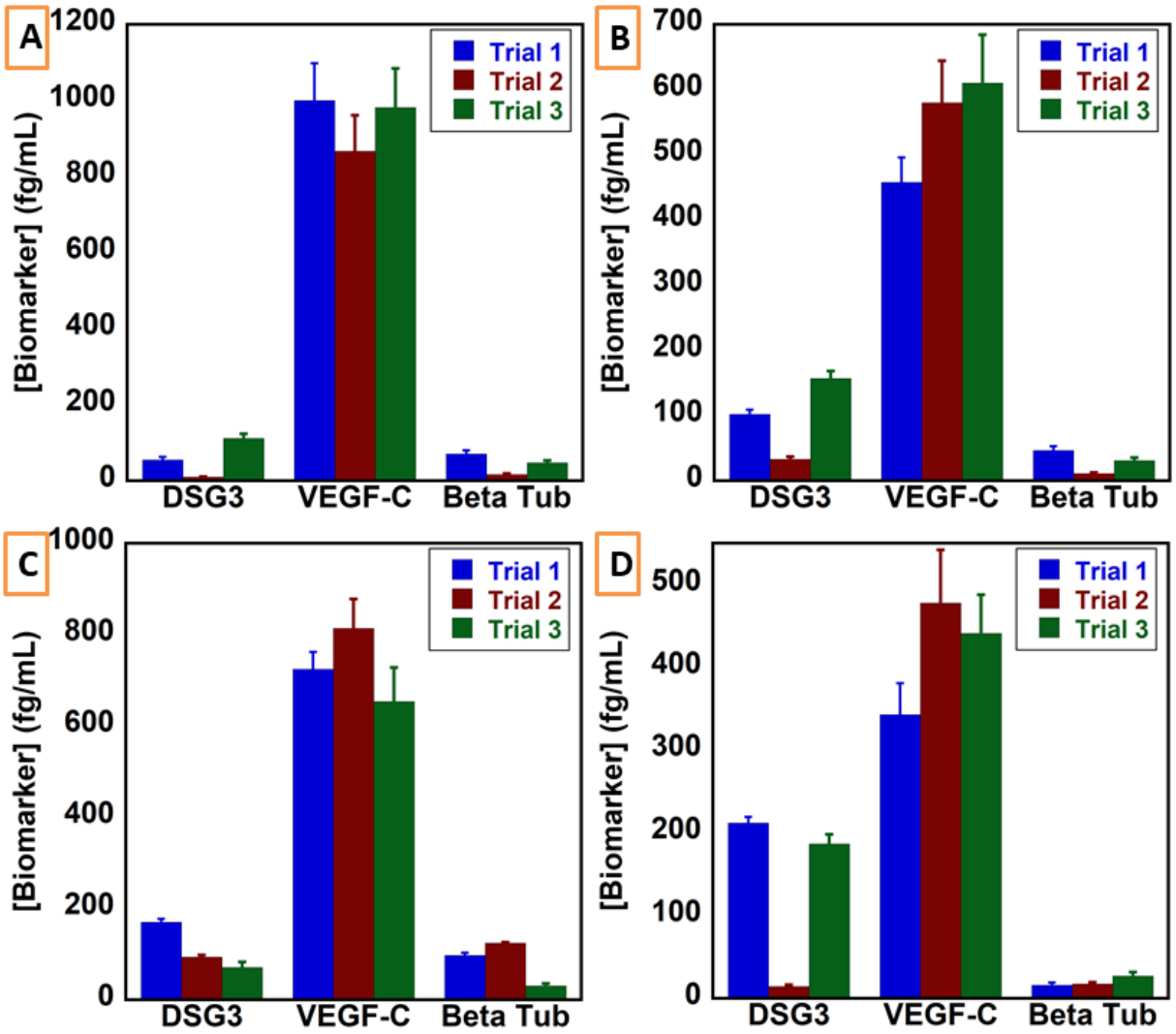

Fig. 4.10 Estimated biomarker concentration from single cell lysates for (A) HN12, (B) HN13, (C) HN30, and (d) CAL27 cell lines. 3 different samples were tested from each cell line (n=2) to study cell to cell variation.

4.5 Discussion

This work is the first report of online human cell lysis coupled to ultrasensitive detection of panel of biomarkers to accurately assess lymph node metastasis encountered in most of head and neck cancer patients. Cell lysis was achieved using chemical lysis augmented by short 2s pulse of 50 KHz ultrasonic wave. Ultrasonication was essential component since it helped mix the cells with RIPA lysis buffer after introducing cells into sample compartment. This approach allowed

fully automated system setup eliminating the need to mix the cell samples with lysis buffer before initiating the assy.

Biomarker panel was selected to fully assess the biopsy sample in order to get a full picture of the lymph node status before deciding upon dissection procedure. DSG3 was used as a positive biomarker exclusively expressed in invaded lymph nodes, and absent in non-invaded ones. The ability to detect sub-femtogram levels of DSG3 facilitated the discovery of as low as a single metastasized cell in the collected sample. VEGF-C has been previously reported to have strong correlation to state of head and neck cancer metastasis.[48,49] Combining both VEGF-C and DSG3 in the same assay would increase the significance of assay outcomes towards making an educated decision on the lymph node dissection.

This work also reported for the first time the use of β-Tub as a marker to estimate the number of cells in each sample analyzed in a ligand-binding assay format. β-Tub has been used as loading control for western blots but has not been explored in ligand-binging assay format.[50,5134,35] Ability to correlate found concentrations of each biomarker to the number of cells in the sample provide a more precise diagnostic significance.

The use of chitosan hydrogel to immobilize antibodies provided a 3D platform for antibody-antigen interaction improving the interaction kinetics which in turn was reflected in decrease in assay time and increased sensitivity. One component of this enhanced performance was the ability to immobilize approximately 2.0×10^{13} Ab/detection chamber. The other component was the expandable hydrogel nature of the chitosan layer that allowed the formation of water filled channels inside a 3D network that allowed better diffusion.

Excellent antibody surface coverage provided by chitosan hydrogel film improved the interaction kinetics between antigen flowed into detection compartment and antibodies on the chip surface. This improved kinetics was also supported by the microfluidic nature of the detection compartment with low volume/surface area ratio (10 μL/cm^2). This helped accelerate diffusion-controlled antigen-antibody interaction allowing reduction in assay time while maintaining ultra-sensitivity. In addition, the use of polymeric streptavidin multi-labelled with up to 400 HRP enzmes allowed the huge signal amplification has resulted in the sub femtogram LOD. Chemiluminescence signals has been generated using ultra-sensitive substrate (West Femto® Luminol) with its enhanced luminescence characteristics allowing bright images at very low antigen concentrations.

4.6 Conclusion

An ultra-sensitive detection strategy for biomarkers extracted from single cells was developed and validated. The technique depends on a physicochemical on-chip lysis protocol that adapt mixing cells with lysis buffer using 50 KHz ultrasonic waves for 2s. 3D printed microfluidic chip was designed to run assay automatically with reagents and samples delivered to detection compartment using peristaltic micro-pumps controlled by Arduino microcontroller. Detection compartment had 8 chambers that were massively coated with covalently immobilized capture antibodies on hydrogel chitosan film. Three protein biomarkers were tested in order to assess metastatic cancer cells in lymph nodes of Head and Neck Cancer (HNC) patients. Performance of the system was optimized to achieve sub-femtogram LOD of the selected biomarkers by applying signal amplification strategy using polymeric streptavidin Poly-HRP that resulted in LOD of 0.10 fg/mL for DSG3, 0.20 fg/mL for VEGF-C and 0.20 fg/mL for β-Tub.

4.7 References

[1] D. Spano, C. Heck, P. De Antonellis, G. Christofori, M. Zollo, Molecular networks that regulate cancer metastasis. *Seminars in Cancer Biol*. **2012**, 22, 234–249.

[2] (a) M. Kalinich, D. A. Haber, Cancer detection: Seeking signals in blood, *Science*, **2018**, 866-867; (b) Editorial: Early detection: a long road ahead, *Nature Rev. Cancer*, **2018,** 18, 401

[3] N. Gerges, J. Rak,, N. Jabado, New technologies for the detection of circulating tumour cells, *British Med. Bull*. 2010, 1–16 (April, 2010).

[4] Siriwardena, S. B. S. M.; Tsunematsu, T.; Qi, G.; Ishimaru, N.; Kudo, Y. Invasion-Related Factors as Potential Diagnostic and Therapeutic Targets in Oral Squamous Cell Carcinoma—A Review. *Int. J. Mol. Sci.* **2018**, *19* (5), 1462.

[5] Hoque Apu, E.; Akram, S. U.; Rissanen, J.; Wan, H.; Salo, T. Desmoglein 3 – Influence on Oral Carcinoma Cell Migration and Invasion. *Exp. Cell Res.* **2018**, *370* (2), 353–364.

[6] V. Patel, D. Martin, R. Malhotra, C. A. Marsh, C. L. Doçi, C. O. Nathan, U. K. Sinha, B. Singh, A. A. Molinolo, J. F. Rusling, J. S. Gutkind, Identification of DSG3 as a Biomarker for the Detection of Occult Metastasis in Sentinel Lymph Nodes in Oral Cancer Patients. *Oral Oncology*, **2013,** *49*, 93-101.

[7] V. Patel, B. L. Hood, A. A. Molinolo, et al. Proteomic analysis of laser-captured paraffin-embedded tissues: a molecular portrait of head and neck cancer progression. *Clin Cancer Res*. **2008**,14,1002-1014.

[8] J. Ferlay, H. R. Shin, F. Bray, D. Forman, C. Mathers, D. M. Parkin. Estimates of worldwide burden of cancer in 2008: GLOBOCAN 2008. *Int. J. Cancer*. **2010**, 127, 2893-917.

[9] C. R. Leemans, R. Tiwari, J. J. Nauta, I. van der Waal, G. B. Snow. Recurrence at the primary site in head and neck cancer and the significance of neck lymph node metastases as a prognostic factor. *Cancer*, **1994**, 73, 187-190.

[10] A. Forastiere, W. Koch, A. Trotti, D. Sidransky Head and neck cancer. *N. Engl. J. Med*. **2001**, 345,1890-1900.

[11] Marur, S.; Forastiere, A. A. Head and Neck Squamous Cell Carcinoma: Update on Epidemiology, Diagnosis, and Treatment. *Mayo Clin. Proc.* **2016**, *91* (3), 386–396.

[12] De Zinis, L. O. R.; Bolzoni, A.; Piazza, C.; Nicolai, P. Prevalence and Localization of Nodal Metastases in Squamous Cell Carcinoma of the Oral Cavity: Role and Extension of Neck Dissection. *Eur. Arch. Oto-Rhino-Laryngol. Head Neck* **2006**, *263* (12), 1131–1135.

[13] J. P. Shah, F. C, Candela, A. K. Poddar. The patterns of cervical lymph node metastases from squamous carcinoma of the oral cavity. *Cancer*, **1990**, 66, 109-113.

[14] M. A. Kuriakose, N. P. Trivedi. Sentinel node biopsy in head and neck squamous cell carcinoma. *Curr. Opin. Otolaryngology & Head and Neck Surgery*. **2009**, 17, 100-110.

[15] T. Mücke, D.A. Mitchell, S. Wagenpfeil, L. M. Ritschl1, K.-D. Wolff, A. Kanatas, Incidence and outcome for patients with occult lymph node involvement in T1 and T2 oral squamous cell carcinoma: a prospective study. *BMC Cancer* **2014**, 14,346-352.

[16] Research https://www.cancer.gov/types/head-and-neck/research (last accessed Jun 10, 2019).

[17] G. H. Head and neck squamous cell carcinoma https://ghr.nlm.nih.gov/condition/head-and-neck-squamous-cell-carcinoma (last accessed Jun 10, 2019).

[18] Koloutsos, G.; Vahtsevanos, K.; Kyrgidis, A.; Kechagias, N.; Triaridis, S.; Antoniades, K. Neck Dissection in Relation with Disease-Free, Disease-Specific, and Overall Survival of Patients with Squamous Cell Cancer of the Oral Cavity. *J. Craniofac. Surg.* **2014**, *25* (6), 1992–1997.

[19] Dogan, E.; Cetinayak, H. O.; Sarioglu, S.; Erdag, T. K.; Ikiz, A. O. Patterns of Cervical Lymph Node Metastases in Oral Tongue Squamous Cell Carcinoma: Implications for Elective and Therapeutic Neck Dissection. *J. Laryngol. Otol.* **2014**, *128* (3), 268–273.

[20] G. B. Snow, A. A. Annyas, E. A. van Slooten, H. Bartelink, A. A. Hart. Prognostic factors of neck node metastasis. *Clin Otolaryngol Allied Sci.* **1982**, 7,185-192.

[21] de Bondt, R. B. J.; Nelemans, P. J.; Hofman, P. A. M.; Casselman, J. W.; Kremer, B.; van Engelshoven, J. M. A.; Beets-Tan, R. G. H. Detection of Lymph Node Metastases in Head and Neck Cancer: A Meta-Analysis Comparing US, USgFNAC, CT and MR Imaging. *Eur. J. Radiol.* **2007**, *64* (2), 266–272.

[22] Alkureishi, L. W. T.; Burak, Z.; Alvarez, J. A.; Ballinger, J.; Bilde, A.; Britten, A. J.; Calabrese, L.; Chiesa, C.; Chiti, A.; de Bree, R.; et al. Joint Practice Guidelines for Radionuclide Lymphoscintigraphy for Sentinel Node Localization in Oral/Oropharyngeal Squamous Cell Carcinoma. *Ann. Surg. Oncol.* **2009**, *16* (11), 3190–3210.

[23]Don, D. M.; Calcaterra, T. C.; Anzai, Y.; Lufkin, R. B.; Fu, Y.-S. Evaluation of Cervical Lymph Node Metastases in Squamous Cell Carcinoma of the Head and Neck. *The Laryngoscope* **1995**, *105* (7), 669–674.

[24] (a) K. Kinkel. Y. Lu, M. Both, R. S. Warren, R. F. Thoeni, Detection of Hepatic Metastases from Cancers of the Gastrointestinal Tract by Using Noninvasive Imaging Methods (US, CT, MR Imaging, PET): A Meta-Analysis, *Radiology* **2002**, 224, 748–756, (b) D. Di Gioia, P. Stieber, G. P. Schmidt, D. Nagel, V. Heinemann and A. Baur-Melnyk, Early detection of metastatic disease in asymptomatic breast cancer patients with whole-body imaging and defined tumour marker increase, *Brit. J. Cancer*, **2015**, 112, 809–818

[25] Bree, R. de; Takes, R. P.; Castelijns, J. A.; Medina, J. E.; Stoeckli, S. J.; Mancuso, A. A.; Hunt, J. L.; Rodrigo, J. P.; Triantafyllou, A.; Teymoortash, A.; et al. Advances in Diagnostic Modalities to Detect Occult Lymph Node Metastases in Head and Neck Squamous Cell Carcinoma. *Head Neck* **2015**, *37* (12), 1829–1839.

[26] Chaturvedi, P.; Datta, S.; Arya, S.; Rangarajan, V.; Kane, S. V.; Nair, D.; Nair, S.; Chaukar, D. A.; Pai, P. S.; Pantvaidya, G.; et al. Prospective Study of Ultrasound-Guided Fine-Needle Aspiration Cytology and Sentinel Node Biopsy in the Staging of Clinically Negative T1 and T2 Oral Cancer. *Head Neck* **2015**, *37* (10), 1504–1508.

[27] R. L. Ferris, L. Xi, R. R. Seethala, J. Chan, S. Desai, B. Hoch, W. Gooding, T. E. Godfrey, Intraoperative qRT-PCR for Detection of Lymph Node Metastasis in Head and Neck Cancer, *Clin Cancer Res.*, **2011**, 17, 1858-1866.

[28] J. Solassol, V. Burcia, V .Costes, Pemphigus vulgaris antigen mRNA quantification for the staging of sentinel lymph nodes in head and neck cancer, *Brit. J. Cancer*, **2010**, 102, 181 – 187

[29] Ferris, R. L.; Xi, L.; Seethala, R. R.; Chan, J.; Desai, S.; Hoch, B.; Gooding, W.; Godfrey, T. E. Intraoperative QRT-PCR for Detection of Lymph Node Metastasis in Head and Neck Cancer. *Clin. Cancer Res.* **2011**, *17* (7), 1858–1866.

[30] (a) R. L. Ferris, Liqiang Xi, Siva Raja, Jennifer L. Hunt, Jun Wang, William E. Gooding, Lori Kelly, Jesus Ching, James D. Luketich, and Tony E. Godfrey, Molecular Staging of Cervical Lymph Nodes in Squamous Cell Carcinoma of the Head and Neck, *Cancer Res* **2005**, 65, 2174-2156. (b) C. H. Kim, R. A. Soslow, K. J. Park et al. Pathologic ultrastaging improves micrometastasis detection in sentinel lymph nodes during endometrial cancer staging. *Int J Gynecol Cancer*. 2013, 23, 964-70.

[31] R. L. Ferris, L. Xi, R. R. Seethala, J. Chan, S. Desai, B. Hoch, W. Gooding, T. E. Godfrey, Intraoperative qRT-PCR for Detection of Lymph Node Metastasis in Head and Neck Cancer, *Clin Cancer Res*., **2011**, 17, 1858-1866.

[32] (a) G. H. Lyman, A. E. Giuliano, M. R. Somerfield, et al. American Society of Clinical Oncology Guideline Recommendations for Sentinel Lymph Node Biopsy in Early-Stage Breast Cancer,*Clin. Oncol.* **2005**, 23, 7703-7720 (b) D. L. Weaver, Pathology evaluation of sentinel lymph nodes in Breast Cancer: protocol recommendations and rationale, *Mod. Pathol.* **2010**, *23*, S26–S32.

[33] Hamoir, M.; Schmitz, S.; Gregoire, V. The Role of Neck Dissection in Squamous Cell Carcinoma of the Head and Neck. *Curr. Treat. Options Oncol.* **2014**, *15* (4), 611–624.

[34] Lim, Y. C.; Koo, B. S.; Lee, J. S.; Choi, E. C. Level V Lymph Node Dissection in Oral and Oropharyngeal Carcinoma Patients with Clinically Node-Positive Neck: Is It Absolutely Necessary? *The Laryngoscope* **2006**, *116* (7), 1232–1235.

[35] Rusling, J. F. Multiplexed Electrochemical Protein Detection and Translation to Personalized Cancer Diagnostics. *Anal. Chem.* **2013**, *85* (11), 5304–5310.

[36] Malhotra, R.; Patel, V.; Chikkaveeraiah, B. V.; Munge, B. S.; Cheong, S. C.; Zain, R. B.; Abraham, M. T.; Dey, D. K.; Gutkind, J. S.; Rusling, J. F. Ultrasensitive Detection of Cancer Biomarkers in the Clinic by Use of a Nanostructured Microfluidic Array. *Anal. Chem.* **2012**, *84* (14), 6249–6255.

[37]. S. O. Kelley, C. A. Mirkin, D. R. Walt, R. F. Ismagilov, M. Toner, E. H. Sargent, Advancing the speed, sensitivity and accuracy of biomolecular detection using multi-length-scale engineering, *Nature Nanotech.* 2014, 9, 969-980.

[38] Dixit, C. K.; Kadimisetty, K.; Otieno, B. A.; Tang, C.; Malla, S.; Krause, C. E.; Rusling, J. F. Electrochemistry-Based Approaches to Low Cost, High Sensitivity, Automated, Multiplexed Protein Immunoassays for Cancer Diagnostics. *Analyst* **2016**, *141* (2), 536–547.

[39] Otieno, B. A.; Krause, C. E.; Jones, A. L.; Kremer, R. B.; Rusling, J. F. Cancer Diagnostics via Ultrasensitive Multiplexed Detection of Parathyroid Hormone-Related Peptides with a Microfluidic Immunoarray. *Anal. Chem.* **2016**, *88* (18), 9269–9275.

[40] Chi K. Tang, Abhay Vaze, James F. Rusling, Automated 3D-Printed Unibody Immunoarray for Chemiluminescence Detection of Cancer Biomarker Proteins, *Lab-on-Chip*, **2017**, 91, 359–366.

[41] Karteek Kadimisetty, Spundana Malla, Ketki S. Bhalerao, Islam M. Mosa, Snehasis Bhakta, Norman H. Lee, and James F. Rusling Automated 3D-Printed Microfluidic Array for Rapid Nanomaterial-enhanced Detection of Multiple Proteins, *Anal. Chem*., **2018,** *90*, 7569–7577.

[42] Rusling, J. F. Developing Microfluidic Sensing Devices Using 3D Printing. *ACS Sens.* **2018**, *3* (3), 522–526.

[43] Sharafeldin, M.; Jones, A.; Rusling, J. F. 3D-Printed Biosensor Arrays for Medical Diagnostics. *Micromachines* **2018**, *9* (8), 394.

[44]Fountzilas, G.; Angouridakis, N.; Wirtz, R. M.; Claas, S.; Nikolaou, A.; Kalogeras, K. T. Prognostic Value of VEGFC, HER2 and HER3 Gene Expression in Recurrent Squamous Cell Head and Neck Tumors. *J. Clin. Oncol.* **2006**, *24* (18_suppl), 5538–5538.

[45] Jeon, G. A.; Lee, J.-S.; Patel, V.; Gutkind, J. S.; Thorgeirsson, S. S.; Kim, E. C.; Chu, I.-S.; Amornphimoltham, P.; Park, M. H. Global Gene Expression Profiles of Human Head and Neck Squamous Carcinoma Cell Lines. *Int. J. Cancer* **2004**, *112* (2), 249–258.

[46] Sharafeldin, M.; Kadimisetty, K.; Bhalerao, K. R.; Bist, I.; Jones, A.; Chen, T.; Lee, N. H.; Rusling, J. F. Accessible Telemedicine Diagnostics with ELISA in a 3D Printed Pipette Tip. *Anal. Chem.* **2019**, *91* (11), 7394–7402.

[47] Shah, V. P.; Midha, K. K.; Findlay, J. W. A.; Hill, H. M.; Hulse, J. D.; McGilveray, I. J.; McKay, G.; Miller, K. J.; Patnaik, R. N.; Powell, M. L.; et al. Bioanalytical Method Validation—A Revisit with a Decade of Progress. *Pharm. Res.* **2000**, *17* (12), 1551–1557.

[48] Sousa, E. A. de; Lourenço, S. V.; Moraes, F. P. P. de; Vartanian, J. G.; Gonçalves–Filho, J.; Kowalski, L. P.; Soares, F. A.; Coutinho–Camillo, C. M. Head and Neck Squamous Cell Carcinoma Lymphatic Spread and Survival: Relevance of Vascular Endothelial Growth Factor Family for Tumor Evaluation. *Head Neck* **2015**, *37* (10), 1410–1416.

[49] Zhang, B.; Gao, Z.; Sun, M.; Li, H.; Fan, H.; Chen, D.; Zheng, J. Prognostic Significance of VEGF-C, Semaphorin 3F, and Neuropilin-2 Expression in Oral Squamous Cell Carcinomas and Their Relationship with Lymphangiogenesis. *J. Surg. Oncol.* **2015**, *111* (4), 382–388.

[50] Liu, N.-K.; Xu, X.-M. β-Tubulin Is a More Suitable Internal Control than β-Actin in Western Blot Analysis of Spinal Cord Tissues after Traumatic Injury. *J. Neurotrauma* **2006**, *23* (12), 1794–1801.

[51] Li, R.; Shen, Y. An Old Method Facing a New Challenge: Re-Visiting Housekeeping Proteins as Internal Reference Control for Neuroscience Research. *Life Sci.* **2013**, *92* (13), 747–751.

Chapter Five

Influence of Antibody Immobilization Strategy on Carbon Electrode Immunoarrays

5.1 Abstract

We report here the influence of antibody immobilization strategy on protein immunosensors on screen printed carbon electrode arrays in terms of antibody binding activity, analytical sensitivity, limit of detection, and stability. Horseradish peroxidase (HRP) was the model analyte with anti-HRP immobilized on the sensors, and HRP activity was used for detection. Covalently immobilized anti-HRP antibodies on electrodes coated with chitosan, electrochemically reduced graphene oxide (rGO), and dense gold nanoparticle (AuNP) films had only 20-30% of the total immobilized antibodies active for binding. Active antibodies increased to 60% with passively adsorbed antibodies on bare electrodes, to 85 % with oriented antibodies using protein A covalently immobilized on AuNP-coated carbon electrode, and to 98% when attached to protein A passively adsorbed onto bare electrodes. Passively adsorbed antibodies on bare electrodes lost activity in 1-2 days, but antibodies immobilized using other strategies remained relatively stable after 5 days. Covalent immobilization gave limits of detection (LOD) of 40 fg mL^{-1}, while passively adsorbed antibodies or protein A on carbon electrodes had LODs 4-8 fg mL^{-1}, but were unstable. Sensitivity was highest for antibodies covalently attached to AuNP electrodes (2.40 nA/log pg mL^{-1}) that also had highest antibody coverage, and decreased slightly when protein A on AuNP was used to orient antibodies. Passively adsorbed antibodies and oriented antibodies on protein A gave slightly lower sensitivities. Immobilization strategy or antibody orientation did not have a significant effect on LOD, but dynamic range increased as the number of active antibodies on sensor surfaces increased.

5.2 Introduction

Antibodies are major tools for ligand binding assays due to their ability to bind and target analytes in complex sample matrices with high selectivity and specificity.[1] Immobilization of antibodies on a solid surface or nanoparticle is often a crucial step for developing sensors for target analytes. Immunoassay format has been adapted to a wide spectrum of diagnostic tests including enzyme linked immunosorbent assay (ELISA),[2] protein microarrays,[3] lateral flow assay (LFA),[4] radioimmunoassay (RIA),[5] and electrochemical immunosensors.[6,7] Performance is predicted to depend on the method of antibody immobilization that can control surface coverage, correct orientation of antibodies to bind analytes, degree of nonspecific binding, and sensor shelf life.[8]

Electrochemical immunosensors are attractive due to inherent high sensitivity, simplicity of instrumentation, ease of integration into microfluidic systems, multiplexing capabilities, and possible upgrades to point-of-care (POC) devices.[9,10] Microfluidic electrochemical immunosensors have been developed to detect target analytes in environmental samples,[11] biological fluids,[12-14] and pharmaceutical preparations.[15] In electrochemical immunosensors, antibodies are immobilized onto sensor electrodes of materials including metals,[16, 17] conductive polymers [18] and different forms of carbon.[19] Carbon electrodes are available at low cost and give excellent performance in sensors due to a wide range potential window, low resistance, and low residual currents.[20-22] Screen printed electrodes have been widely used in sensor applications due to their relative low-cost mass production in single sensor or array format, and ease of design and miniaturization.[23]

For antibody attachment, sensor electrodes have been modified with functionalized nanomaterials via drop casting, inkjet [24] or manual [25] deposition, electrodeposition[26] and

electrospray sputtering.[27] Carbon nanotube forests were used on electrodes to immobilize increased amounts of antibodies on immunosensors resulting from high surface area of the nanostructured surface.[28]

Layer-by layer (LBL) assembly is a fast, facile technique for immobilizing polymers and nanomaterials on carbon electrodes. [29-31] Decorating carbon electrodes with a film of glutathione-coated gold nanoparticles (AuNP) is an effective antibody immobilization strategy to construct ultrasensitive immunosensors that also yields a large population of antibodies on a nanostructured surface.[32] Electrochemical deposition of graphene on electrodes from graphene oxide dispersions can also improve immunosensor performance.[33] Passive adsorption of antibodies on carbon electrode surface is another approach that can been utilized.[34, 35] Antibodies can also be oriented on electrodes through binding Fc region onto protein A letting Fab region free for antigen capture. Protein A is 42 KDa surface protein derived from Staphylococcus aureus bacteria and has five specific IgG binding domains.

In this paper, we compare six different antibody immobilization techniques on screen printed carbon electrodes, namely, attachment to glutathione-AuNP layers, electrochemical deposition of reduced graphene oxide (rGO), chitosan films, passive antibody adsorption, passively adsorbed protein A oriented antibody immobilization and covalent immobilization of protein A on AuNP electrodes (Scheme 5.1). We utilized anti-horseradish peroxidase (anti-HRP) as a model antibody to quantify horseradish peroxidase (HRP) in calf serum as a human serum surrogate. Amperometric current was measured at -0.3 V against Ag/AgCl upon addition of H_2O_2 to activate HRP and hydroquinone (HQ) as mediator.[28] Results were confirmed by measuring catalytic activity of captured HRP on sensor surfaces. Surface loading of antibody, sensitivity, limit of detection (LOD) and sensor shelf life were compared for the different immobilization strategies.

High sensitivity was achieved when large amounts of active antibodies were immobilized. A high degree of antibody orientation increased dynamic range, but was not a factor in LOD or sensitivity.

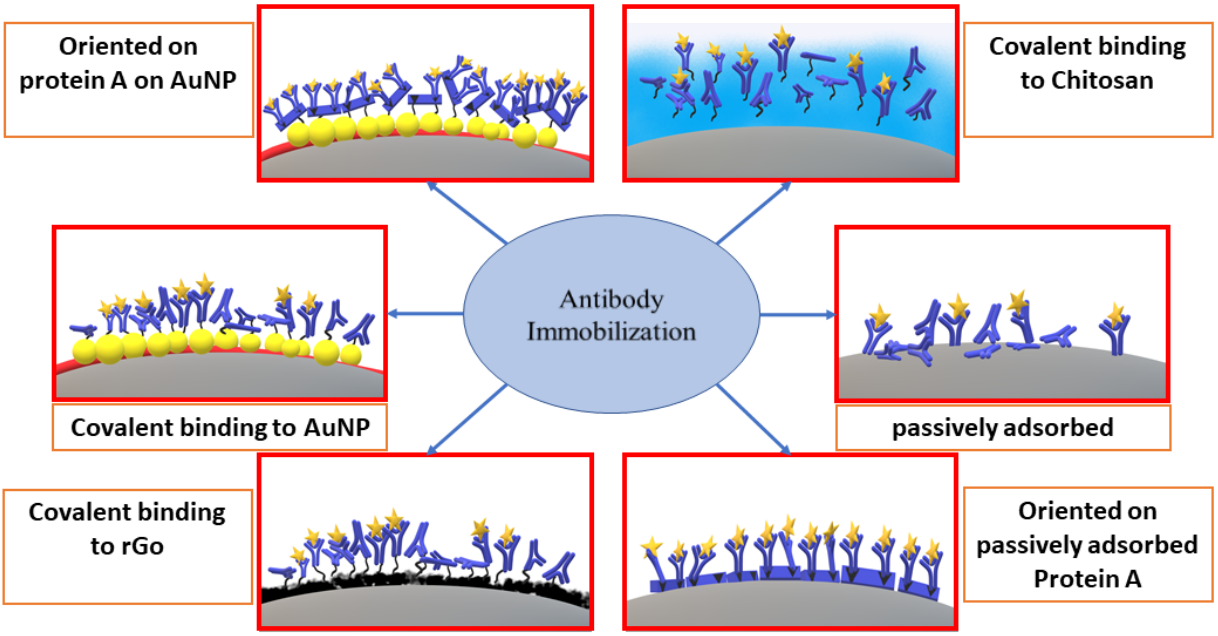

Scheme 5.2. Studied antibody immobilization techniques on screen printed carbon

5.3 Materials and methods

Materials. All chemicals were of analytical grade and nanopure water was prepared using a Hydro® Picosystem®. Screen printed carbon electrodes featuring eight electrodes were from Kanichi®. Gold (III) chloride trihydrate ($HAuCl_4$), N-(3-dimethylaminopropyl)-N′-ethylcarbodiimide hydrochloride (EDC), N-hydroxysulfosuccinimide sodium salt (NHSS), hydroquinone (HQ), hydrogen peroxide (30%), graphite powder (99%), potassium permanganate, poly(diallyldimethylammonium chloride) (PDDA, MW 100,00– 200,000, 20%) were from Sigma Aldrich®. Poly(dimethoxy)silane (PDMS) kit was from Dow Corning®. Phosphate buffer saline (PBS) pH 7.4 was 0.01 M sodium phosphate in 0.14 M NaCl, 2.7 mM KCl and phosphate buffer saline-tween20 (PBS-T20) was 0.01 M sodium phosphate in 0.14 M NaCl, 2.7 mM KCl and 0.5%

Tween-20. SIGMAFAST® O-phenylenediamine (OPD) tablets and horseradish peroxidase (HRP) were from Sigma Aldrich®. Anti-horseradish peroxidase mouse monoclonal antibody (Ani-HRP) [2H11] (ab10183) and recombinant protein A (ab52953) were from Abcam®.

Instrumentation: Microfluidic device incorporated a PDMS gasket with a flow channel in between two micromachined poly(methyl methacrylate) (PMMA) plates. The chamber is equipped with Pt counter electrode and Ag/AgCl reference electrode wires. A Kanichi® screen printed carbon electrode array featuring eight electrodes was inserted in the microfluidic chip under the PDMS flow channel. Amperometric measurements were done by applying -0.3V vs. Ag/AgCl using a multichannel CHI 1040 electrochemical workstation as reported previously in similar microfluidic arrays.,[29,36](Fig. 5.1) while flowing a mixture of 100 μM H_2O_2 in 1 mM HQ in PBS buffer.

Antibody concentration. A relatively high concentration of anti-HRP (100 μg/mL) was used in order to achieve maximum possible surface coverage in all tested strategies. Same concentration of antibodies was also used for different immobilization techniques to get a comprehensive comparison where the sensor performance will solely dependent on the immobilization technique and not the availability of antibodies.

Layer-by-layer (LBL) electrode modification. LBL film growth was used for anti-HRP immobilization using alternating layers of PDDA and glutathione-gold nanoparticles (AuNP). As reported previously.[32] Carboxylic acid groups on AuNP were activated by EDC/NHSS for 10 minutes, rinsed with DI water and dried with nitrogen. Anti-HRP at 100 μg mL^{-1} was spotted onto sensors, and arrays were left overnight at 4˚ C. Before use, arrays were washed with PBS-T20, incubated for 1 hour with 1% bovine serum albumin (BSA) in PBS buffer to reduce nonspecific binding.

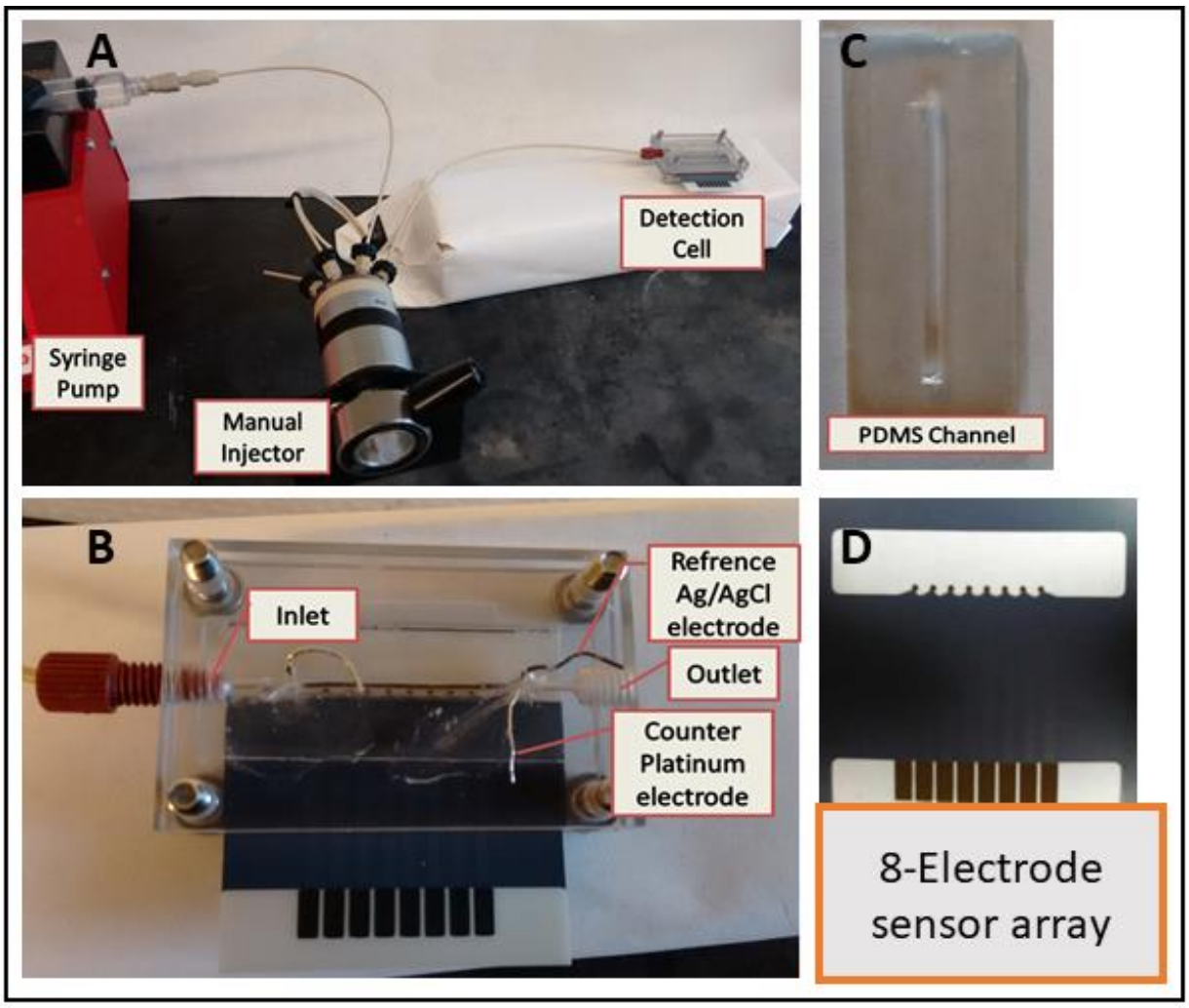

Fig. 5.1 Immunoassay system: (A) syringe pump, injector for samples and standards; (B) assembled detection chamber consisting of 2 machined PMMA plates, top plate holds symmetrically placed reference Ag/AgCl 0.6 mm diameter and 0.2 mm platinum counter electrode wires along the entire length of the 8-sensor array. Peek tubing is fitted to connect inlet and outlet; (C) PDMS channel 2.8 x 0.15 x 1.0 cm, volume 60 µL, placed above sensors; (D) Kanichi screen-printed carbon 8-sensor array alone.

Electrochemical deposition of graphene oxide (rGO). The array was immersed in 4 mg/mL graphene oxide (GO) solution prepared using modified Hummer's method [37] in 0.5 M lithium perchlorate. rGO was electrochemically deposited at -1.2 V vs. SCE for 60 s. Arrays were rinsed with water and dried with nitrogen. EDC-NHSS was used activate residual carboxylic groups on rGO for ten min, rinsed with water and dried with nitrogen, anti-HRP (100 µg mL^{-1}) was spotted

and arrays were left overnight at 4˚ C. Before use, arrays were washed with PBS-T20 and incubated with 1% BSA in PBS for 1 hr, and then rinsed with PBS-T20.

Antibody immobilization on chitosan. A thin film of chitosan was formed on sensor electrodes by spotting 0.25 mg mL^{-1} of chitosan in 0.05 M hydrochloric acid (pH 4.5). After 1 hr incubation, arrays were dried under vacuum, and amine groups of chitosan were activated by spotting 3% glutaraldehyde in PBS (pH 7.8), incubated for 2 hr, washed with water and dried using nitrogen. Anti-HRP (100 μg mL^{-1}) was spotted on the arrays and left overnight at 4˚ C, then rinsed with PBS-T20, incubated with 1% BSA for 1 hr and rinsed with PBS-T20 before use.

Passive adsorption of antibodies. 100 μg mL^{-1} of anti-HRP antibodies were adsorbed on sensors by incubating overnight at 4˚ C. Arrays were rinsed with PBS-T20, blocked with 1% BSA for 1 hr, and washed with PBS-T20 before use.

Passively adsorbed protein A oriented antibody immobilization. 25 μg mL^{-1} protein A were spotted on bare electrodes and allowed to incubate overnight at 4˚ C. Arrays were rinsed with PBS-T20 and incubated with 100 μg mL^{-1} anti-HRP for 3 hr, rinsed with PBS-T20, blocked with 1% BSA in PBS for 1 hr, and washed with PBS-T20 before use.

Covalent immobilization of protein A on AuNP electrode for oriented antibody immobilization. LBL strategy was utilized to decorate electrode surface with AuNP, that was activated by incubation with EDC/NHSS for 10 minutes. Protein A (25 μg mL^{-1}) was spotted and incubated on electrode surfaces overnight at 4˚C. Arrays were rinsed with PBS-T20, and incubated for 3 hr with 100 μg mL^{-1} anti-HRP, rinsed with PBS-T20, blocked with 1% BSA in PBS for 1 hr and washed with PBS-T20 before use

HRP assay. Arrays decorated with anti-HRP were inserted into the microfluidic chamber (Figure 5.1) where PBS buffer flowed at 100 μL min^{-1} flow rate using a syringe pump (New Era, NE-1000). 100 μL of standard or sample solution was loaded into the sample loop and injected using the sample injector (Rheodyne®, 9725i). Once the sample filled the microfluidic detection chamber, as determined by tests with dye solutions, flow was stopped and sample was incubated for 20 mins. Then, arrays were washed by flowing PBS-T20 for 3 min at 100 μL min^{-1}. Flow was switched from PBS-T20 to 1 μM HQ mediator in PBS and amperometry was done at -0.3 V vs. Ag/AgCl while injecting 100 μL of 100 μM H_2O_2 in 1 mM HQ/PBS.

Quantitation of antibodies immobilized on electrode surface. Bicinchoninic acid assay (BCA) was used to quantify the actual number of antibodies immobilized on the electrode surface [38]. Briefly, 100 μL micro BCA reagent kit (ThermoFisher® 23235) was prepared according to the vendor specification and incubated with 80 electrodes with immobilized antibodies at 37˚ C. BCA solution with the developed blue color was transferred to microplate and absorbance was measured at 562 nm. The concentration of immobilized anti-HRP was estimated utilizing a calibration graph constructed by running the same BCA procedures for series of standards of anti-HRP.

Quantitation of active antibodies: In order to estimate the number of active antibodies immobilized on electrodes, increasing concentrations of HRP were allowed to incubate for 20 minutes with electrodes and electrochemical oxidation catalyzed by HRP was measured. Hydroquinone was used as a mediator to shuttle electrons between electrode surface and enzyme distant from the electrode surface.[36] The use of mediator was essential to avoid variations of electrochemical signal resulting from varying distance between enzyme and electrode surface. Signal saturation was considered as the point where all active antibodies captured HRP molecules and further increase in HRP did not result in any increase in the signal. HRP concentration at the

saturation point was equivalent to the concentration of active antibodies immobilized on electrode surface.

HRP activity. Arrays decorated with anti-HRP captured HRP from solution using excess amount HRP (50 ng mL^{-1}) for 20 min. Each array was then washed with PBS-T20 and incubated with 100 μL of 4 mg mL^{-1} O-phenylenediamine (OPD) substrate in 0.05 M phosphate-citrate buffer (pH 5.0). OPD is converted to colored product (2,3–diaminophenazine) and the solution was transferred to a micro-well plate and absorbance measured at 492 nm after stopping reaction with 25 μL 3M HCL.[39] Concentration of HRP on electrodes was estimated using a calibration made with standard HRP solutions and the same protocol.

Inter-day assays. Electrodes were prepared, blocked, rinsed with PBS-T20 and stored in PBS buffer at 4˚ C for up to 5 days, the tested with 5 pg mL^{-1} HRP over 5 days. Results were used to estimate the loss of the immobilized antibody activity.

5.4 Results

Nominal electrode surface area and antibody coverage. Sensor surface area was estimated before and after surface modifications. Electrochemically active surface area of the bare electrode was estimated at 9.5±0.5 $x10^{-4}$ cm^2, using the slope of cyclic voltammogram (CV) peak currents vs. square root of the scan rate ($v^{1/2}$) for 0.5 mM ferrocene methanol (Fc-MeOH, D: diffusion coefficient of Fc-MeOH in TEAP = 7 X 10^{-6} cm^2 s^{-1})[40] in 0.1 M tetra-ethyl ammonium perchlorate (TEAP, Fig. 5.2).[41] Surface area after modification with rGO and was 2.1±0.1 $x10^{-3}$ cm^2, and for AuNP 2.4±0.2 x 10^{-3} cm^2, while chitosan electrodes had area 9.1±0.3 $x10^{-4}$ cm^2. Surface areas were used to compute the theoretical monolayer coverage of antibodies using antibody dimensions (14.5 x 8.5 x 4 nm^3),[42] and considering side-on or end-on orientation (Table 5.1).[43]

Protein A is a 42 kDa polypeptide with two functionally distinct halves, A C-terminal half for binding to cell walls and an N-terminal half for IgG binding. The protein binding portion is composed of five semi-identical, three-helix bundles, i. e. Ab-binding domains (E-D-A-B-C) that are interconnected with highly flexible linkers.[44] Average dimensions of protein A are 25-30 nm,[45] so theoretical maximum surface coverage of protein A was 1.2 x 10^8 – 1.5 x 10^8 on bare electrodes and 2.7 x 10^8 - 3.2 x 10^8 on AuNP electrodes. Although protein A has five antibody binding sites, actual binding of antibodies per protein A molecule is been estimated at 2.[46] Theoretical numbers of antibodies were also estimated for binding onto protein A on electrodes (Table 5.1).

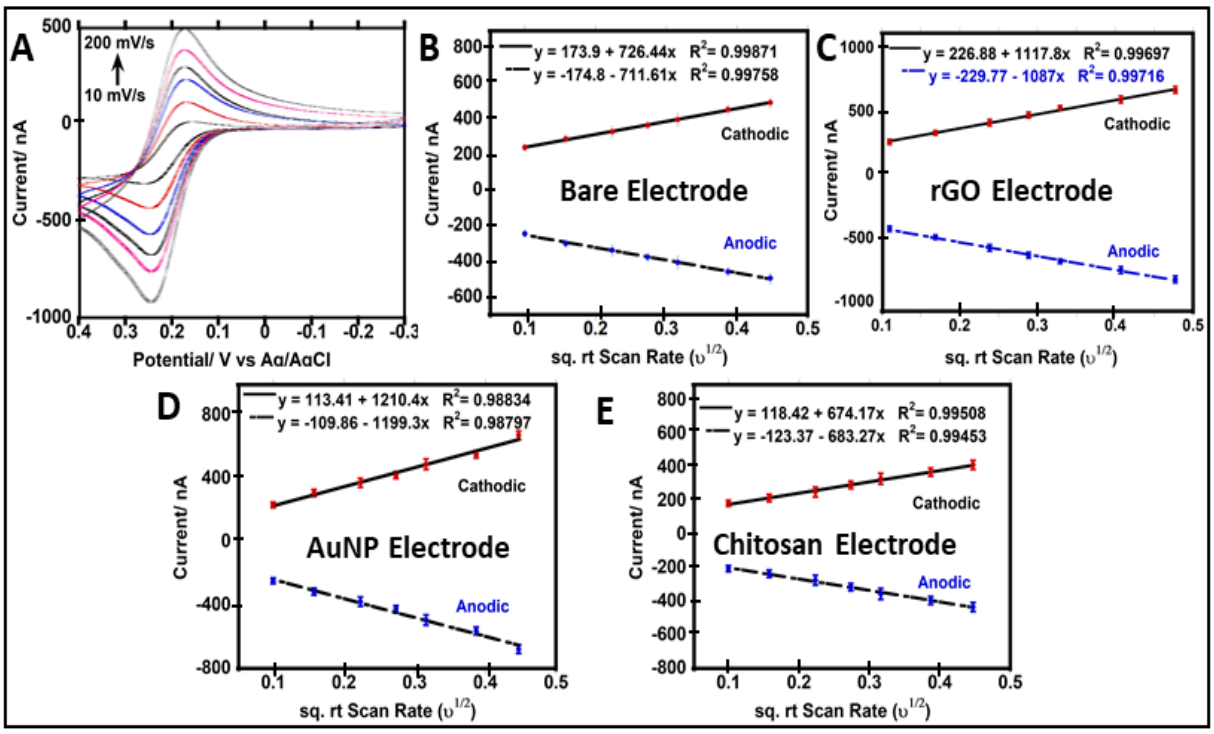

Fig. 5.2 Electrode surface area studies before and after electrode modifications using 0.5 mM Fc-MeOH in 0.1 M TEAP vs Ag/AgCl (0.14M NaCl); (A) Cyclic voltammograms at different scan rates (from 10 to 200 mV/s) for bare electrode; (B) peak current (I_p) vs. square root of the scan rate ($\nu^{1/2}$)for bare electrode; (C) I_p vs. $\nu^{1/2}$ for rGO coated electrode; (D) I_p vs. $\nu^{1/2}$ for AuNP electrode; (E) I_p vs. $\nu^{1/2}$ for chitosan electrode. (Error bars = standard deviation, n=8)

Actual antibody coverage. BCA assays were used to measure the actual number of bound antibodies on the electrode (Table 5.1). Surprisingly, chitosan electrodes had antibody coverage higher than the theoretically estimated coverage since it had 1.4±0.1 x 10^{-3} μg anti-HRP/electrode equivalent to 6.1±0.6 x 10^{9} anti-HRP/electrode, this was about 3 times higher coverage than the theoretical value, probably because of the 3 dimensional chitosan hydrogen forms with an area larger than that of the electrode.[47] Protein A immobilized on AuNP electrodes had approximately 10 times higher number of antibodies compared to the theoretical estimation based on calculated electrochemical active surface area of the modified electrodes, as flexible anchoring of protein A on a dense film of AuNP on electrode surface provided an excellent platform to covalently immobilize protein A that had the flexibility to bind to up to 6.1 ± 0.4 x 10^{9} anti-HRP/electrode. Passively adsorbed Protein A had a much smaller number of immobilized anti-HRP.

Table 5.3. Actual antibody coverage from BCA assay and theoretical estimated antibody coverage based on electrode surface area and antibody dimensions (standard deviation values indicated with n=2)

Immobilization Strategy	**Theoretical Coverage/electrode x 10^{9}**		**Coverage found x 10^{9}**
	(Side-on)	**(end-on)**	
AuNP/(EDC/NHSS)	1.90	7.10	6.2± 0.3
rGO/(EDC/NHSS)	1.70	6.20	4.3±0.3
Chitosan/Glutaraldehyde	0.73	2.40	6.1±0.6
Direct antibody Adsorption	0.76	2.70	1.1±0.03
Protein A (Passive Adsorption)	0.24	0.30	0.26±0.01
Protein A on AuNP electrodes	0.54	0.64	6.1±0.4

Active Antibodies. The saturation level of HRP signals in the arrays where signals level off, was used to estimate the number of active antibodies. Bulk HRP concentration at each saturation point was used to estimate the maximum number of HRP molecules that can interact with antibodies on electrode surface during incubation. Number of HRP molecules that would bind to antibodies immobilized on each electrode, from the volume of solution inside microfluidic chamber, was estimated using Einstein's diffusion equation (Eq. 1) assuming that binding is diffusion controlled.[48] For diffusion coefficient (D) of HRP 5 x 10^{-7} cm^2 s^{-1},[49] the distance travelled by HRP in 20 min incubation time is 0.012 mm.

$$d = \sqrt{(2\ D\ t)} \quad \text{..... (1)}$$

where d is distance in cm, D is the diffusion coefficient, and t is time in sec.

The solution containing HRP available to bind to anti-HRP immobilized on each electrode is a hemisphere of radius 0.012 mm with volume 7.24 x 10^{-6} µL (Fig. 5.3).

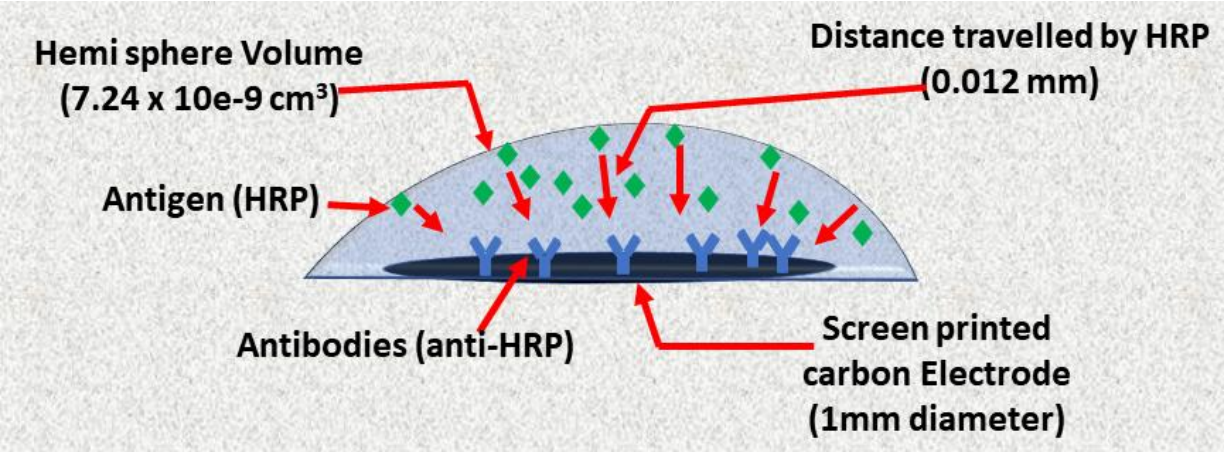

Fig. 5.3 Schematic illustration of the diffusion-controlled interaction between antigen and antibodies immobilized on electrode surface; maximum distance that can be travelled by antigen with diffusion coefficient of 5 x 10^{-7} cm^2/s in 20 min was estimated to be 0.012 mm. This result in a hemisphere with a volume of 7.24 x 10^{-6} µL.

The number of HRP molecules in this available volume of solution to bind anti-HRP was estimated from the saturation concentrations (Table 5.2 and Table 5.3). Amounts of actively binding antibodies were relatively low except for those using an initial layer of protein A, which had 85% active antibodies for AuNP electrodes and 98% on bare carbon (Fig. 5.4)

Active antibodies on each electrode was also measured using the HRP enzyme activity assay for oxidaton of O-phenylenediamine (OPD). Enzymes captured on sensor arrays were incubated with OPD for 1 hr and color developed was used to estimate the number of HRP molecules that correspond to the number of active anti-HRP. Calibration using soluble HRP with was used to esimate the concenterations of HRP on arrays (Fig. 5.5). Good agreement between results obtained from electrochemical and OPD assays was found (Table 5.2).

Table 5.4. Active antibodies/electrode using different immobilization strategies on screen printed carbon electrode estimated using electrochemical assay and OPD enzyme activity assay (standard deviation values indicated with n=16 for electrochemical measurements and n=3 for OPD assay).

Immobilization Strategy	**No. of Active antibodies/electrode x 10^9**	
	Electrochem. estimate	**OPD Assay**
AuNP/(EDC/NHSS)	2.56±0.20	2.94±0.11
rGO/(EDC/NHSS)	1.28±0.14	1.48±0.13
Chitosan/Glutaraldehyde	1.28±0.09	1.00±0.05
Direct antibody Adsorption	2.56±0.08	2.11±0.11
Protein A (Passive Adsorption)	0.26±0.01	0.23±0.01
Protein A on AuNP electrodes	5.13±0.36	5.86±0.41

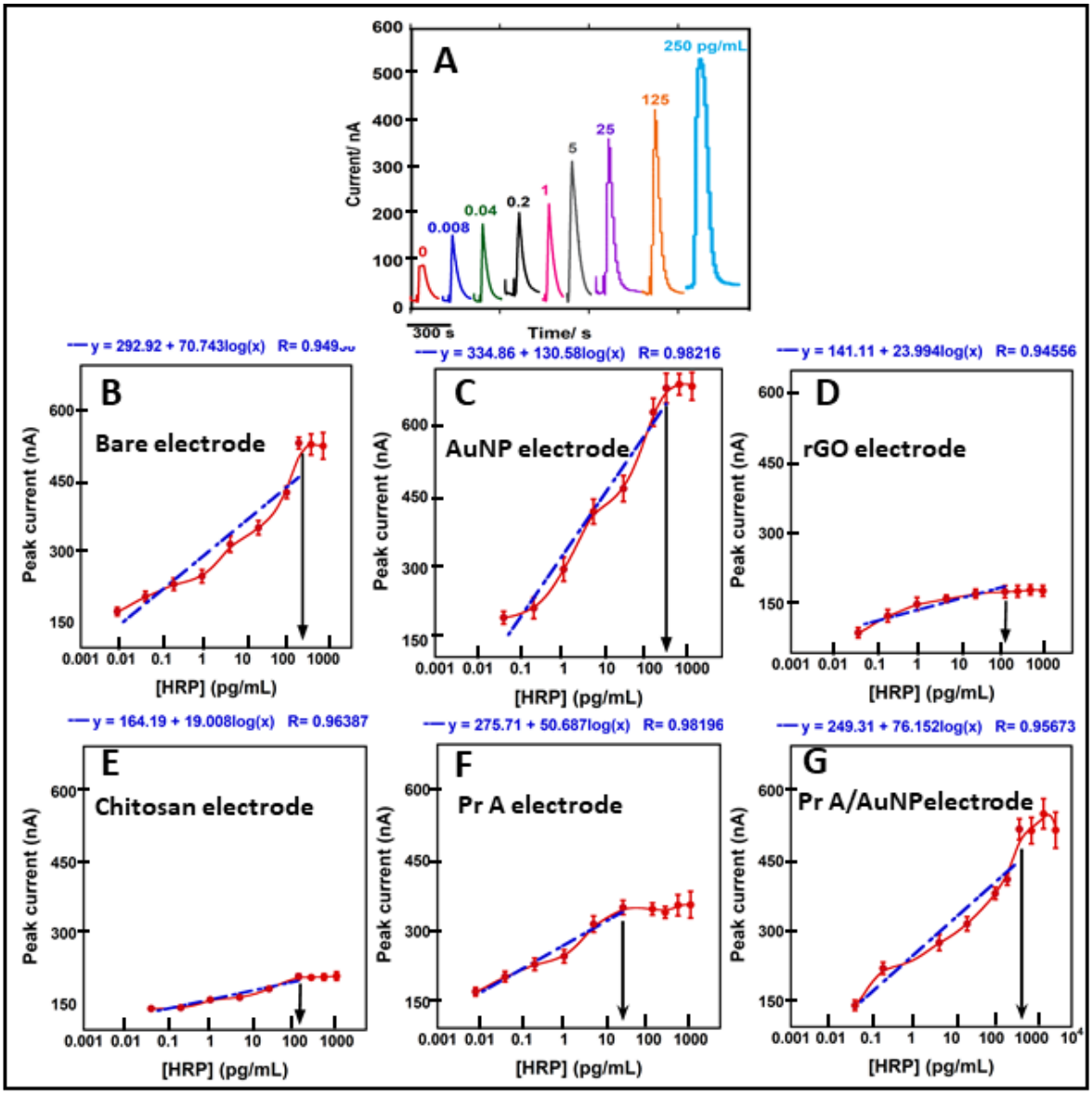

Fig. 5.4 Calibration for different anti-HRP immobilization strategies; (A) Example showing amperometric peaks with increasing concentrations of HRP using antibodies (Ab) passively adsorbed on bare carbon. Calibration graphs: (B) passively adsorbed Ab on bare electrodes; (C) covalently immobilized Ab on AuNP electrodes; (D) covalently immobilized Ab on rGO electrodes; (E) covalently immobilized on chitosan electrodes; (F) Ab oriented onto protein A passively adsorbed on bare electrodes; (G) Ab oriented onto protein A covalently immobilized on AuNP electrode. Logarithmic fits shown as blue dashed line; arrows indicate saturation points (Error bars = standard deviation, n=8)

Table 5.3. Theoretical calculation of no. of HRP available to bind to anti-HRP immobilized on electrodes at each concentration of HRP standards under diffusion control

[HRP] (pg mL^{-1})	**[HRP] available to bind anti-HRP/electrode (pg mL^{-1})**	**No. of HRP available to bind anti-HRP/electrode**
0.008	5.79×10^{-15}	8.20×10^{4}
0.04	2.90×10^{-14}	4.10E x 10^{5}
0.2	1.45×10^{-13}	2.05×10^{6}
1	7.24×10^{-13}	1.03×10^{7}
5	3.62×10^{-12}	5.13×10^{7}
25	1.81 x10^{-11}	2.56×10^{8}
125	9.05×10^{-11}	1.28×10^{9}
250	1.81×10^{-10}	2.56×10^{9}
500	3.62×10^{-10}	5.13×10^{9}
1000	7.24×10^{-10}	1.03×10^{10}

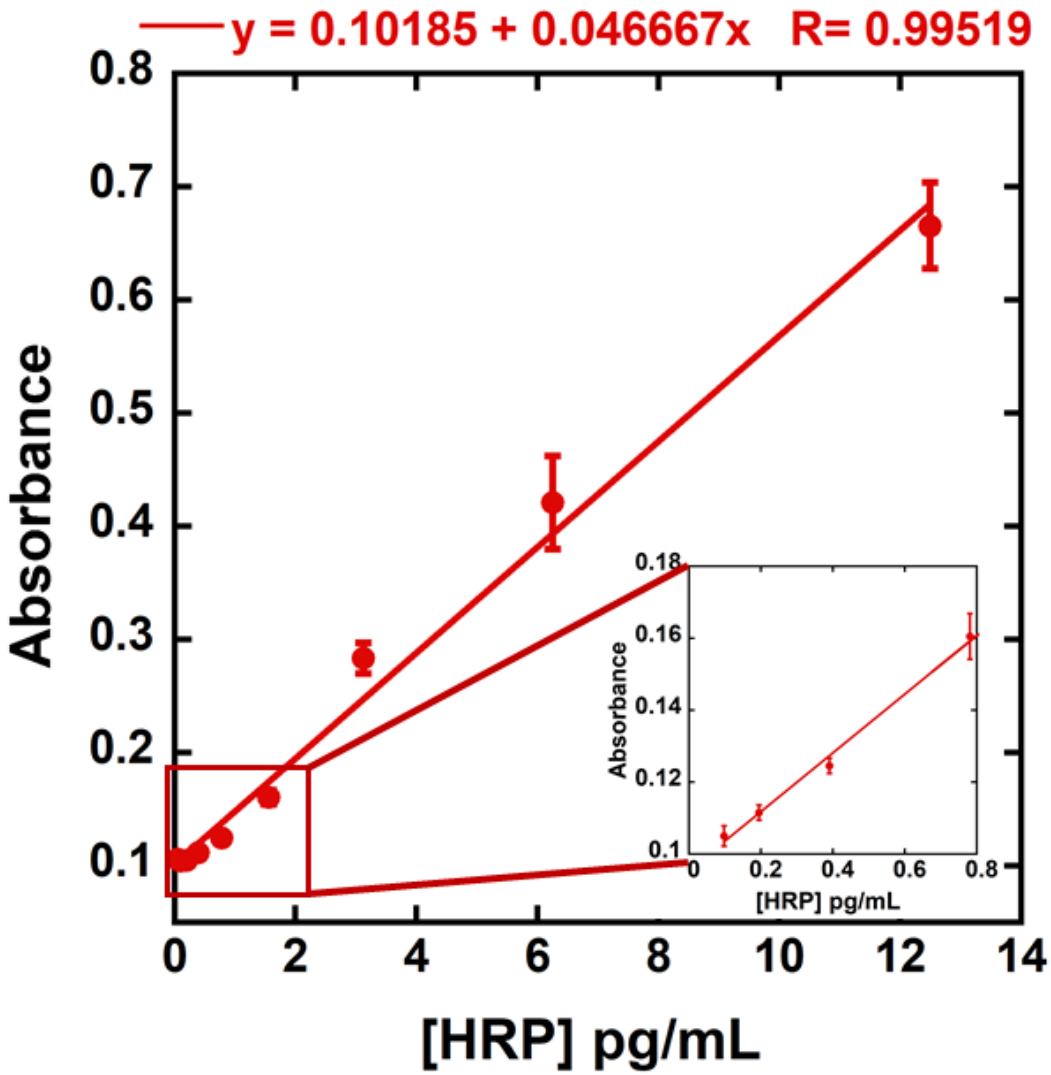

Fig. 5.5 Calibration curve of series of standard HRP using SIGMAFAST OPD assay. 100 µL O-phenylenediamine (4 mg/mL) in 0.05 M phosphate-citrate buffer (pH 5.0) was incubated with 100 µL of HRP standard for 1 hour, reaction was stopped using 25 µL 3M HCL and absorbance was measured at 492 nm. Error bars represent standard deviation, n=3.

Electrode to electrode variation. Selected concentrations of HRP were assayed on different electrode arrays on the same day to estimate intra-day signal variations for each immobilization strategy. Passive adsorption of antibodies on electrode surface and oriented antibody

immobilization using passively adsorbed protein A gave relative standard deviation (RSD) less than ±5%. For covalent attachment, RSDs were ±11%, for rGo electrodes, ±8% for AuNP, and 7% for chitosan and oriented antibodies on protein A covalently immobilized on AuNP (Fig. 5.6).

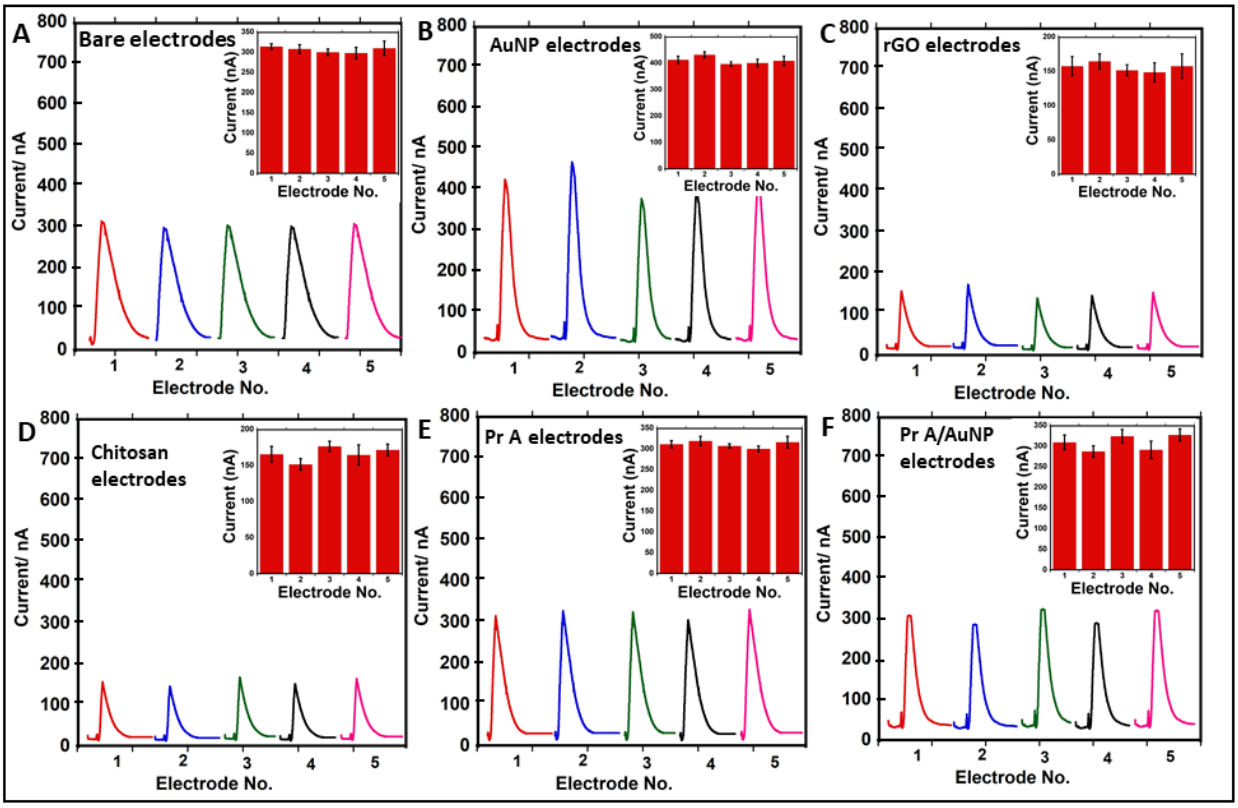

Fig. 5.6 Inter-day electrode to electrode variation showing amperometric peaks obtained from 5 different electrodes challenged against 5 pg mL^{-1} HRP; anti-HRP antibodies (A) passively adsorbed on bare electrodes; (B) covalently bound to AuNP decorated electrodes; (C) covalently bound to rGO coated electrodes; (D) covalently bound to chitosan modified electrodes; (E) oriented on protein A passively adsorbed on bare electrodes; (F) Anti-HRP oriented on protein A covalently immobilized on AuNP decorated electrodes. Insets are columns representing peak currents from different electrodes

Stability. Arrays were challenged with the same concentration of HRP over 5 days. Chitosan coated electrodes showed the best stability with only a small loss in signal over 5 days (≤ 7%). Electrodes with passively adsorbed antibodies were the fastest to deteriorate with 15-20% loss of activity each day in the first 3 days. AuNP and rGO electrodes were relatively stable for the first three days of storage (~5% decrease/day) followed by larger decrease in signal in 5th day of storage (~10%). Antibodies adsorbed on protein A electrodes had good stability over the test period with approximately 20% decrease in the overall signal after 5 days (Fig. 5.7, Table 5.4).

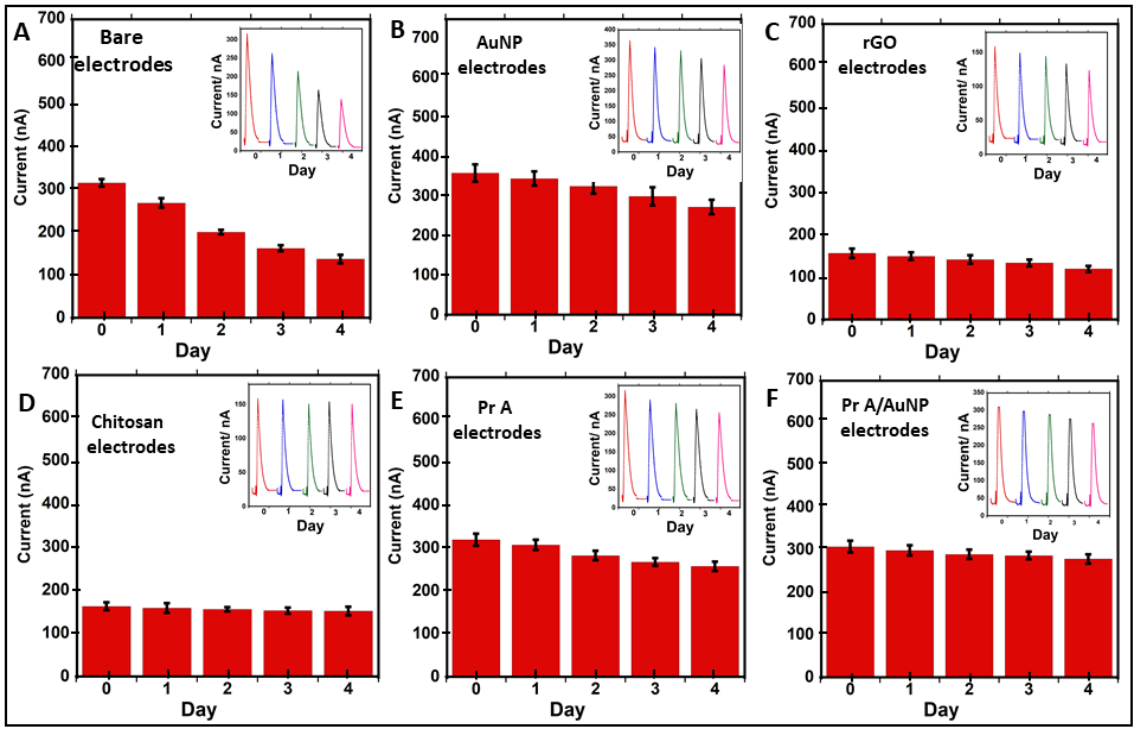

Fig. 5.7 Stability of electrodes as a function of change of the electrochemical amperometric signal challenged against 5 pg mL^{-1} HRP over a period of 5 days; Anti-HRP antibodies were (A) Passively adsorbed on bare electrodes; (B) Covalently immobilized on AuNP decorated electrodes; (C) Covalently immobilized on rGO coated electrodes; (D) Covalently immobilized on chitosan modified electrodes; (E) Oriented onto protein A passively adsorbed on bare electrodes; (F) Oriented onto protein A covalently immobilized on AuNP decorated electrodes. Insets are amperometric peaks. (Error bars represent standard deviation, n=8).

Table 5.4. Comparison of performance for HRP sensors using different antibody immobilization strategies on screen printed carbon arrays

Immobilization strategy	**LOD (fg mL^{-1})**	**Dynamic Range**	**Sensitivity (nA/log (pg mL^{-1})**	**No. of Ab/ Electrode (x10^{9})**	**Percent active antibodies**	**Signal loss after 5 days storage**
Anti-HRP/AuNP	40	40 fg mL^{-1} 250 pg mL^{-1}	2.40	6.2 ± 0.3	21%	≤ 30%
Anti-HRP/rGO	40	40 fg mL^{-1} 125 pg mL^{-1}	0.55	4.3 ± 0.3	30%	≤ 35%
Anti-HRP/Chitosan	40	40 fg mL^{-1} 125 pg mL^{-1}	0.90	6.1 ± 0.6	21%	≤ 7%
Anti-HRP/Protein A /AuNP	40	40 fg mL^{-1} 500 pg mL^{-1}	2.01	6.1 ± 0.4	85%	≤ 20
Anti-HRP/bare electrode	4	8 fg mL^{-1} 250 pg mL^{-1}	1.75	$^{1.1}$ ±0.03	60%	> 60%
Anti-HRP/Protein A/bare electrode	8	8 fg mL^{-1} 25 pg mL^{-1}	1.62	0.26 ± 0.1	98%	≤ 25

5.5 Discussion

Results above demonstrate the influence of antibody immobilization strategy and coatings on screen-printed carbon electrode for immunoarrays. Sufficient binding activity and availability of antibodies immobilized on sensor electrodes is a key factor for sensor performance, we found that other factors such as stability, degree of antibody coverage, orientation, and assay to assay variations also have an influence. We found that highly oriented antibody systems (using protein

A) can extend the dynamic range, but have little influence on sensitivity or LOD, most easily seen by comparing AuNP-electrodes with Protein A/AuNP (Table 5.4). This goes against the common view that improving antibody orientation also improves sensitivity and LOD of immunoassays.[7,8] Sensors with 20-30% orientation (Table 5.4) still have enough active antibodies to achieve good sensitivity and LOD in the lower concentration range, and had AuNP electrodes with 21% active antibodies had the best sensitivity. This result agrees with our earlier study of sensors coated with upright single-wall carbon nanotube forests having large antibody coverage, but ~30% active antibodies.[50] These sensors had excellent sensitivity and LODs for prostate specific antigen and interlukin-6 proteins in serum. For sensors with 85-95% correct antibody orientation, the main effect is maintenance of sensitivity in the higher concentration range because more of the antibodies are being active, and that extends dynamic range upward. We believe these conclusions are dependent on sizes of both antibodies and antigens.

Antibody coverage was highest when antibodies were bound to protein A/AuNP films electrodes (Table 5.4), although these sensors did not have the best sensitivities. In addition, nanostructured dense 5 nm AuNP packing[32] and the chitosan hydrogel property both extend the surface area available for Ab binding, leading to the binding of more antibodies. Electrodes with passively adsorbed antibodies showed the highest LODs (Table 5.4), but were the least stable (Table 3), Instability can be attributed to documented hydrophobic interactions between antibodies and electrode which lead to denaturation and loss of binding activity.[51] The hydrogel nature of chitosan causes antibody-chitosan matrix swelling in aqueous solution to more than 600% of its original mass.[47] The hydrogel provides high water content that also helps preserve antibody activity during storage by stabilizing conformation.[52,53]

rGO coated electrodes may have mixed affinities toward antibodies through covalent binding to residual carboxylic groups after electrochemical deposition and hydrophobic adsorption to graphene. This explains the intermediate antibody activity (30%), that lies between covalent immobilization and passive adsorption, of rGO coated sensors. Sensitivities and LODs of sensors with covalently immobilized antibodies were similar with LOD 40 fg mL^{-1} for chitosan modified, rGO coated and AuNP electrodes (Table 3). Wider dynamic range achieved by AuNP sensors compared to other covalent immobilization techniques can be attributed to high surface coverage of antibodies compared to other sensors. Although chitosan modified electrodes had surface antibody coverage similar to AuNP films, its narrower dynamic range is due to a degree of electron transfer blockage by the chitosan (Table 5.2).

Protein A passively adsorbed on the sensors preserved 98% of immobilized antibody activity, and maintained up to 80% of sensor activity after 5 days storage, but had the worst dynamic range (Table 5.4). This is presumably due to low surface coverage of antibodies, about 10% of that of the other sensors. This was overcome by covalent immobilization of protein A onto AuNP electrodes, which offers flexible anchoring and allowed a large increase in antibody coverage while maintaining 85% activity.

5.6 Conclusions

Results show that ability of the immunosensors to achieve high sensitivity is mainly a function of having sufficient active antibodies immobilized and the degree of surface coverage. Protein A mediated antibody surface conjugation that allowed oriented immobilization of antibodies preserved 98% of antibody activity, but was outperformed by other sensors possessed higher surface coverage (Table 5.4). In general, a high degree of antibody orientation on AuNP sensor did not improve sensitivity or LOD, but extended dynamic range to higher concentrations. Our

findings suggest that increasing the number of antibodies on sensors by increasing electrode surface area is key factor to improve sensitivity. In addition, stable covalent conjugation of antibodies protects them from hydrophobic interaction-induced denaturation found in passive adsorption.

5.7 References

([1]) Wei, Y.; Zeng, Q.; Huang, J.; Hu, Q.; Guo, X.; Wang, L. An Electro-Responsive Imprinted Biosensor with Switchable Affinity toward Proteins. *Chem. Commun.* **2018**, *54*, 9163–9166.

([2]) Lequin, R. M. Enzyme Immunoassay (EIA)/Enzyme-Linked Immunosorbent Assay (ELISA). *Clin. Chem.* **2005**, *51*, 2415–2418.

([3]) Peluso, P.; Wilson, D. S.; Do, D.; Tran, H.; Venkatasubbaiah, M.; Quincy, D.; Heidecker, B.; Poindexter, K.; Tolani, N.; Phelan, M.; et al. Optimizing Antibody Immobilization Strategies for the Construction of Protein Microarrays. *Anal. Biochem.* **2003**, *312*, 113–124.

([4]) K. M. Koczula and A. Gallotta, *Essays Biochem.* 2016, **60**, 111–120.

([5]) Brock, P.; Eldred, E. W.; Woiszwillo, J. E.; Doran, M.; Schoemaker, H. J. Direct Solid-Phase 125I Radioimmunoassay of Serum Cortisol. *Clin. Chem.* **1978**, *24*, 1595–1598.

([6]) Nanomaterials-based Electrochemical Immunosensors for Proteins. *Chem. Rec.* **2012**, *12*, 164–176.

([7])Shen M, Rusling J, Dixit CK. Site-selective orientated immobilization of antibodies and conjugates for immunodiagnostics development. *Methods*, **2017**, 116, 95–111.

([8]) Sharma S.; Byrne H.; O'Kennedy RJ. Antibodies and antibody-derived analytical biosensors. *Essays Biochem.* **2016**;*60*, 9–18..

([9]) Yáñez-Sedeño, P.; Campuzano, S.; Pingarrón, J. M. Pushing the Limits of Electrochemistry toward Challenging Applications in Clinical Diagnosis, Prognosis, and Therapeutic Action. *Chem. Commun.* **2019**, *55*, 2563–2592.

([10]) Rusling, J. F. Multiplexed Electrochemical Protein Detection and Translation to Personalized Cancer Diagnostics. *Anal. Chem.* **2013**, *85*, 5304–5310.

([11]) C. Jokerst, J.; M. Emory, J.; S. Henry, C. Advances in Microfluidics for Environmental Analysis. *Analyst* **2012**, *137*, 24–34.

([12]) Chikkaveeraiah, B. V.; Mani, V.; Patel, V.; Gutkind, J. S.; Rusling, J. F. Microfluidic Electrochemical Immunoarray for Ultrasensitive Detection of Two Cancer Biomarker Proteins in Serum. *Biosens. Bioelectron.* **2011**, *26*, 4477–4483.

([13]) Carvajal, S.; Fera, S. N.; Jones, A. L.; Baldo, T. A.; Mosa, I. M.; Rusling, J. F.; Krause, C. E. Disposable Inkjet-Printed Electrochemical Platform for Detection of Clinically Relevant HER-2 Breast Cancer Biomarker. *Biosens. Bioelectron.* **2018**, *104*, 158–162..

([14]) Lee, G.; Lee, J.; Kim, J.; Choi, H. S.; Kim, J.; Lee, S.; Lee, H. Single Microfluidic Electrochemical Sensor System for Simultaneous Multi-Pulmonary Hypertension Biomarker Analyses. *Sci. Rep.* **2017**, *7*, 7545.

([15]) Bertolino, F. A.; De Vito, I. E.; Messina, G. A.; Fernández, H.; Raba, J. Microfluidic-Enzymatic Biosensor with Immobilized Tyrosinase for Electrochemical Detection of Pipemidic Acid in Pharmaceutical Samples. *J. Electroanal. Chem.* **2011**, *651*, 204–210.

([16]) Uosaki, K.; Sato, Y.; Kita, H. Electrochemical Characteristics of a Gold Electrode Modified with a Self-Assembled Monolayer of Ferrocenylalkanethiols. *Langmuir* **1991**, *7*, 1510–1514.

([17]) Määttänen, A.; Ihalainen, P.; Pulkkinen, P.; Wang, S.; Tenhu, H.; Peltonen, J. Inkjet-Printed Gold Electrodes on Paper: Characterization and Functionalization. *ACS Appl. Mater. Interfaces* **2012**, *4*, 955–964.

([18]) Malhotra, B. D.; Chaubey, A.; Singh, S. P. Prospects of Conducting Polymers in Biosensors. *Anal. Chim. Acta* **2006**, *578*, 59–74.

([19]) Tiwari, J. N.; Vij, V.; Kemp, K. C.; Kim, K. S. Engineered Carbon-Nanomaterial-Based Electrochemical Sensors for Biomolecules. *ACS Nano* **2016**, *10*, 46–80.

([20]) Céspedes, F.; Martinez-Fàbregas, E.; Alegret, S. New Materials for Electrochemical Sensing I. Rigid Conducting Composites. *TrAC Trends Anal. Chem.* **1996**, *15*, 296–304.

([21]) Weber, S. G. Signal-to-Noise Ratio in Microelectrode-Array-Based Electrochemical Detectors. *Anal. Chem.* **1989**, *61*, 295–302.

([22]) Céspedes, F.; Alegret, S. New Materials for Electrochemical Sensing: Glucose Biosensors Based on Rigid Carbon-Polymer Biocomposites. *Food Technol. Biotechnol.* **1996**, *34*, 143–146.

([23]) Arduini, F.; Micheli, L.; Moscone, D.; Palleschi, G.; Piermarini, S.; Ricci, F.; Volpe, G. Electrochemical Biosensors Based on Nanomodified Screen-Printed Electrodes: Recent Applications in Clinical Analysis. *TrAC Trends Anal. Chem.* **2016**, *79*, 114–126.

([24]) Cinti, S.; Arduini, F.; Moscone, D.; Palleschi, G.; Killard, A. J. Development of a Hydrogen Peroxide Sensor Based on Screen-Printed Electrodes Modified with Inkjet-Printed Prussian Blue Nanoparticles. *Sensors* **2014**, *14*, 14222–14234.

([25]) Arduini, F.; Amine, A.; Majorani, C.; Di Giorgio, F.; De Felicis, D.; Cataldo, F.; Moscone, D.; Palleschi, G. High Performance Electrochemical Sensor Based on Modified Screen-Printed Electrodes with Cost-Effective Dispersion of Nanostructured Carbon Black. *Electrochem. Commun.* **2010**, *12*, 346–350.

([26]) Nunez-Bajo, E.; Blanco-López, M. C.; Costa-García, A.; Fernández-Abedul, M. T. Electrogeneration of Gold Nanoparticles on Porous-Carbon Paper-Based Electrodes and Application to Inorganic Arsenic Analysis in White Wines by Chronoamperometric Stripping. *Anal. Chem.* **2017**, *89*, 6415–6423.

([27]) Hatakeyama, Y.; Onishi, K.; Nishikawa, K. Effects of Sputtering Conditions on Formation of Gold Nanoparticles in Sputter Deposition Technique. *RSC Adv.* **2011**, *1*, 1815–1821.

([28]) Yu, X.; Munge, B.; Patel, V.; Jensen, G.; Bhirde, A.; Gong, J. D.; Kim, S. N.; Gillespie, J.; Gutkind, J. S.; Papadimitrakopoulos, F.; et al. Carbon Nanotube Amplification Strategies for Highly Sensitive Immunodetection of Cancer Biomarkers. *J. Am. Chem. Soc.* **2006**, *128*, 11199–11205.

([29]) Krause, C. E.; Otieno, B. A.; Bishop, G. W.; Phadke, G.; Choquette, L.; Lalla, R. V.; Peterson, D. E.; Rusling, J. F. Ultrasensitive Microfluidic Array for Serum Pro-Inflammatory Cytokines and C-Reactive Protein to Assess Oral Mucositis Risk in Cancer Patients. *Anal. Bioanal. Chem.* **2015**, *407*, 7239–7243.

([30]) Lvov, Y. M.; Lu, Z.; Schenkman, J. B.; Zu, X.; Rusling, J. F. Direct Electrochemistry of Myoglobin and Cytochrome P450cam in Alternate Layer-by-Layer Films with DNA and Other Polyions. *J. Am. Chem. Soc.* **1998**, *120*, 4073–4080.

([31]) Lvov, Y.; Decher, G.; Moehwald, H. Assembly, Structural Characterization, and Thermal Behavior of Layer-by-Layer Deposited Ultrathin Films of Poly(vinyl Sulfate) and Poly(allylamine). *Langmuir* **1993**, *9*, 481–486.

([32]) Mani, V.; Chikkaveeraiah, B. V.; Patel, V.; Gutkind, J. S.; Rusling, J. F. Ultrasensitive Immunosensor for Cancer Biomarker Proteins Using Gold Nanoparticle Film Electrodes and Multienzyme-Particle Amplification. *ACS Nano* **2009**, *3*, 585–594.

([33]) Sharafeldin, M.; Bishop, G. W.; Bhakta, S.; El-Sawy, A.; Suib, S. L.; Rusling, J. F. Fe3O4 Nanoparticles on Graphene Oxide Sheets for Isolation and Ultrasensitive Amperometric Detection of Cancer Biomarker Proteins. *Biosens. Bioelectron.* **2017**, *91*, 359–366.

([34]) Parkash, O.; Yean, C. Y.; Shueb, R. H. Screen Printed Carbon Electrode Based Electrochemical Immunosensor for the Detection of Dengue NS1 Antigen. *Diagnostics* **2014**, *4*, 165–180.

([35]) R. M. Pemberton and J. P. Hart, Preparation of Screen-Printed Electrochemical Immunosensors for Estradiol, and Their Application in Biological Fluids. In *Biosensors and Biodetection: Methods and Protocols: Electrochemical and Mechanical Detectors, Lateral Flow and Ligands for Biosensors*; Rasooly, A., Herold, K. E., Eds.; Methods in Molecular BiologyTM; Humana Press: Totowa, NJ, 2009; pp 85–98.

([36]) Chikkaveeraiah, B. V.; Mani, V.; Patel, V.; Gutkind, J. S.; Rusling, J. F. Microfluidic Electrochemical Immunoarray for Ultrasensitive Detection of Two Cancer Biomarker Proteins in Serum. *Biosens. Bioelectron.* **2011**, *26*, 4477–4483.

([37]) Kim, M. I.; Kim, M. S.; Woo, M.-A.; Ye, Y.; Kang, K. S.; Lee, J.; Park, H. G. Highly Efficient Colorimetric Detection of Target Cancer Cells Utilizing Superior Catalytic Activity of Graphene Oxide–magnetic-Platinum Nanohybrids. *Nanoscale* **2014**, *6*, 1529–1536.

([38]) Smith, P. K.; Krohn, R. I.; Hermanson, G. T.; Mallia, A. K.; Gartner, F. H.; Provenzano, M. D.; Fujimoto, E. K.; Goeke, N. M.; Olson, B. J.; Klenk, D. C. Measurement of Protein Using Bicinchoninic Acid. *Anal. Biochem.* **1985**, *150*, 76–85.

([39]) Porstmann, B.; Porstmann, T.; Nugel, E. Comparison of Chromogens for the Determination of Horseradish Peroxidase as a Marker in Enzyme Immunoassay. *J. Clin. Chem. Clin. Biochem. Z. Klin. Chem. Klin. Biochem.* **1981**, *19*, 435–439.

([40]) Cannes C.; Kanoufi, F.; Bard, A. J. Cyclic voltammetry and scanning electrochemical microscopy of ferrocenemethanol at monolayer and bilayer-modified gold electrodes. *J. Electroanal. Chem.*, 2003, **547**, 83–91.

([41]) Allen J. Bard and Larry R. Faulkner, Electrochemical Methods: Fundamentals and Applications, New York: Wiley, 2001, 2nd ed.

([42]) Saha, B.; Evers, T. H.; Prins, M. W. J. How Antibody Surface Coverage on Nanoparticles Determines the Activity and Kinetics of Antigen Capturing for Biosensing. *Anal. Chem.* **2014**, *86*, 8158–8166.

([43]) Sarma, V. R.; Silverton, E. W.; Davies, D. R.; Terry, W. D. The Three-Dimensional Structure at 6 A Resolution of a Human Gamma Gl Immunoglobulin Molecule. *J. Biol. Chem.* **1971**, *246*, 3753–3759.

([44]) Deis, L. N.; Pemble, C. W.; Qi, Y.; Hagarman, A.; Richardson, D. C.; Richardson, J. S.; Oas, T. G. Multiscale Conformational Heterogeneity in Staphylococcal Protein A: Possible Determinant of Functional Plasticity. *Structure* **2014**, 22, 1467–1477.

([45]) Tripathi, K.; Driskell, J. D. Quantifying Bound and Active Antibodies Conjugated to Gold Nanoparticles: A Comprehensive and Robust Approach to Evaluate Immobilization Chemistry. *ACS Omega* **2018**, *3*, 8253–8259.

([46]) Yang, L.; Biswas, M. E.; Chen, P. Study of Binding between Protein A and Immunoglobulin G Using a Surface Tension Probe. *Biophys. J.* **2003**, *84*, 509–522.

([47]) Sharafeldin, M.; Kadimisetty, K.; Bhalerao, K. R.; Bist, I.; Jones, A.; Chen, T.; Lee N. H.; and Rusling, J. F. Accessible Telemedicine Diagnostics with ELISA in a 3D Printed Pipette Tip. *Anal. Chem.* 2019, **91**, 7394-7402

([48]) Wilson, M. S.; Nie, W. Electrochemical Multianalyte Immunoassays Using an Array-Based Sensor. *Anal. Chem.* **2006**, *78*, 2507–2513.

([49]) Schurr, J. M. The Role of Diffusion in Enzyme Kinetics. *Biophys. J.* **1970**, *10*, 717–727.

([50]) Malhotra R.; Papadimitrakopoulos F.; Rusling J. F. Sequential layer analysis of protein immunosensors based on single wall carbon nanotube forests. *Langmuir*, **2010,** 26, 15050–15056

([51]) Butler, J. E.; Ni, L.; Brown, W. R.; Joshi, K. S.; Chang, J.; Rosenberg, B.; Voss, E. W. The Immunochemistry of Sandwich elisas—VI. Greater than 90% of Monoclonal and 75% of Polyclonal Anti-Fluorescyl Capture Antibodies (CAbs) Are Denatured by Passive Adsorption. *Mol. Immunol.* **1993**, *30*, 1165–1175.

([52]) Higashi, T.; Ohshita, N.; Hirotsu, T.; Yamashita, Y.; Motoyama, K.; Koyama, S.; Iibuchi, R.; Uchida, T.; Mieda, S.; Handa, K.; et al. Stabilizing Effects for Antibody Formulations and Safety Profiles of Cyclodextrin Polypseudorotaxane Hydrogels. *J. Pharm. Sci.* **2017**, *106*, 1266–1274.

([53]) Szenczi, Á.; Kardos, J.; Medgyesi, G. A.; Závodszky, P. The Effect of Solvent Environment on the Conformation and Stability of Human Polyclonal IgG in Solution. *Biologicals* **2006**, *34*, 5–14.